INVESTIGATION OF PORE FILLING OF NANOPOROUS ALUMINUM OXIDE BY THERMORESPONSIVE PNIPAM POLYMER USING SAXS EXPERIMENT

Dissertation

zur Erlangung des akademischen Grades eines Doktors der Naturwissenschaften

vorgelegt von

M.Sc. Mona Erfani

eingereicht bei der Naturwissenschaftlich-Technischen Fakultät der Universität Siegen

Siegen

September 2021

Prüfungskommission:

Vorsitzender:
Prof. Dr. Ullrich Pietsch (1. Gutachter)

Beisitzer:
Prof. Dr. Patrick Huber (2. Gutachter)
Prof. Dr. Holger Schönherr
Prof. Dr. Otfried Gühne

Tag der Mündlichen Prüfung:

18. März 2022

ABSTRACT

In this thesis we aim to determine the filling status and thermoresponsive behavior of polymer in the confinement of nanopores of aluminum oxide. The anodic aluminum oxide (AAO) nanopores are obtained by the anodization of the aluminum under certain conditions. The right choice of anodization condition enables us to achieve well-ordered hexagonal arrangement of circular pores. The AAO nanopores are then filled by thermoresponsive poly(*N*-isopropyl acrylamide) polymers (PNIPAM) with different percentages of solution concentration. The X-ray reflectivity (XRR) from polymers which are wetting on silicon substrates with various solution concentrations is used to determine their wetting and scattering properties.

Samples with empty and filled pores are carefully calibrated and examined by small angle X-ray scattering (SAXS). The in-situ SAXS experiment at filled samples is performed at temperatures above and below the lower critical solution temperature (LCST) with the purpose to find differences of the effective pore diameter caused by different wetting behaviors at the pores inner surfaces. The 2D scattering pattern is converted to line profiles which contains the structural information of the sample. An analytical model of SAXS intensity taken from the sample system is adapted to describe the scattering properties of samples under investigation. The parameters of the model are obtained by fitting to the experimental data employing a Monte-Carlo algorithm. It is shown that the developed mathematical model describes the structural parameters of the AAO in reasonable agreement and are in good agreement with previous works.

Particular details of the scattering pattern for the different measurements are found qualitatively with the help of a toy model. This model is built up by an analytical solution of the 2D gratings problem containing circular pinholes. The differences in samples with varied polymer solution concentrations as well as the differences for the measurements at various temperatures are estimated with the use of this model. More accurate model that can provide detailed and quantitative analysis of samples differences is explained. In this approach, the accuracy of the sample identification is a question of higher resolution of the measured data which can be gained by a different experimental setup.

ZUSAMMENFASSUNG

In dieser Arbeit sollen der Füllungszustand und das thermoresponsive Verhalten von Polymeren beim Einschluss von Nanoporen aus Aluminumoxid bestimmt werden. Die Nanoporen aus anodisiertem Aluminumoxid (AAO) werden durch die Anodisierung von Aluminum unter bestimmten Bedingungen erhalten. Durch die richtige Wahl der Anodisierungsbedingungen können wir eine geordnete hexagonale Anordnung der kreisförmigen Poren erreichen. Die AAO-Nanoporen werden dann durch thermoresponsive Poly(*N*-Isopropylacrylamid)-Polymere (PNIPAM) mit unterschiedlichen Prozentsätzen der Lösungskonzentration gefüllt. Das Röntgenreflexionsvermögen (XRR) von Polymeren, die auf Siliziumsubstraten mit verschiedenen Lösungskonzentrationen benetzt werden, wird zur Bestimmung ihrer Benetzungs- und Streueigenschaften verwendet.

Proben mit leeren und gefüllten Poren werden sorgfältig kalibriert und mittels Kleinwinkel-Röntgenstreuung (SAXS) untersucht. Das in-situ SAXS-Experiment an gefüllten Proben wird bei Temperaturen oberhalb und unterhalb der unteren kritischen Lösungstemperatur (LCST) durchgeführt, um Unterschiedlichkeiten im effektiven Porendurchmesser zu ermitteln, die durch unterschiedliches Benetzungsverhalten an den Poreninnenflächen verursacht werden. Das 2D-Streumuster wird in Linienprofile umgewandelt, die die Strukturinformationen der Probe enthalten. Ein analytisches Modell der SAXS-Intensität aus dem Probensystem wird angepasst, um die Streueigenschaften der untersuchten Proben zu beschreiben. Die Parameter des Modells werden durch Anpassung an die experimentellen Daten mit Hilfe eines Monte-Carlo-Algorithmus ermittelt. Es wird gezeigt, dass das entwickelte mathematische Modell die strukturellen Parameter von AAO in voller Übereinstimmung beschreibt und in guter Übereinstimmung mit früheren Arbeiten steht.

Besondere Details des Streumusters für die verschiedenen Messungen werden qualitativ mit Hilfe eines Spielzeugmodells gefunden. Dieses Modell basiert auf einer analytischen Lösung des Problems der 2D-Gitter-Problems mit kreisförmigen Löchern. Die Unterschiedlichkeiten bei Proben mit unterschiedlichen Konzentrationen der Polymerlösung sowie die Unterschiedlichkeiten bei den Messungen bei verschiedenen Temperaturen werden mit Hilfe dieses Modells geschätzt. Ein genaueres Modell, das eine detaillierte und quantitative Analyse der Unterschiedlichkeiten zwischen den Proben ermöglicht, wird erläutert. Bei diesem Ansatz ist die Genauigkeit der Probenidentifizierung abhängig von höherer Auflösung der Messdaten, die durch einen anderen Versuchsaufbau erreicht werden kann.

CONTENTS

1 INTRODUCTION

In recent years the investigations on the nanoporous-structured materials have been vastly developed. A primitive example of such materials is anodic aluminum oxide (AAO) nanopores. This type of nanoporous material has reached remarkable attention due to its tunable pore diameter and potential functionalization. Nanoporous AAO is synthesized under mild anodization (MA) or hard anodization (HA). The initial porosities are 10% in MA and 3% in HA and they can be increased up to 40% using the chemical process of widening. The pore shapes are mostly circular and the distribution of the pore diameter is narrow at any given porosity. The arrangement of the pores is hexagonal and it is rather well-order comparing other nanoporous materials e.g. porous silicon (pSi).

Since 1953 the fabrication of anodic aluminum oxide nanopores have been studied vastly. The process has been improved to obtain better order of the pore arrangement on the surface, more uniform pore diameter, and more parallel pores [1, 2, 3, 4]. These first achievements were followed by the studies which unraveled the dependence of characteristic sizes of the nanoporous AAO on the applied voltage [5, 6, 7].

With its flexible key properties, nanoporous AAO is applicable in an extensive range of subjects. In particular, it is applied as a template in synthesis of nanotubes and nanorods [8], catalysis [9], interferometric sensing [10, 11, 12], photonic structures [13], bone implants [14], and drug delivery systems [15]. Filling of the nano-scale porous materials with various materials have been studied vastly. An example is the confinement of water in nanopores which have been investigated in detail [16]. However, the replication of the AAO with soft matters such as polymers is at high interest due to its applications for sensors [17, 18, 19] and solar cells [20]. In our work, we make use of the wetting process to fill the AAO nanopores by the thermoresponsive poly(*N*-isopropyl acrylamide) polymer (PNIPAM) with different concentrations of solution.

The focus of this study is on empty and polymer-filled AAOs. Our motivation is to investigate the filling status of polymer inside the nanopores and their thermoresponsive behavior in the confinement of the pores at temperatures above

and below the lower critical solution temperature (LCST). This type of information helps us to understand the functionalization of such material as nanopumps, as substrates to interrogate cell-material interactions, and as sensing platform for enzymes, e.g., detect bacterial infections [8]. The filling status and thermoresponsive behavior of polymer filled AAO have been previously studied by the use of interference reflectance spectroscopy (IRS) and ellipsometry measurements [8].

In this piece of work, we aim to investigate the same problem with the use of X-ray experiment. The choice of experimental setup is a question of the dimensions of the target samples. To investigate their structure and dimensional properties a probe is needed sensitive on their scales.

Different X-ray measurements techniques are used for various studies. A few popular techniques are given in the following. X-Ray Reflectivity (XRR) is capable to measure the surface parameters such as roughness and the thickness of the thin layer films on a flat smooth substrate. X-Ray Fluorescence (XRF) gives information on the type and the concentration of the existing elements in the material. X-Ray Diffraction (XRD) provides knowledge on the lattice parameters of a bulk crystal structure. Whereas, Grazing Incidence Small Angle X-ray Scattering (GISAXS) is used to find crystallographic parameters of powder or solution of molecules of an organic material. Wide Angle X-ray Scattering (WAXS) is used to determine the crystallographic characters and phase shifts of partially ordered materials such as polymers. Since GISAXS and WAXS collect data of large angles, the given information is related to the smaller distances such as molecular scale. In contrary, Ultra Small Angle X-ray Scattering (USAXS) which collects data on very small angles and the given data is related to particles or structures in the sample with size scale of several hundreds of nanometers.

Small Angle X-ray Scattering (SAXS) is measured between these two ranges. this method of measurement gives information on structure of materials which are scaled between a few to hundreds of nanometers. The given information by SAXS are on both the size and the shape of measured sample. Considering the size scale of our samples and the type of the information of our interest, we investigate the problem by the experimental setup of the small angle X-ray scattering (SAXS).

Detailed explanation of scattering theory can be found in literature [21, 22, 23, 24]. The calculation of basic principles of SAXS scattering can be found for example in [24]. The study of SAXS intensity in gratings is the starting point through our study. This kind of work can be found in [25] where the SAXS intensity through a grating was analytically calculated. And in [26] where the transmission efficiency of the gratings was measured for several gratings' orders and different photon energies.

In recent years this kind of study has received high attention and accordingly developed vastly. Therefore, the SAXS intensity in gratings has been developed due to increasing applications of nano-scale gratings such as AAO. The collected angular range and wide spectrum of X-ray wavelength made SAXS experiment a perfect tool to investigate nano-scale gratings with various pore sizes. This tool provides the valuable information on shape, size and electron intensity of gratings, pores and inside the pores.

In our study we aim to find the filling status and swelling behavior of polymer inside AAO pores. For this, the difference of measurements for empty and filled samples should be found. This difference turns out to be very small. It should be tracked by

statistical methods via fitting procedure. To find a small statistically meaningful difference, a detailed and accurate mathematical model is needed to be fitted.

Steps towards the simulation of similar problem was also taken by Ruland et. Al, who worked on mesostructured nanocomposite films. Their samples were considered as parallel nanoscale cylinders arranged on a hexagonal system which were examined under SAXS experiment in synchrotron facility. The intensity of the SAXS experiment were evaluated using an advanced method based on fitting the data to a model function obtained by an analytical solution which provided structural parameters [27, 28]. Later they analyzed the influence of separate structural parameters in their simulations and applied on fitting to the measured data [29].

A more detailed and realistic model was expanded by Engel et, Al [30, 31]. Their mathematical model considered not only the properties of measured sample, but also the instrumental effects that contribute in the scattering pattern. They applied the model on empty and polymer-filled anodic aluminum oxide samples, albeit on a different SAXS setup. Later the model was expanded by Khaneft to be used for carbon nanotubes (CNTs) [32].

Another analytical analysis of SAXS data on porous systems was done by Hadley et. Al. Their samples were conical pores on amorphous SiO2 thin films and polycarbonate foils. The morphology of the cones was found by fitting the 2-D simulation to the scattering image of the measurements [33].

With regards to the SEM studies of our samples [8, 34], we extended/modified the mathematical model to explain them and used statistical methods with the use of Monte-Carlo algorithm to fit that model to our measured data.

There are other methods to simulate the SAXS intensity. As an example, the ray-tracing method has been used to simulate the X-ray transmission of a polycapillary X-ray lens where the capillaries are arranged in layered hexagonal structure [35]. Another approach towards clarifying the structural effect of the sample system was taken by Roslyakov et. Al. They investigated the crystallographic approach to discuss the effect of the deviation of the standing pores from the parallelity [36].

In this thesis empty AAO and polymer filled nanoporous AAO are examined under the setup of SAXS experiment. In the following chapter, chapter 2, the detailed explanation of the AAO samples is presented which includes the knowledge on dimensions and characters of the anodic aluminum oxide templates and also on the anodization method that leads to achieve variety of well-ordered nanopores with different diameters. It also explains the thermoresponsive PNIPAM polymers and their properties. The named polymers are used to coat the AAO templates and are investigated under SAXS experiment. In chapter 3 the DELAT synchrotron facility is explained followed by the description of the SAXS experimental setup. Chapter 4 is dedicated to present the history and basic concepts of X-ray theory with a focus on phenomena occurring during a SAXS experiment. The optical twin of the SAXS is explained at the end of the chapter. In chapter 5 the mathematical model of the SAXS intensity is explained. The model is modified to better reproduce the used samples in our experiments. The model includes the details that contribute in the SAXS intensity. The results for different cases of the calculated model are simulated in MATLAB platform. The experimental results are demonstrated in chapter 6 where the altered

model is used to fit them. The results are first investigated by an analytical method. Then a statistical approach is applied by the favor of Monte-Carlo algorithm. Finally in chapter 7 remarkable notes of the thesis are collected.

2 SAMPLES

As explained in previous chapter, deposition of materials in nano structures is at high interest. Nanoporous Anodic Aluminum Oxide (AAO) have a high porosity as well as a perfect periodicity under controllable conditions. Accordingly, nanoporous AAO is known to be a suitable template for deposition of soft materials such as polymers.

The samples represented in this work are nanoporous anodic aluminum oxides empty as well as filled by polymers. The desired porous anodic aluminum oxide is fabricated under certain environmental/laboratorial conditions in a homemade setup at physical chemistry department, University of Siegen.

The nanoporous AAO are made by anodization process. This process has received great attention from researchers in the recent years. It is a relatively easy and affordable process for the fabrication of nanostructured material. The anodization process represents one of the widespread methods to synthesis ordered nanostructures which consist close packed cells in a hexagonal arrangement.

In the following sections first, the structure of nanoporous AAO is illustrated. Then the anodization conditions are explained followed by an introduction to the process. After that the polymers are presented and then the filling process is explained.

2.1 The Structure of Nanoporous AAO Templates

The nanoporous AAO samples can be describe as long parallel nanoscale cylindrical pores which are made of aluminum oxide and placed within an aluminum matrix. The pores are arranged on a hexagonal lattice due to close packing (Figure 2.1). Each pore is embedded in a hexagonal cell the walls of the cells are made of oxide and they run parallel along the length of the pores.

The nanoporous AAO samples are characterized by certain features. The first feature is the interpore distance D_i also called the cell size. It is the distance between the centers of two adjacent pores which in a crystallography point of view is the representative for the lattice parameter of the hexagonal arrangement. The pore diameter d_p is the average value of the diameters of the pores. This value can be changed in the range of

a few nanometers to hundreds of nanometers related to the conditions of anodization. The values of D_i and d_p are both proportional to the anodization voltage (V). The length of the parallel cylindrical pores $L_p$is another characteristic feature. The pore length can be controlled by the anodization time and can be changed from a few nanometers to several micrometers.

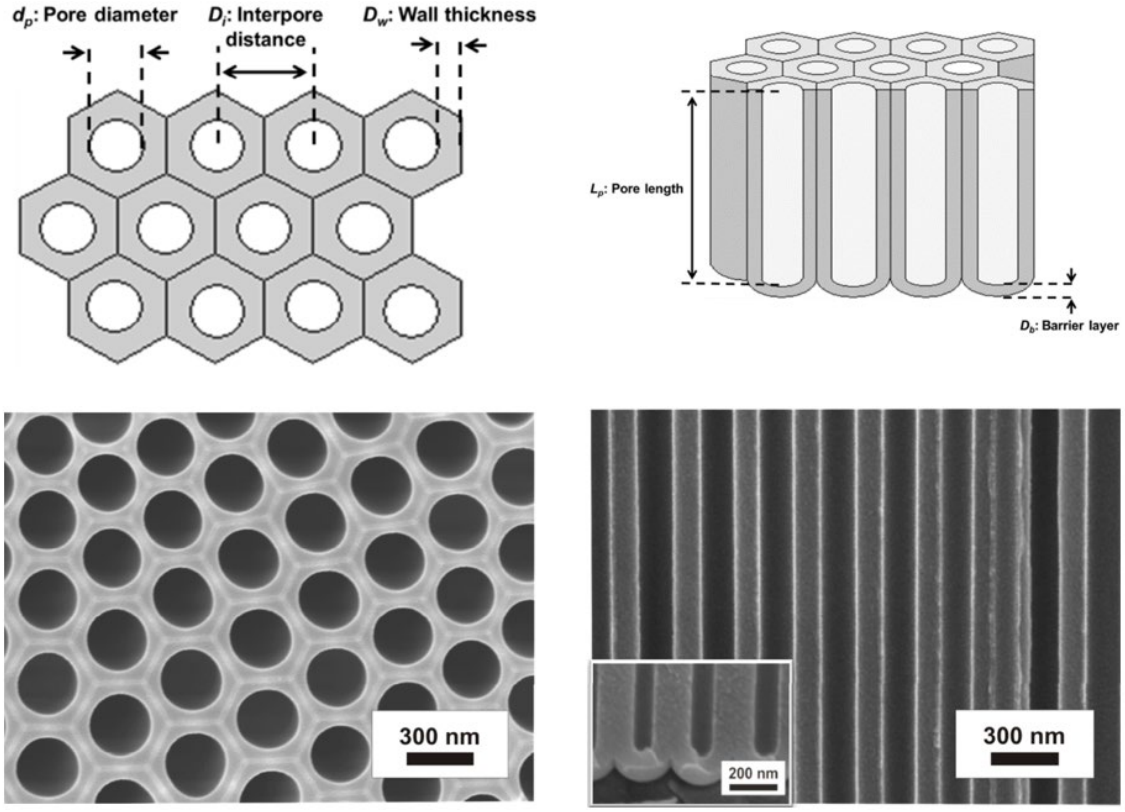

Figure 2.1 Schematic view (top) and FESEM image (bottom) of the nanoporous AAO. On the left is the top view and on the right is the side view of the membranes [34].

At the bottom of the pores there is a hemispherical oxide shell called the barrier layer BL. The thickness of the BL is denoted by D_b which depends on the anodization potential and the temperature of electrolyte solution [37]. The BL has an insulating nature since it is an oxide film formed along the aluminum matrix. The wall thickness D_w is related to the BL thickness as $D_w = 0.71D_b$ [38].

Another important feature is the porosity. It is defined as the ratio of the cell surface area that is occupied by the pores. Each cell contains one complete pore in the center. The surface area of the pore is $\pi\frac{{d_p}^2}{4}$. The length of each side of the hexagonal cell is $\frac{D_i}{\sqrt{3}}$ and the total surface area of the cell is $\frac{\sqrt{3}{D_i}^2}{2}$. Therefore, the porosity is calculated as follow [1]:

$$P = \frac{\pi}{2\sqrt{3}}\left(\frac{d_p}{D_i}\right)^2 \qquad 2.1$$

The domain is defined as the area over which the arrangement of the pores is well-ordered. Depending on the anodization voltage a nanoporous AAO contains many domains in the scale of a few to tens of μm^2. A favorable nanoporous AAO has larger domain area which is a cause of a better degree of ordering.

Several environmental and laboratorial conditions have significant effects on the cell dimensions and the growth of self-ordered pore. Temperature, electrolyte and anodization voltage are some of these effective conditions. The choice of the anodization voltage is an important starting point to obtain the desired pore diameter and interpore distance. The increment of anodization voltage results in the linear growth of the interpore distance D_i and the pore diameter d_p. The obtained interpore distance of AAO nanopores is linearly related to the applied potential with a proportionality constant of 2.5 ± 0.1 nmV^{-1} for MA [39, 40].

2.2 Anodization Conditions

Aluminum has a very high chemical affinity for oxygen. The aluminum oxide (Al2O3) is formed easily when a fresh aluminum surface is exposed to air. The oxidation process can be controlled by electrolysis technique. Nanoporous aluminum oxide is made by the well-known anodization procedure which may be defined as the coating of a metal with a protective oxide film by electrolysis technique.

For the synthesis of AAO nanopores two types of anodization procedures are established, namely “mild” and “hard” anodization. The samples presented here were synthesized under the mild anodization (MA) which is the most widely used method for the fabrication of the AAO nanopores in research.

The porous oxide films of aluminum are formed by the anodization of aluminum in acidic electrolytes, such as oxalic, phosphoric, sulfuric or chromic acid solutions. But the formation of self-ordered nanopores has been observed under the certain conditions.

To obtain highly ordered arrays of AAO nanopores with truly circular pore shapes certain conditions are needed to be fulfilled. These conditions restrict the MA anodization to three well-known regimes. These three MA anodization regimes are carried out at constant potentials of 25 V, 40 V and 195 V in sulfuric acid, oxalic acid and phosphoric acid respectively [41, 42, 43, 44]. These three regimes give rise to AAO membranes with interpore distances of 63 nm, 110 nm and 500 nm, respectively [45, 38, 46, 47]. In the presented work, samples are prepared under the first and second regimes which are the subjects of the following section.

2.3 Two-Step Anodization for Highly Ordered Nanoporous AAO

It is well known that impurities in the aluminum affect the anodization process. The surface characteristics and roughness of the Al may also affect the results of the AAO formation. Therefore, the anodization is performed on high purity aluminum foil (99.9999%) which is smoothened by electropolishing prior to anodization. When the electropolishing process starts the surface of the metal begins to be slowly eroded away. This process smoothens the Al surface at the micron level. As is shows in Figure 2.2 [34], the surface roughness is decreased after electropolishing. This process on the aluminum foils improves the regularity of the pore shapes and ordering of the pore structure during the anodization procedure [48].

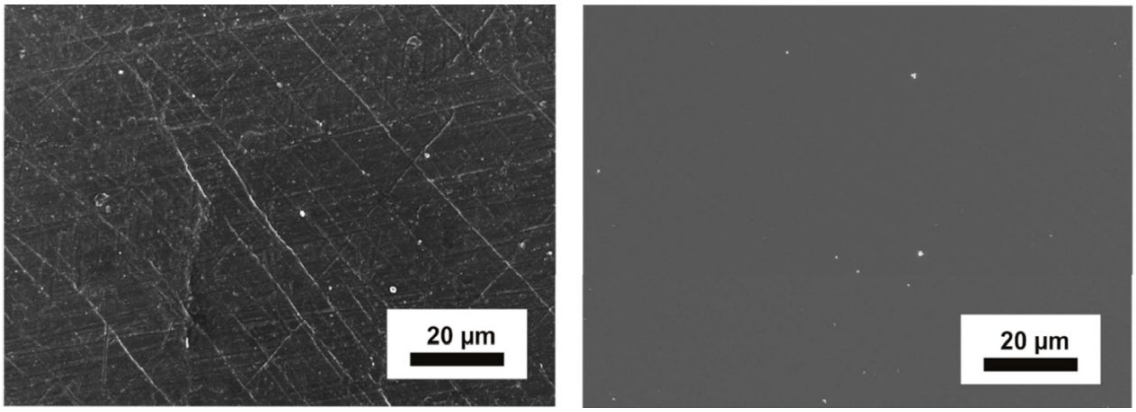

Figure 2.2 Highly pure aluminum surface before (left) and after (right) the electropolishing [34].

When the anodization is carried out for the first time, pores with irregular shapes and arrangement are formed. This problem is usually improved based on a two-step anodization. In this method two sequenced anodization processes take place in the same anodization condition. On the other hand, a long-term anodization helps the arrangement of nanopores to get more ordered. Therefore, the first anodization is performed on a longer period of time. This helps the formation of ordered pore configuration at the interface of the aluminum and oxide (Figure 2.3).

After the first anodization, the formed oxide layer is removed in a mixture of phosphoric and chromic acids. However, the pattern of the order of the formed pores on the first oxide layer is preserved on aluminum substrate. This pattern acts as a regular array of initiation sites for the pore formation in the second anodization step. Then the second is carried out with a significantly improved ordering of the nanopores and gives rise to the parallel highly ordered nanopores on the aluminum substrate. The two-step anodization process improves the resembling of the shape of the pores. In [34] it is shown that the histograms related to the pore diameters of AAO nanopores in different regimes has lower variance and the mean value is non-bias representative after the second anodization. It also has been observed that under optimal conditions this method increases the domain areas as well.

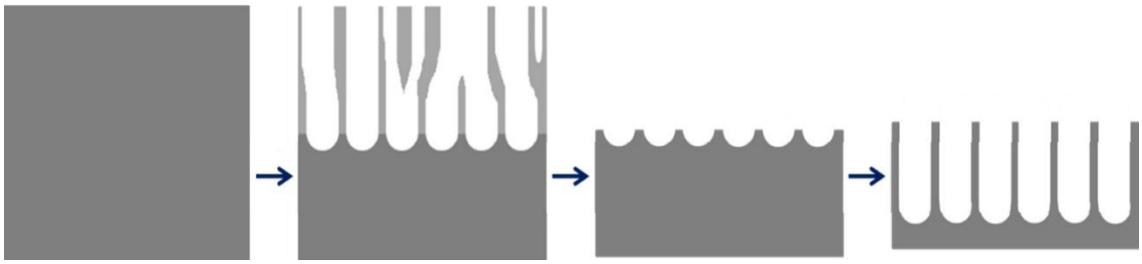

Figure 2.3 Schematic view of two-step anodization. The pores resulted from the first anodization are not parallel. The oxide layer is removed leaving the regular footprint. Second anodization gives rise to parallel pores on a well-ordered arrangement [34].

As it was mentioned in previous section, to reach the desired quality for samples, nanoporous AAO are fabricated under certain conditions that restrict the MA anodization to three well-known regimes. In the following we consider two regimes under which our samples were prepared.

In the first regime the MA anodization is conducted in sulfuric acid at 25 V [41, 42, 38]. In this case smaller pore diameter and interpore distance are obtained compared to the other two regimes. The first anodization time is between 10 to 12 hours. This is the critical time for the first anodization after which the ordering of nanopores is decreased. The second anodization is performed under the same condition. Timing of the second anodization depends on the desired pore length. Afterwards highly ordered nanopores are obtained with pore diameter and interpore distance of 19 ± 3 nm and 66 ± 4 nm respectively (arithmetic mean ± two times standard deviation) [34]. The well-ordered hexagonal structures with a mean cell size of 66 ± 4 nm are observed (Figure 2.4 a). There are evidences that the pores tend to grow during the anodizing as parallel channels.

The porosity for this regime was calculated according to equation 2.1 which is around 7 ± 0.4 percent. Figure 2.4.a represents distribution of pore diameter.

In the second regime [49, 40], oxalic acid is used at 40 V. The obtained interpore distance and pore diameter are 110 ± 2 and 55 ± 4 respectively. The resulted porosity is 22 ± 0.4% which is higher than for the other two regimes in MA. The pore diameter of AAO nanopores is sensitive to the temperature. This value changes between 41 ± 7 nm and 67 ± 6 nm by varying the temperature of the electrolyte between 5 °C and 15 °C, which results in a change of the porosity between 12 ± 0.2 and 32 ± 0.3%.

The obtained interpore distances of AAO nanopores in the MA method is linearly related to the voltage applied for anodization. Figure 2.4.c shows this linear relation with a proportionality constant of 2.5 ± 0.1 nmV^{-1} which agrees favorably with the previous reports [40].

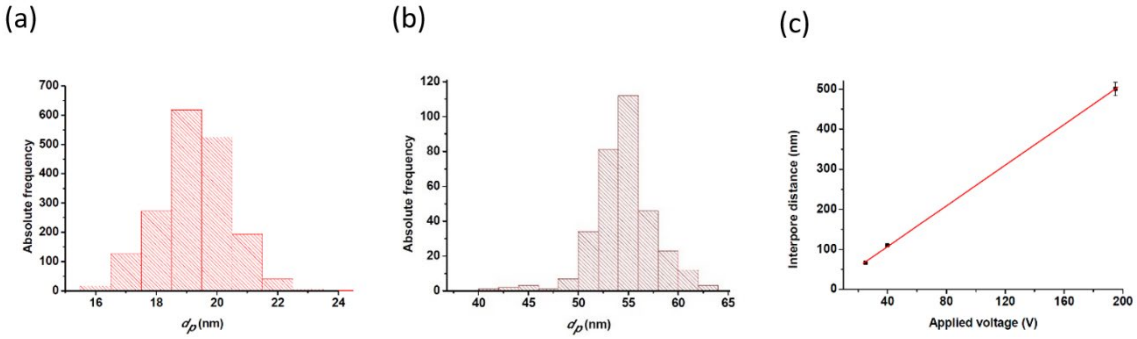

Figure 2.4 Distribution of pore diameter in AAO samples anodized at 25 V (left) an 45 V (middle). The value of interpore distance is linearly related to anodization voltage with factor 2.5 ± 0.1 nmV^{-1} (right) [34].

The pore diameter of the AAO nanopores obtained by MA can be expanded by the widening process. This is a useful approach when we aim to fabricate templates to deposit and grow materials within the pores. Phosphoric acid solution is commonly used for this chemical procedure. The wall thickness of the cell determines the maximum diameter that can be achieved by widening. This value is less than 35 nm for pores fabricated under first and second regimes of MA anodization.

2.4 Polymers

The word Polymer consist of two Greek words “poly” meaning many, and “meros” meaning parts or units. A polymer is repetition of large molecule or macromolecules units which are identical or similar to each other. The repeating units are called monomers [50]. The arrangement of the monomers defines the properties of polymer. Polymers containing identical monomers are known as homopolymers, whereas the polymers with repeating units made of more than one kind of monomers are known as copolymers [51].

The chemical process that combines monomers is called “Polymerization”. Monomer molecules are covalently bonded during polymerization and build up polymer chains or three-dimensional networks [52, 53].

There are different aspects in which polymers are classified. They are classified with regards to their sources, structure, polymerization method, molecular forces, thermal behavior, etc.

Poly(*N*-isopropylacrylamide) (PNIPAAm) is the kind of polymer that has been widely used in many fields such as biomedical and drug delivery. This polymer exhibits a prolific property as it is a temperature-responsive polymer. According to the changes in temperature, PNIPAAM polymer solution gets hydrated or dehydrated in a reversible manner [54]. The Lower Critical Solution Temperature (LCST) is the temperature below which the polymer solution gets hydrated and above it is immiscible. For PINIPAAM LCST is 32 °C [55].

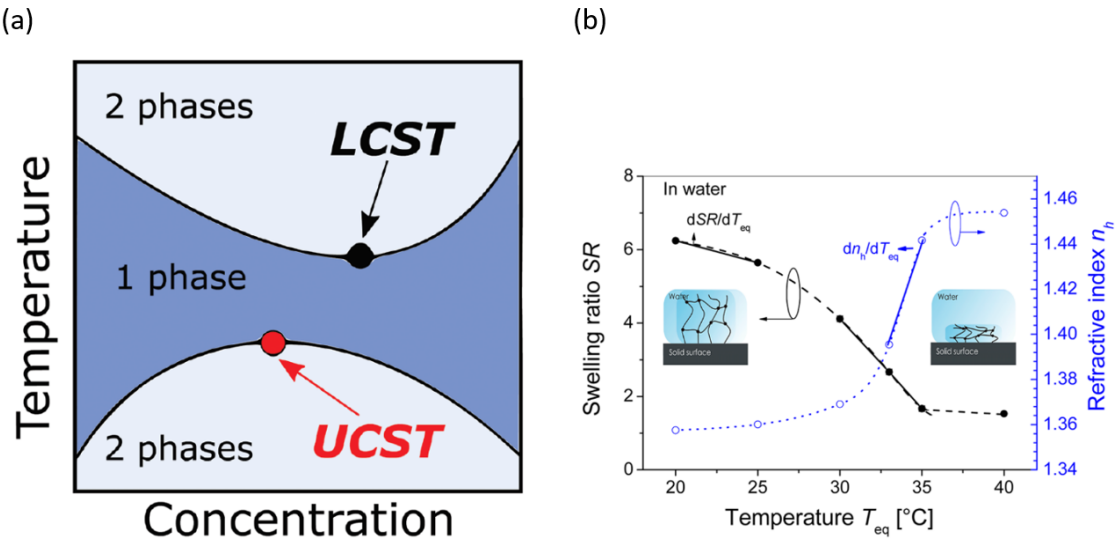

Figure 2.5 A typical phase behavior diagram which shows the two types of behavior of the material [56]. (b) changes in the refractive index with regards to the temperature and ratio of swelling [57].

PNIPAM is categorized as a hydrogel. The molecules of a hydrogel polymer bind to water primarily by noncovalent hydrogen bonds and make up the gel. In the hydrated phase, this kind of polymer swells in water with a considerable increase in volume, but without losing material cohesion [58]. For a PNIPAM-based polymer below LCST the chains of the polymer are miscible in water and therefore the PNIPAM hydrogel swells. Whilst, the chains are immiscible above the LCST which causes the hydrogel to collapse

at dehydrated phase. This two-phase behavior of the polymer is often shown by phase diagram (figure 2.5) [56].

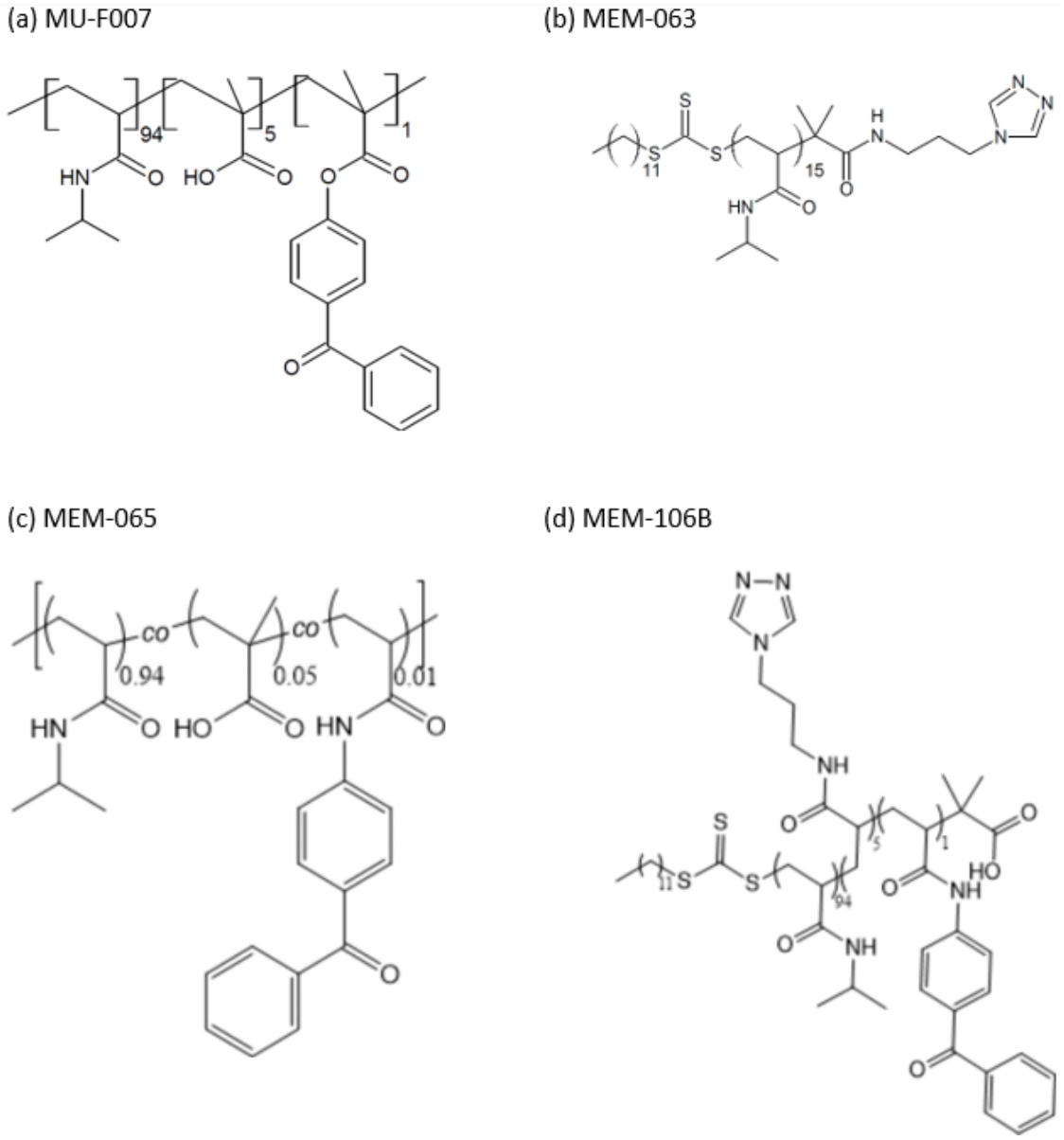

Figure 2.6 The chemical structure (chemsketch) of the four PNIPAM-based polymers used in this study. (a) MU-F007, (b) MEM-063, (c) MEM-065, and (d) MEM-106B. Chemsketch produced by Maximilian Meier, Macromolecular chemistry, University of Siegen.

The swelling of the polymer leads to the decrease in its density and therefore electron density. On the other hand, the collapse causes a higher electron density. Since the refractive index of any material is related to its electron density, in some studies the LCST is determined by observing the changes in refractive index of the hydrogel [57].

In our study, four kinds of PNIPAM-based polymers were used namely:

- MU-F007: poly(NIPAM94-*co*-MAA5-*co*-MABP1), synthesized by Franz Müller (Macromolecular Chemistry, University of Siegen), LCST = 35.9°C for the heating and 33.5°C for the cooling cycle [8].
- MEM-063: Poly(NIPAAm)-DMP-APTRZ with DMP-APTRZ (RAFT), synthesized by Maximilian F. T. Meier (Macromolecular Chemistry, University of Siegen), LCST = 34.7°C.
- MEM-065: **Poly(NIPAAm-co-MAA-co-BPAAm) (94:5:1) (FRP)**), synthesized by Maximilian F. T. Meier(Macromolecular Chemistry, University of Siegen), LCST = 33.6°C for the heating and 27.3°C for the cooling cycle.
- MEM-106B: **Poly(NIPAAm-co-APTRZAAm-co-BPAAm) (94:5:1) with DMP (200:1:0.05) (RAFT)**, synthesized by Maximilian F. T. Meier (Macromolecular Chemistry, University of Siegen), LCST around 40°C for the heating and 35°C for the cooling cycle.

2.5 Thermo-Responsive Polymer Coated Nanopores

One approach to the replication of AAO nanopores templates by polymer solutions or melts, is the wetting method. It is an easy and reliable approach for the fabrication of polymer nanotubes [59] or nanowires [60]. This approach is at high interest as it offers the advantage of the control on the thickness of polymer film as well as on its function by the right choice of soft materials formed on the AAO template walls. The wetting conditions such as the geometry of the template and the properties of the polymer solution defines the shape and the functionality of the structures.

Surface energy is playing an important role on formation of the polymer films on the AAO substrate. It can be defined as the work required to cut a bulk sample to creating its surfaces in a specified surrounding. Inorganic materials such as AAO commonly possess high energy surfaces [61]. While this value is low for polymer solutions the combination of a low surface energy liquids and a high surface energy of a solid substrates leads to the formation of liquid film on the solid substrate [62]. This process is applicable for forming polymer nanotubes inside the AAO template [63].

In wetting process, the polymer solution or polymer melt is placed on the top of the template. The polymer film is formed inside the nanopores within a short time [64, 65].

The driving forces leading to the formation of the polymer thin film are the van der Waals interactions. In case of the complete filling of the pores the dominant forces would be cohesive forces. Since the latter forces are much smaller than the former ones [8], formation of thin films inside the pores is more likely to occur. Therefore, the fabrication of polymer nanowires is more challenging than the polymer nanotubes [66].

The process of wetting can be described by the spreading coefficient S. This value is related to the surface tension of the polymer solution and the nanopores [62]. It is defined as follow:

$$S = \gamma_{sg} - \gamma_{sl} - \gamma_{lv} \qquad 2.2$$

γ_{sg}, γ_{sg}, and γ_{sg} are the the interfacial tensions between the solid and the gas, the solid and the liquid, and between the liquid and the gas respectively. The value of S gives information on the status of filling. If S is a positive value, the case is a complete filling and a nanorods are formed inside the pores [67]. On the other hand, if S is negative, the wetting is incomplete and the polymer is spread partially into the pores [68, 69, 70]. The value of S can be changed laboratory by the changes in the loading temperature. At temperatures higher than a critical wetting temperature the wetting spread shifts from partial filling to complete filling [69].

The LCST of pure PNIPAM in water was determined by Heskins et al. as 31°C [71]. However, the corresponding value for PNIPAM-based polymers is modified due to the concentration of the polymer in solution and on the molar mass of the polymer [72, 73]. When these functional polymers are confined in an AAO template, they modify the pore diameter into an alerting parameter with regards to the temperature. The thermo-switching of PNIPAM has been used in thermo-responsive gels, (bio)sensors, tissue engineering and drug delivery [74]. In [8] the coating of AAO with PNIPAAM-based polymers was performed.

In the presence of water the thermo-responsive PNIPAM swells at temperatures below the lower critical solution temperature (LCST) and collapses above the LCST. The AAO was loaded with PNIPAM-based polymers, to understand the polymer-functionalized nanopores behavior and the thermo-switchable response of the polymer in the confinement of the nanopores.

In [8] the successful replication of AAO nanopores by PNIPAAM-based polymers (MU_F007, MEM062c, MEM063, etc) have been observed. The functionality of polymers have been observed by changes of refractive index of in temperatures below and above the LCST via interference reflectance spectroscopy (IRS) measurements.

3 EXPERIMENT

The experiments of this study have been performed at DELTA [75]synchrotron radiation facility. The abbreviation DELTA stand for Dortmund ELecTron Accelerator. It is located at Technical University of Dortmund and is operated by the Centre of radiation. This facility contains an electron storage ring with a beam energy of 1.5 GeV and is a synchrotron light source for users. The injection current is 120 mA with a lifetime of 10 to 14 hours [76].

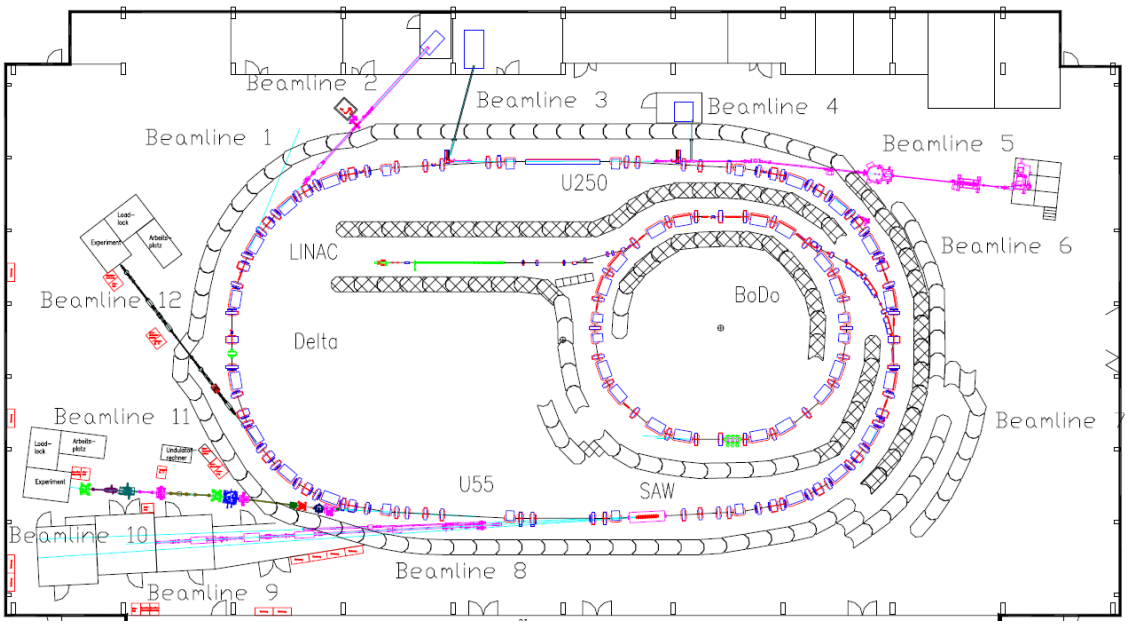

Figure 3.1 Schematic view of DELTA accelerator complex [77].

There are 12 beamlines in DELTA facility. Different detector types and experimental setups are accessible in many of them. However, some of them are designed for particular type of experiments. The experiments of the current work have been carried out at BL9 and BL10. The scheme and setup of the two beamlines are explained in the following sections.

A Superconducting Asymmetric Wiggler (SAW) with 20 poles with a magnetic gap of 18 mm provides the beam simultaneously for three beamlines [78, 79, 80, 81], beamline 8 with an energy range between 4 to 30 keV , beamline 9 with the energy range between 2 to 30 keV [78, 79, 80] and beamline 10 with an energy between 4 keV to 16 keV [76].

3.1 Beamline 9 (BL9) and Beamline 10 (BL10) at DELTA

Beamline 9 provides an intensive beam with energy between 4 to 30 keV selected by a silicon (311) double crystal monochromator. There is a two-slit system (S1 and S2) to collimate the beam followed by a guard slit (S3) to reduce the slit scattering. The absorber system can be set between 4 different values to attenuate the incoming photon beam. After that there is another slit (S4) to control the beam exposure. Two normalization detectors are located before and after the absorber to evaluate the direct beam. After setting the beam with desired parameters, it reaches the sample located on the diffractometer. The diffractometer has six-axis rotation as well as 3 translations. Then comes the detector which in our case is the two-dimensional PILATUS detector. The detector is built up of 195 by 487 square pixels with length 172 micro meters. It is located on the direction of incoming photon beam and records the 2D diffraction pattern as a tiff image file. The scheme of the BL9 setup is given in figure 3.2 [79, 78].

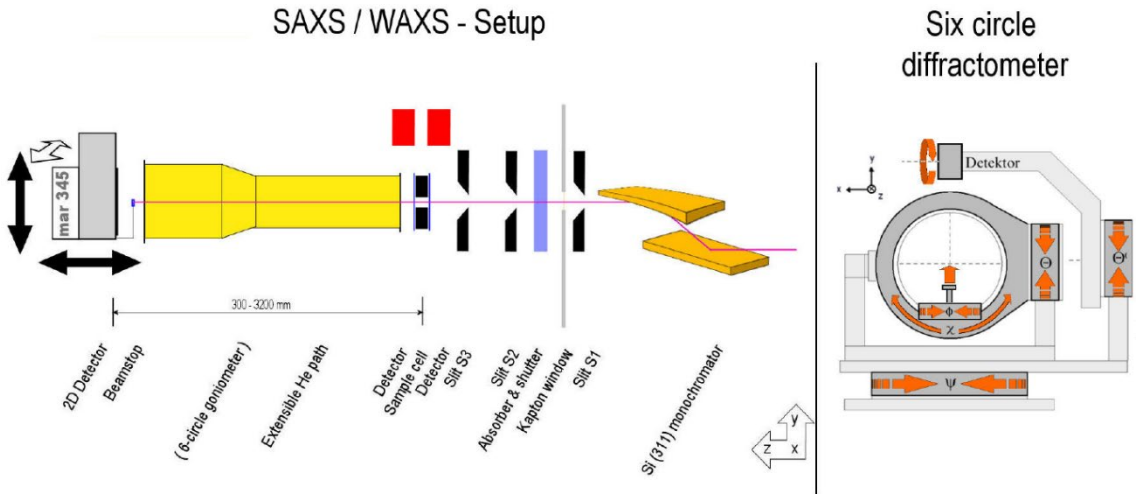

Figure 3.2 Schematic view of left: setup at BL10 and rigt: six-axis diffractometer [82].

The BL10 is equipped with a Si(111) channel-cut monochromator. The energy range 4 keV to 16 keV at BL10 corresponds to 3.1 to 0.7 A˚ of wavelength. The experimental setup for X-ray absorption spectroscopy, diffraction measurements and surface-sensitive X-ray reflectivity experiments are available at BL10. Different detection modes are accessible such as transmission, fluorescence and reflectivity. As in the case of BL9 the diffractometer at BL10 is a six-axis kappa diffractometer. Translation on the three Cartesian directions are also possible. Different kinds of detector are available including gas-filled ionization chambers, different photodiodes and Pilatus 2D-detectors.

The three beamlines originating from the SAW are installed in a limited space. This causes to a rather small space of the experimental hutch. The experimental hutch at BL10 is around 3.8 m long 1.4 - 1.5 m wide (Fig. 3.3). The centre of the monochromator is installed about 1.5 m apart for the lead shielding on the walls. An EXAFS table of about 80 cm length is installed between two slits. This table allows a flexible operation between the different set-ups of the different X-ray techniques. Then the six-axis user diffractometer is installed in the line directly downstream of the monochromator. The table is about 30.8 m and the diffractometer is about 31.7 m far from the source. An I0 detector and additional slit systems may be mounted on the EXAFS table as well as beam attenuators and also a He-gas-filled or evacuated flight tube [76].

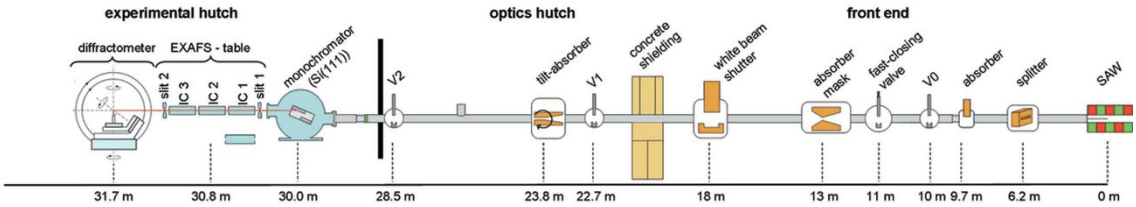

Figure 3.3 The scheme of the side view of the setup at BL10 [76].

3.2 Experimental Setup

The samples should be prepared for the SAXS experiment. The backside aluminum of the sample is a strong absorber of the photon beam for the SAXS experiment. Since it has no contact to the inside walls of the pores and therefore does not play any role on the filling status of the polymer inside them, it is removed from the sample to raise the photon number and therefore the resolution of the data.

To study the temperature sensitivity of the polymer in the confinement of the pores, a sealed sample holder is designed to keep the water inside (fig. 3.4). The heating process is performed by a capton heater and the temperature is controlled by an in-house designed device at electronical workshop of the ENC at university of Siegen.

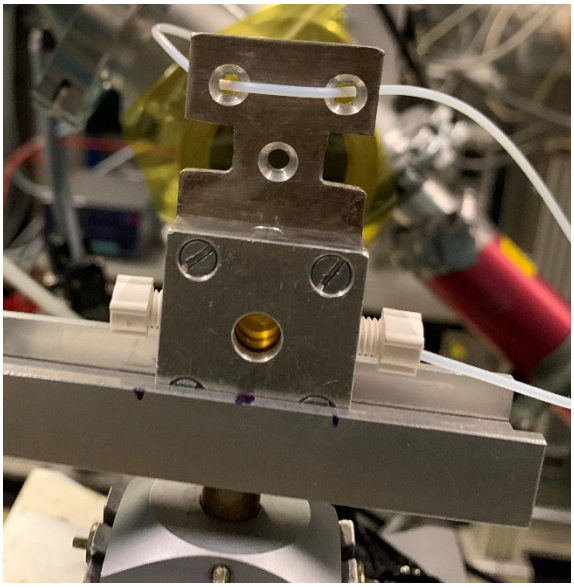

Figure 3.4 The designed sealing sample holder.

The energy is mostly set to 13 keV. A few experiments have been carried out at 10 keV. Beam size is changed between 0.2 mm by 1mm or 0.5 mm by 0.5 mm. 2D-Pilatus detector is used for the experiments. In order to have larger angular resolution, the sample to detector distance should be as large as possible. This distance is around 1 m at BL9 and 1.3 m at BL10.

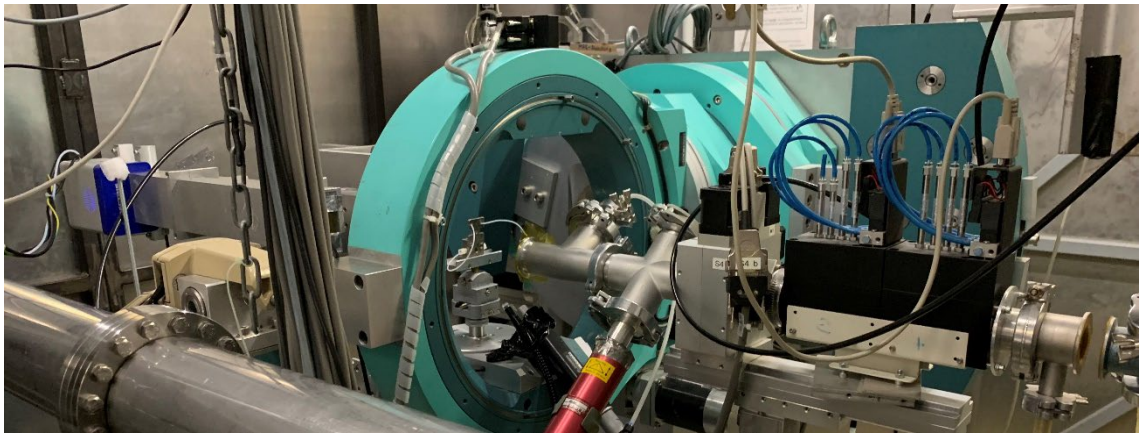

Figure 3.5 The SAXS experimental setup at BL9.

4 THEORETICAL BACKGROUND

The X-ray is a high energy radiation of the electromagnetic spectrum discovered by German scientist Wilhelm Röntgen in 1895 [24]. The energy range contains from 4 keV to 400 keV, corresponding to 9.67×10^{11} MHz and 9.67×10^{13} MHz in frequency, and 3.1×10^{-10} m and 3.1×10^{-12} m in wavelength. Today X-rays have diverse applications in a variety of fields, including fundamental research, security, and medical purposes.

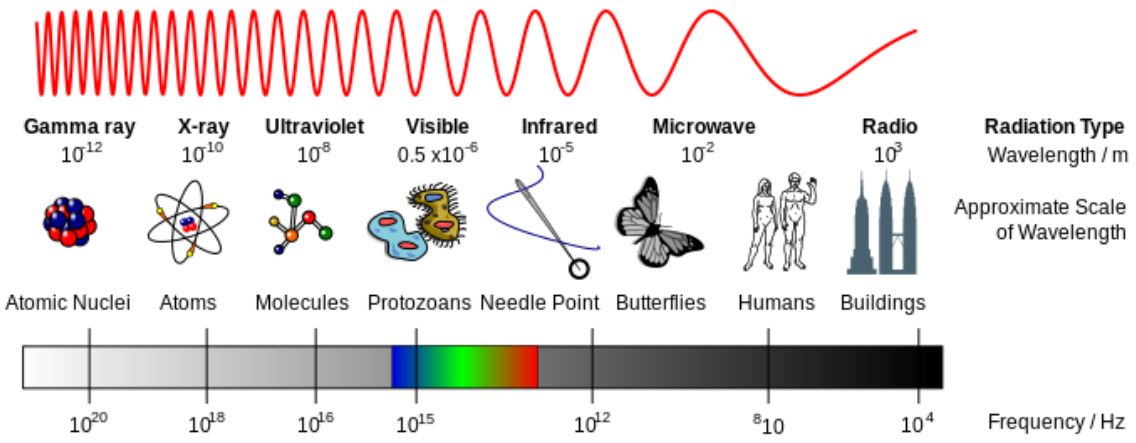

Figure 4.1 The spectrum of the electromagnetic wave. The main categories are shown [83].

Since its discovery, X-rays are widely used to study the structure of materials from the atomic up to the nanometer scale. X-rays are a strong tool for studying the building blocks of materials and understanding their physical properties.

In this chapter, we start with a brief summary of the of X-rays history, followed by a review of the X-ray sources. Then the elements of X-rays are presented with an emphasis on their interaction with matter. The method of Small-Angle X-ray Scattering (SAXS) is explained next, which is used in this work. Finally, the optical twin of the SAXS is explained as a transmission phenomenon.

4.1 Discovery, Early History, and Sources

In November 1895 X-rays were discovered by Wilhelm Conrad Röntgen in his laboratory at the University of Würzburg, Germany. He observed unexpected radiations on a detection screen, which he named X-rays due to their unknown nature. He discovered that this new radiation passes through wood and paper, with the metallic materials leaving shadow on the screen. He photographed the very first X-ray image, which was of his hand, and saw his own bones. Later, he realized that the shadows left by the metals and the bones are due to the X-ray absorption, which depends strongly on the atomic number of the probe to the power of 4. In 1901 he was awarded the Nobel Prize in Physics for his remarkable discovery.

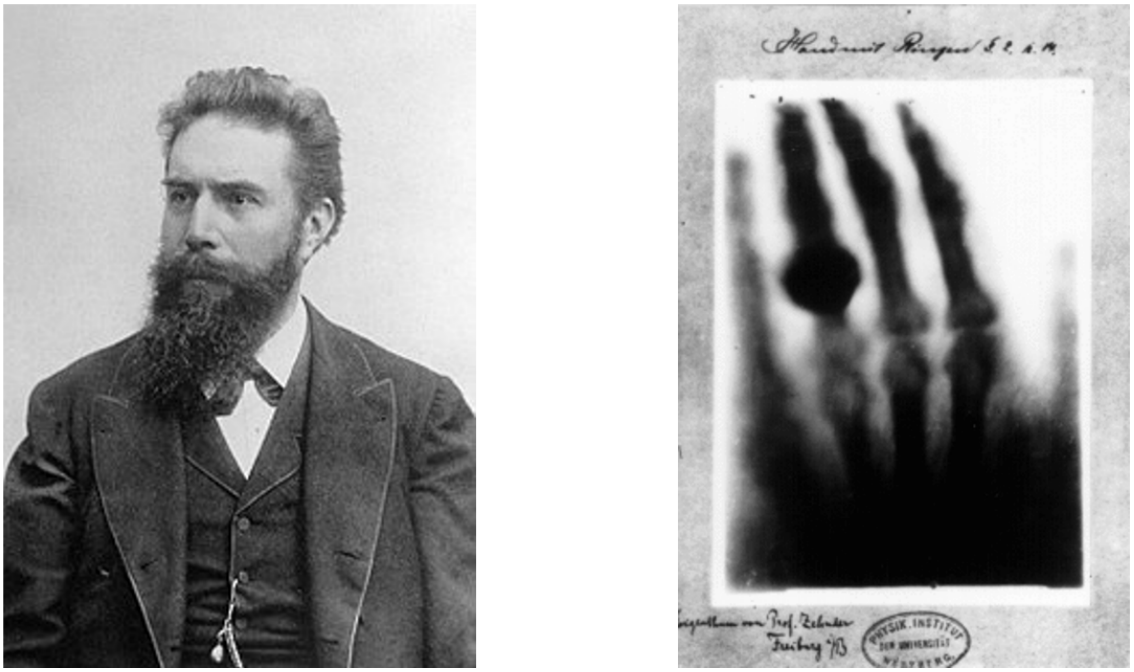

Figure 4.2 Left: Wilhelm Conrad Röntgen (1845-1923) [84]. Right: one of the first X-rays taken by Röntgen from his wife's hand in 1895 [85].

4.1.1 Birth of Crystallography

It was 17 years after the discovery of X-rays when Max von Laue found the first diffraction pattern of a crystal, where he observed spots at certain positions on the detection film. He won the 1914 Nobel Prize in physics for his discovery. This was a supporting evidence that X-rays have wave-like nature and can interfere with each other and are in fact electromagnetic radiations with wavelength in the order of Angstrom (10^{-10} m). He concluded that the structure of crystalline materials can be revealed by X-rays. In 1911 he conducted several experiments on crystalline materials. The outcome of the experiments was explained in the following year.

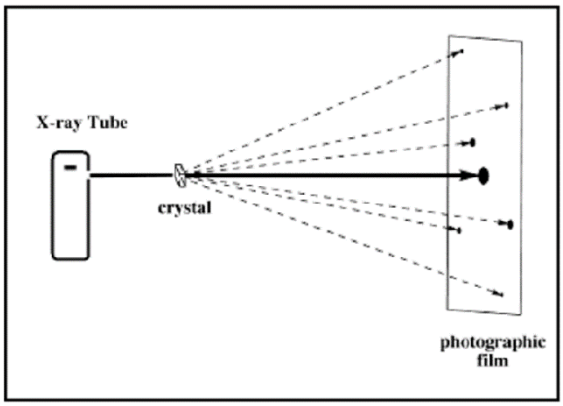

Figure 4.3 Left: Max von Laue (1879-1960) [86]. Right: schematic view of the X-ray experiment designed by Laue [87].

In 1912 William Henry Bragg and William Lawrence Bragg (father and son) solved the first crystal structure (NaCl) using X-ray diffraction. The son described the minimum condition for spots to appear. They assumed that crystals are made of equally spaced planes with distance d, where the atoms are located. When X-rays with wavelength λ are diffracted by the atomic planes, the resulting diffraction pattern on the detection screen contains constructive interference, forming Laue spots at a scattering angle θ. The condition to be fulfilled is:

$$n\lambda = 2d\,sin\,\theta \qquad 4.1$$

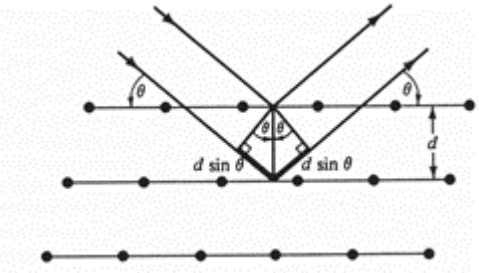

Figure 4.4 Schematic view of Bragg peak formation from scattered X-ray by a crystal.

The Braggs were awarded the 1915 Nobel Prize in physics for their remarkable contribution in X-ray crystallography. As they supposed, a crystal is considered to be made of a lattice and bases. The lattice is a periodic assembly of points in space and it represents the symmetry of the crystal structure. The lattice basis is a set of atoms or molecules placed on the lattice points. Considering the origin of the lattice is the position of one of the bases in the lattice, and r_i is the position of basis i with respect to the origin, we can move to any basis position r_j using vector $\vec{R}_n$:

$$\vec{r}_j = \vec{R}_n + \vec{r}_i \qquad 4.2$$

$\vec{R}_n$ is the combination of the basis vectors of the lattice $\vec{a}_1$, $\vec{a}_2$ and $\vec{a}_3$ with integer prefactors n_1, n_2 and n_3 and is formulated as follow:

$$\vec{R}_n = n_1\vec{a}_1 + n_2\vec{a}_2 + n_3\vec{a}_3 \qquad 4.3$$

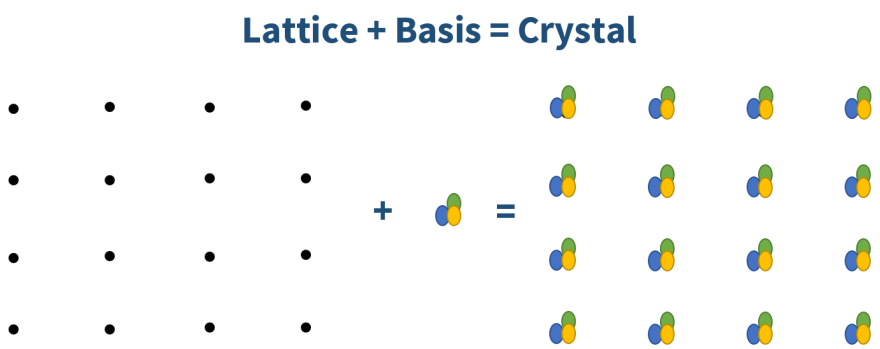

Figure 4.5 A crystal is made of set of basis placed on lattice points.

The periodic electron density of the crystal, described in the direct space, is revealed in a diffraction experiment by observing the diffraction pattern of the crystal and its intensity. The diffraction pattern is related to the crystal electron density by the Fourier transform and forms the reciprocal space. This means the reciprocal space is measured by the diffraction experiment taken in direct space. Therefore, Laue spots are formed by Fourier transform of the direct lattice which themselves form a lattice in the reciprocal space. The reciprocal lattice basis vectors $\vec{a}_1^*$, $\vec{a}_2^*$ and $\vec{a}_3^*$ are given as the following:

$$\vec{a}_1^* = 2\pi \frac{\vec{a}_2 \times \vec{a}_3}{\vec{a}_1 \cdot (\vec{a}_2 \times \vec{a}_3)} \qquad 4.4$$

$$\vec{a}_2^* = 2\pi \frac{\vec{a}_3 \times \vec{a}_1}{\vec{a}_1 \cdot (\vec{a}_2 \times \vec{a}_3)} \qquad 4.5$$

$$\vec{a}_3^* = 2\pi \frac{\vec{a}_1 \times \vec{a}_2}{\vec{a}_1 \cdot (\vec{a}_2 \times \vec{a}_3)} \qquad 4.6$$

Any position in the reciprocal lattice can reached given by:

$$\vec{G}_{hkl} = h\vec{a}_1^* + k\vec{a}_2^* + l\vec{a}_3^* \qquad 4.7$$

where h, k and l are integer numbers and are called Miller indices. The points in the real lattice and the reciprocal lattice are related as follow:

$$\vec{R}_n \cdot \vec{G}_{hkl} = 2\pi(n_1 h + n_2 k + n_3 l) = 2\pi\ (integer) \qquad 4.8$$

On the other hand, the diffraction pattern of an object is the distribution of the transferred momentum at different scattering angles θ. This concept can be better understood by the Ewald sphere which is described next.

In 1912 Peter Paul Ewald submitted his PhD thesis to the Ludwig Maximilian University of Munich (LMU) titled “Finding the optical properties of an anisotropic arrangement of isotropic resonators” [88], where he introduced “Ausbreitungskugel” or the sphere of reflection, today known as the Ewald sphere [89, 90]. One of the aims of his research was to find whether physical properties of materials could be directly related to the regular arrangement of space lattices [91]. He applied a geometric construction

to visualize the appearance of the reciprocal space and the diffraction pattern by making a relationship between the reciprocal space and the wavevector $\vec{k}$ of the incident beam where $\left|\vec{k}\right| = 2\pi/\lambda$ and θ is the scattering angle [92, 90].

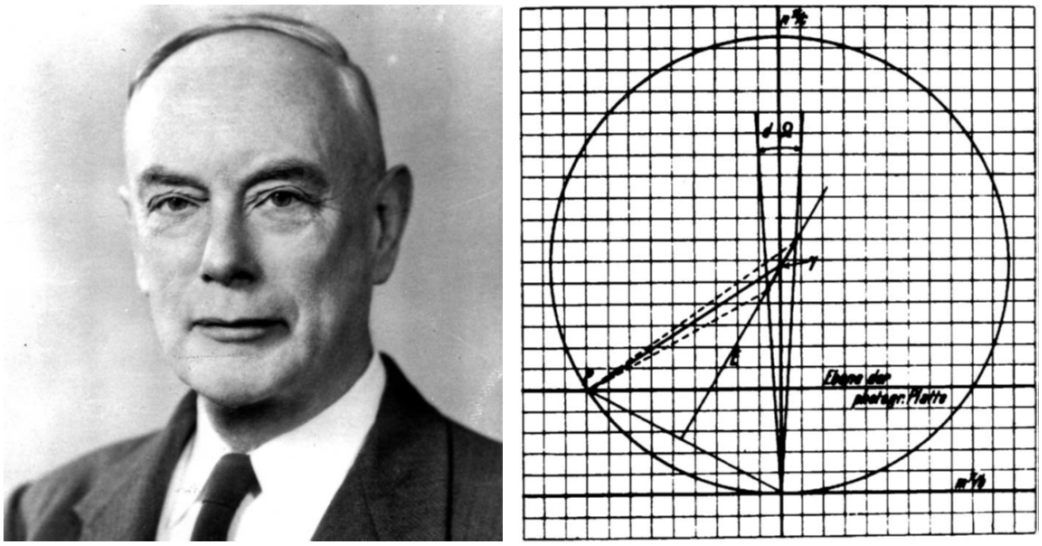

Figure 4.6 Left: Peter Paul Ewald (1888–1985). Right: The reciprocal lattice and Ewald construction. After Ewald (1913) [89, 91].

Let us assume that the incident plane wave of an X-ray with wave vector $\left|\vec{k}_i\right| = 2\pi/\lambda$, illuminates a crystal. The diffracted wave has a wave vector $\vec{k}_d$. For the elastic scattering, we have $\left|\vec{k}_i\right| = \left|\vec{k}_d\right| = 2\pi/\lambda$. The difference between the diffracted and the incident wave vectors, $\vec{q} = \vec{k}_i - \vec{k}_d$ is defined in the reciprocal space and is called the reciprocal vector.

Assuming a sphere which is centered on the diffracting crystal with radius $\left|\vec{k}_i\right|$, if any of the reciprocal lattice points fall on the Ewald sphere, then the Laue condition is fulfilled, and a diffraction peak can be observed [93]. In other words, Laue spots are visible when $\vec{q} = \vec{G}_{hkl}$. This is the Laue condition for the observation of diffraction from a crystalline lattice, which is equivalent to the Bragg's law. Therefore, the reciprocal lattice points are the values of momentum transfer where the Bragg diffraction condition is satisfied. Diffraction occurs if the scattering vector equals a reciprocal lattice vector [94].

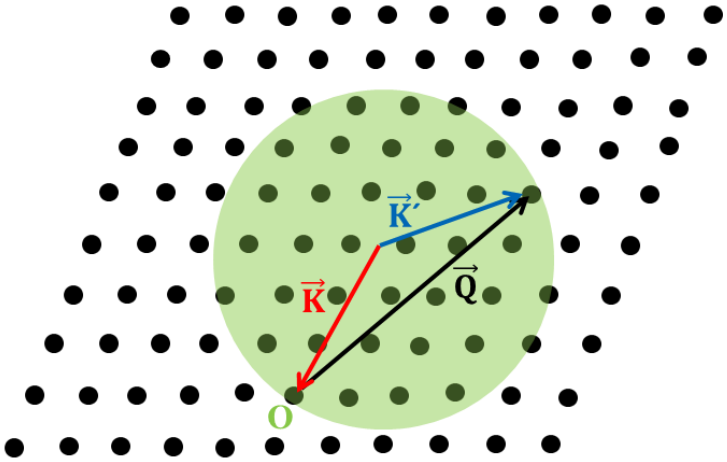

Figure 4.7 The radius of the Ewald sphere is given by the incidence wave vector $\vec{K}$. A Bragg diffraction peak is observed with wave vector $\vec{K'}$ only if a reciprocal lattice point is on the sphere [95].

Here we have assumed that the interaction between X-rays and crystal is weak, and a second or a third order scattering does not occur inside the crystal. Known as the kinematical approximation, this assumption simplifies the problem in hand. However, the assumption breaks down when dealing with perfect macroscopic crystals, where multiple scattering effects are important. These phenomena are described by the dynamical scattering [24] which is beyond the scope of this work.

From a large set of intensities scattered from a given crystal it is possible to deduce the positions of the atoms in the direct space. This method can be generalized to crystals containing small or even large molecules. Indeed, these methods have had great impacts on our knowledge of molecular structure. This was the birth of crystallography, which is the science of obtaining atomic and molecular structures of materials. More than 95% of our knowledge about molecular structures come from X-ray diffraction studies [24].

4.1.2 Sources and Synchrotrons Radiation

For nearly a century, the main sources of X-ray production were the X-rays tubes. In 1947 a synchrotron radiation facility was developed by General Electric as a new method for producing X-rays [96]. This development was followed by the invention of free electron laser. Since the experiments of this work were performed in a synchrotron radiation facility, here we describe how such a facility works.

In the 1970s, scientists discovered that charged particles which are emitting synchrotron radiation while circulating in storage rings are better sources for X-rays than X-ray tubes. Since then, synchrotron radiation sources have been received tremendous attention and efforts to be gradually developed into the third-generation synchrotron sources.

In a synchrotron source, a magnetic field is applied to charged particles e.g., electrons or positrons. This leads the particles to travel at relativistic speed with constant energy, along a curved paths [24, 93, 97, 98]. While passing a bending magnet located

at defined positions within the storage ring, the accelerated electrons emit high-energy X-rays. This radiation leaves tangentially the storage ring and can be sent to the experimental beamlines [97, 98].

There are three kinds of magnets that are used to make the necessary magnetic fields in the synchrotron: bending magnets, wigglers and undulators. In bending magnets, a simple dipole structure is used to constrain the electrons in a curved path. The emitted radiation is extremely intense, and contains a wavelength range from the infrared to the soft and hard X-ray[1] regions of the electromagnetic spectrum [99]. High-field wiggler magnets are often used as a source to increase the flux at shorter wavelengths. A wiggler can be considered as a sequence of bending magnets of alternating polarities, which gives a 2N enhancement in the flux, where N is the number of poles.

Undulators consist of periodic magnetic arrays, which cause small electron deflections that in magnitude are comparable to the natural emission angle of the synchrotron radiation. The radiations emitted at various poles interfere coherently, resulting in the emission of a pencil-shaped beam, peaked in narrow energy bands at the harmonics of the fundamental energy. For N poles, the beams opening angle is decreased by $N^{1/2}$ and the intensity per solid angle increases as N^2 [99].

A synchrotron radiation has some advantages over radiations from conventional sources. Firstly, it has a high resolution in measurement due to its spatial precision. This radiation has high degree of polarization with a very broad spectrum which covers a continuous spectral range from the infrared up to the hard X-ray region and gives the users a choice to select the wavelength required for their experiment. Secondly, the synchrotron radiation has a pulsed time structure, with exceedingly short pulse lengths, which enables us to carry out experiments as fast as tens of picosecond [100]. Thirdly and the most important advantage of the synchrotron radiation is the high intensity of the beam, which allows for rapid experiments for diffraction from weakly scattering crystals. On the other hand, there are some disadvantages associated with the use of synchrotron radiation; a storage ring has to be erected to collect the beam, which is both time consuming and costly [100]. It is also access limited and is accessible baes on successful experimental proposal.

The first visual observation of synchrotron radiation was in 1948 from the General Electric synchrotron in the USA during an investigation into the design and construction of accelerators suitable for the production of very high energy electrons. Afterwards, there was a growing interest in building accelerators which are optimized for synchrotron radiation production around the world [101]. Today, there are four active synchrotron radiation sources in Germany: BESSY (Berliner Elektronenspeicherring-Gesellschaft für Synchrotronstrahlung m.b.H.) in Berlin, DELTA (Dortmunder Elektronen Speicherring Anlage) in Dortmund, DESY (Deutsche Elektronen-Synchrotron) in Hamburg, and ANKA (Angströmquelle Karlsruhe) in Karlsruhe which is not accessible to public and provides only internal access.

[1] X-rays with high photon energies above 5–10 keV (below 0.2–0.1 nm wavelength) are called hard X-rays, while those with lower energy (and longer wavelength) are called soft X-rays [115].

To compare the beam quality of different sources, a parameter related to the characters of the beam is needed. A desired beam has a high intensity and a low collimation. Collimation is defined as the divergence of the beam during its propagation in milli-radian. The beam quality also depends on the size of the source (usually measured in mm^2), and on the one percent of the radiated energy calculated at the center of the energy spectrum. These parameters are combined to introduce a factor named ***brilliance***, which presents the beam quality:

$$Brilliance = \frac{number\ of\ photns/second}{divergence\ (mrad)^2\ .source\ area\ (mrad)^2\ .(0.1\%\ BW)}$$

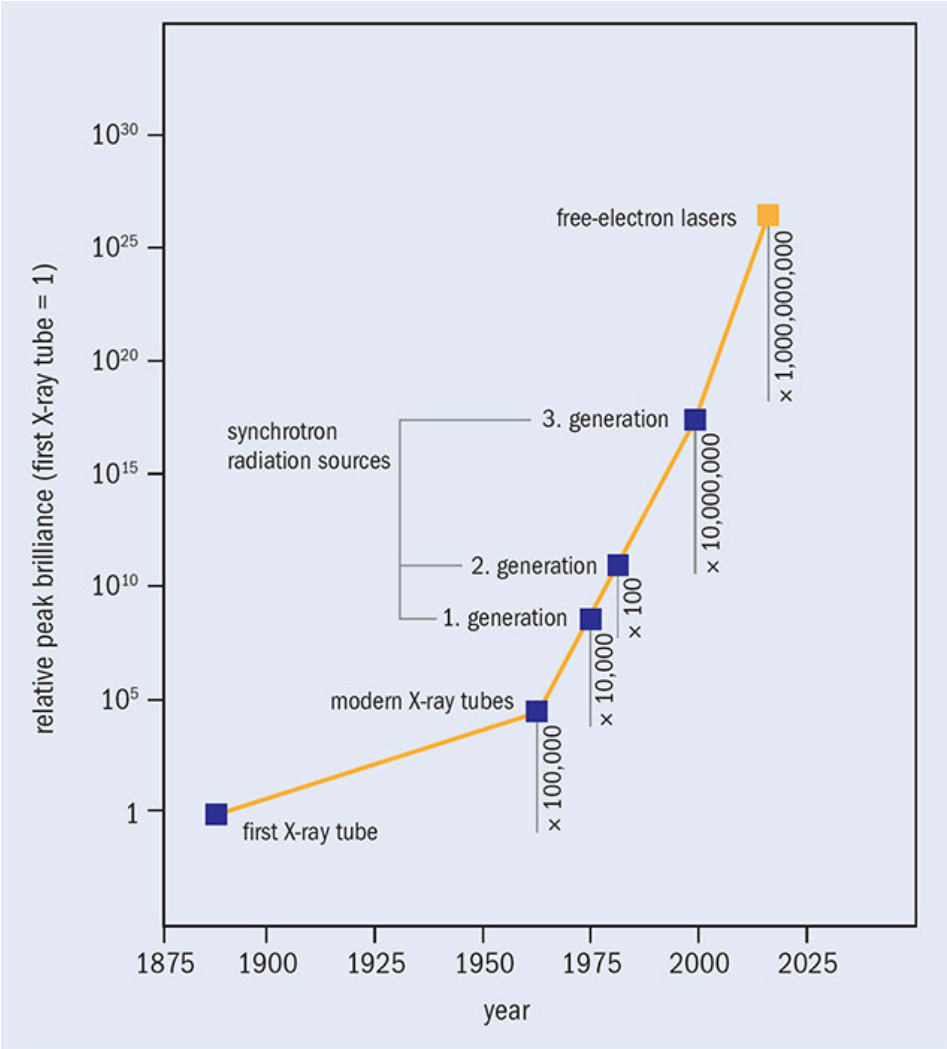

Figure 4.8 Improvement of the brilliance through the time since the discovery of the X-ray. Image credit: European XFEL [102]

As it can be seen from 4.8 the brilliance factor has improved through time.

4.2 Interaction of X-ray with Matter

From a quantum mechanical point of view X-rays are a collection of photons, each with momentum $\hbar\vec{k}$, that can interact with atoms. X-rays interact with matter in two distinct processes: scattering (containing reflection and refraction at interfaces as rays in the classical approach) and absorption.

An oscillating charged particle, such as an electron, can give rise to electromagnetic wave. The wavelength of the wave is related to the oscillation frequency of the electron. As an electromagnetic wave, X-rays are transverse waves composed of two sinusoidal components: electric field $\vec{E}$ and magnetic field $\vec{H}$. The two fields are perpendicular to the direction of propagation specified by the wavevector $k = |\vec{k}| = \frac{2\pi}{\lambda}$ where λ is the wavelength of the two oscillating fields.

$$\vec{E} = E_0 e^{i(\vec{k}.\vec{r}-\omega t)}, \qquad \vec{H} = H_0 e^{i(\vec{k}.\vec{r}-\omega t)}$$
$$\vec{E}.\vec{k} = 0, \qquad \vec{H}.\vec{k} = 0$$

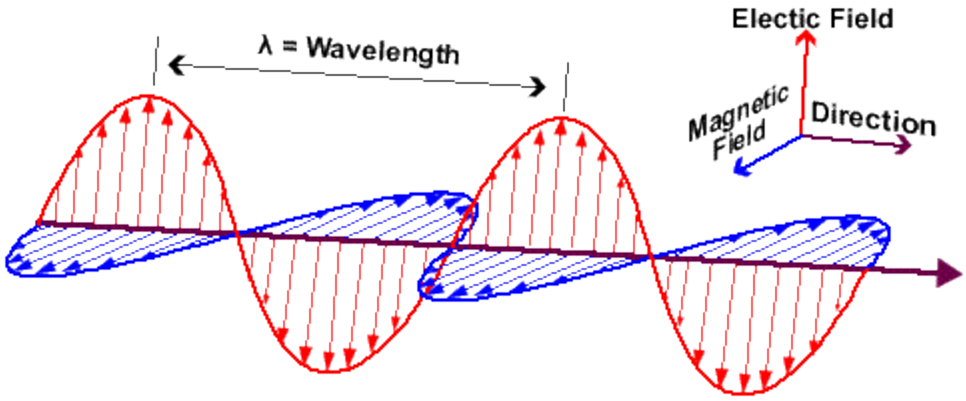

Figure 4.9 The propagation of the electromagnetic wave through space [103].

As a valid assumption in this work, the above equations represent linearly polarized monochromatic plane waves.

4.2.1 Scattering

Scattering of X-ray by an electron can be discussed in two distinct approaches. In the classical description, the electric field of the X-ray accelerates the electron which in turn radiates a wave at the same energy as the incoming X-ray beam. Therefore, the scattering is essentially an elastic process. From a quantum mechanical point of view, an inelastic scattering is also possible where a photon transfers some of its energy $\hbar\omega$ to an electron. As a result, the scattered photon has a smaller frequency. This process is known as the Compton Effect, and can only be explained quantum mechanically. It takes place when the energy of the X-ray is high enough to pass a threshold, which

excites the electrons that are deeply bound in the atom. The present work is dedicated to X-rays with energies in the range of 10-13 keV, which leaves us in the region of the elastic scattering.

The interaction of the X-rays with matter occurs via the electromagnetic force. The photon represents a periodically oscillating electric field which interacts with the electrically charged particles of the matter (the electrons and the protons). Thereby an incident plane wave with amplitude A_0, wave vector $\left|\overrightarrow{k_0}\right| = \frac{2\pi}{\lambda_0}$ and wavelength λ_0 excites the particles to vibrate with the same frequency. Therefore, the excited particles emit spherical waves via dipole radiation. Since the scattering process is elastic, the amount of the wavevector of the spherical waves is the same as the incident wave $\left|\overrightarrow{k_0}\right| = \left|\vec{k}\right|$. The total amplitude is the sum of the amplitudes of the spherical waves given by $A(\vec{q})$. The resulting intensity is given by $(\vec{q}) = |A(\vec{q})|^2$, which is observed in the far field limits on the detector and is related to the scattering angle 2θ. The scattering vector $\vec{q} = \vec{k} - \overrightarrow{k_0}$ is introduced in section 4.1.1 and as figure 4.10 suggests, it can be written as $|\vec{q}| = 2\left|\overrightarrow{k_0}\right| \sin(\theta) = 4\pi \sin(\theta)/\lambda_0$. Since the intensity of the scattered radiation depends inversely on the square of the mass of the scattering particle [24, 21], in general, protons' contribution to the scattering is neglected compared to the electrons' where the scattering is around 1840 times stronger [31].

As mentioned above, the detectable parameter in a scattering experiment is the intensity $I(\vec{q})$, which can be understood by the differential cross section, that is, the scattered flow of the spherical waves normalized to the incident flux of the plane waves in units of $[m^2]$. The differential cross section can be interpreted as a probability of scattering of a photon by a free electron into the solid angle $d\Omega$. In nonpolarized cases, the differential cross section for the scattering of an x-ray wave at a free electron is $\left(\frac{d\sigma}{d\Omega}\right)_e$ given by Thomson-Streuformel [24]:

$$\left(\frac{d\sigma}{d\Omega}\right)_e = \left(\frac{e^2}{4\pi\varepsilon_0 m_e c^2}\right)^2 \frac{1 + cos^2(2\theta)}{2} = r_0^2 \frac{1 + cos^2(2\theta)}{2} \qquad 4.9$$

where e is the elementary charge, m_e is the rest mass of the electron, ε_0 is a constant of medium, and c is the speed of light. In an X-ray synchrotron, the polarization direction of the generated radiation is horizontal. In this case $\left(\frac{d\sigma}{d\Omega}\right)_e = r_0^2$, and the total scattering length of the electron is derived by the classical electron radius:

$$(\sigma_e)_{total} = \int d\sigma_e = \int r_0^2 d\Omega = \frac{8}{3}\pi r_e^2 \qquad 4.10$$

Considering the classical radius of electron is $r_e = (2.818)10^{-15}\, m$, the total cross-section for the scattering of an X-ray photon by an electron results in $(\sigma_e)_{total} = 8/3\, \pi r_e^2 = (6.65)10^{-29}\, m^2 = 0.665$ barn[2], which is known as the Thomson scattering

[2] Barn is a unit to define the cross-section of scattering, which is equal to 10^{-28} m^2.

length. This value depends on the polarization of the incoming beam, but it is independent of its energy. This is because in this range of X-ray energy even the atomic electrons respond freely. This result breaks down for the lower energies of the electromagnetic wave such as the optical waves and the higher energies where resonant excitations of the electrons take place.

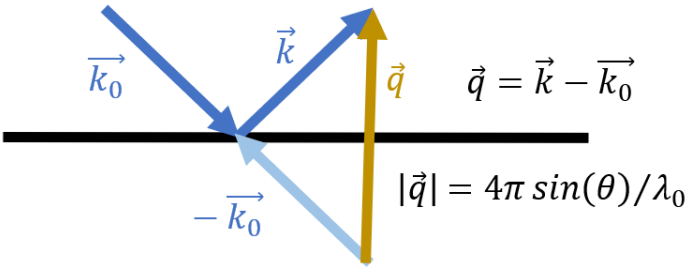

Figure 4.10 The magnitude of the scattering vector can be derived as $|\vec{q}| = 2|\overrightarrow{k_0}|\, sin(\theta) = 4\pi\, sin(\theta)/\lambda_0$.

The spherical waves generated by the electrons in the sample at the locations $\vec{r_i}$, contribute to the scattering amplitude $A(\vec{q})$, and are detected in the form of intensity in the far field limit. The scattering intensity is equal to the sum of all the scattering amplitudes squared, whose relative phase difference $\Delta\phi_i$ is $\vec{q} \cdot \vec{r_i}$.

$$A(\vec{q}) = -r_0 \int_{-\infty}^{\infty} \rho_e(\vec{r}) e^{-i\vec{q}\cdot\vec{r}} d\vec{r} \qquad 4.11$$

As discussed above, the proton interaction with the X-ray is neglected compared to that of the electrons and therefore an atom is considered to be the distribution of a collection of electrons with an electron density denoted by $\rho_e(\vec{r})$. Having phase shift $(\vec{k_i} - \vec{k_s}).\vec{r_j}$ with respect to the incident beam at the origin, the scattered radiation can be obtained by the superposition of the radiations scattered by the electron distribution at positions $\vec{r_j}$. Therefore, the total scattering length of an atom is related to the electron density as follow:

$$f_a(\vec{q}) = -r_0 \int_{-\infty}^{\infty} \rho_e(\vec{r}) e^{-i\vec{q}\cdot\vec{r}} d\vec{r} \qquad 4.12$$

with $\vec{q}$ is the scattering vector. The equation 4.12 shows that the scattering length of an atom is related to the Fourier transform of its electron distribution. Finally, the intensity is the squared of the amplitude and in this case it is given as follow:

$$I(\vec{q}) = A(\vec{q})A^*(\vec{q}) = f_a(\vec{q})f_a^*(\vec{q}) \qquad 4.13$$

In an atom, electrons are bound in discrete energy levels. If the energy of the X-ray photons is smaller than the energy of the most tightly bound electrons, the scattering length of the atom will be reduced. This leads to the correction of the atomic scattering length, which in turn gives rise to the parameters related to the absorption and refractive index explained in the following section.

4.2.2 Refraction and Reflection

Refraction and reflection are two scattering phenomena. they occur when a traveling wave in a medium meets the surface of another medium. From a macroscopic point of view, electromagnetic waves are refracted or reflected on the interference of two different media. Each medium has its own refractive index n defined as:

$$n = 1 - \delta + i\beta \qquad 4.14$$

For the X-ray radiation, δ has a value of around 10^{-5} for solids and around 10^{-8} for air. The value of β is even smaller than δ. The Snell's law shows how the angle of the refracted wave with respect to the surface deviates from that of the incident X-ray. The Snell's law is given as follow:

$$cos\ \alpha_{in} = n\ cos\ \alpha_{ref} \qquad 4.15$$

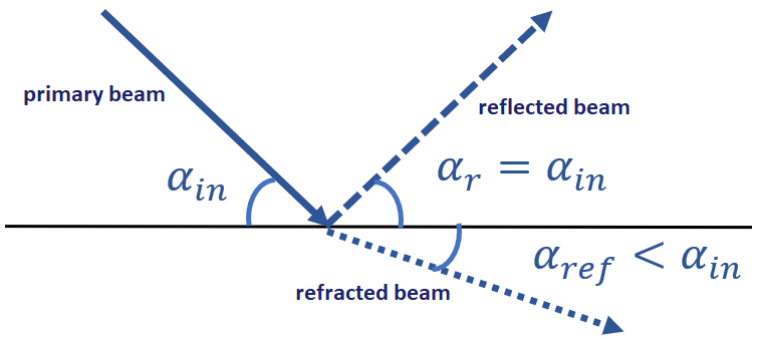

Figure 4.11 Reflection and refraction of X-ray at the surface of two media.

Due to the equations 4.14 and 4.15 and typical values of δ, one can conclude that the refractive index is a value smaller than unity for X-rays, and the wave gets closer to the surface when it enters a denser medium. Consequently, there is a critical angle for the incident X-ray below which the beam does not enter the denser material, and total external reflection occurs. It can be proven that the critical angle is related to the refractive index as:

$$\alpha_c \sim \sqrt{2\delta} \qquad 4.16$$

As it will be explained in chapter 6, δ is a function of the electron density of the surface and therefore α_c represent an important physical characteristic of the medium.

4.2.3 Absorption

When X-ray illuminates a sample, a portion of the photons transfer their energies to the bound electrons of the atoms. The photons are absorbed by the electrons and leave ionized atoms behind. The process is known as the photoelectric absorption.

The parameter related to this phenomenon is called the linear absorption coefficient μ, which is a property of the medium, and its value varies with the energy of the incident X-ray beam. Considering dI is the drop in the intensity of the incident X-ray

passing through an infinitesimally thin layer of the medium dz, the intensity at a given layer is given by:

$$I(z) = I_0 e^{-\mu z} \qquad 4.17$$

The value of μ is related to the number of absorption events which in turn relates to the atomic number density ρ_{at} and the absorption cross-section σ_a. Therefore, the absorption coefficient is given as follow:

$$\mu = \rho_{at}\sigma_a = \frac{\rho_m N_A}{M}\sigma_a \qquad 4.18$$

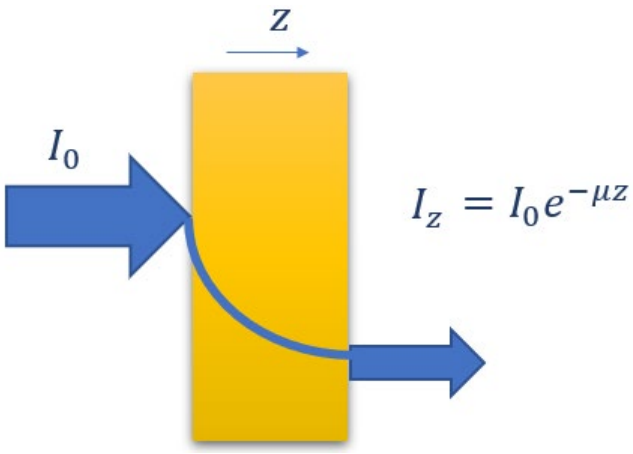

Figure 4.12 When X-ray beam passes a medium, its intensity drops through absorption.

where N_A, ρ_m, and M are the Avogadro's number, mass density, and molar mass respectively. If the material is a composition of different atoms, then the linear absorption coefficient is given by the summation of the absorptions of all atoms:

$$\mu = \sum_i (\rho_{at})_i (\sigma_a)_i \qquad 4.19$$

For every atom there are specific value of the incident beam energy that maximizes the probability that the electrons are expelled from the atom. These energies are comparable to the boundary energies of the electrons inside that atom. These are referred to as the absorption edges which are the fingerprints of the atomic numbers [24].

There is another phenomenon that happens in the concept of absorption. When an electron leaves its atom in an unstable state, the remaining electrons in the atom are rearranged by first filling up the states with higher boundary energies. As a result, they lose energy and emit fluorescence radiation with a larger wavelength than the incident beam [24]. This will appear as a constant background on the detector.

4.3 Small Angle X-ray Scattering (SAXS)

Small Angle X-ray Scattering (SAXS) is the main method of measurement in this study. This is when the X-ray illuminates the sample in the transmission geometry. It means that the scattering pattern is recorded by the detector in the direction of the incident beam (see figure 4.13). Therefore, the sample and the detector are in the direction of

the primary beam. Measurements are made at very small angles, typically in the range of $2\theta = 0.1^{\circ} - 5^{\circ}$. As explained in section 4.2.1, since we assume elastic scattering, the scattering angle θ and the scattering vector $|\vec{q}|$ have the following relationship:

$$|\vec{q}| = 4\pi\, sin(\theta)/\lambda_0 \qquad 4.20$$

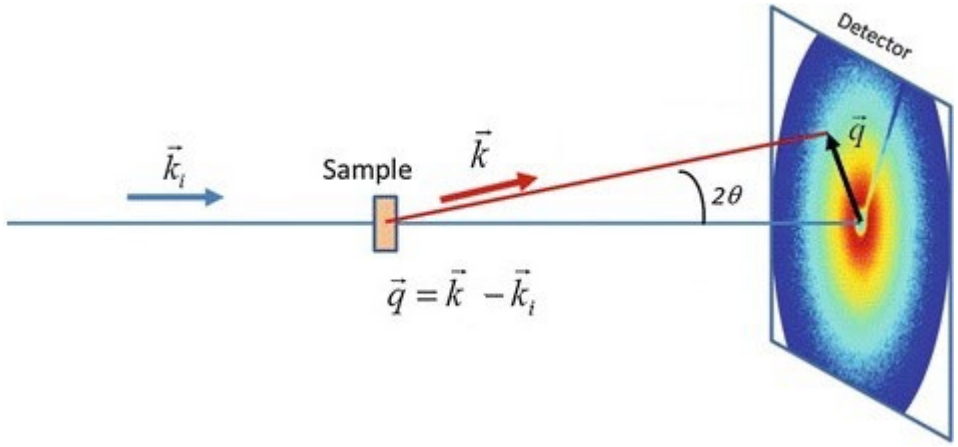

Figure 4.13 Schematic view of SAXS experiment [104].

From Bragg equation it is clear that in order to study the structures in larger scales we need to investigate the diffraction pattern at smaller angles. This is the main motive for conducting measurements using the SAXS method for investigating the shape and the size of the bulk probe.

SAXS is a strong measurement method for acquiring information on the structure of the probe, such as the shape and the size in the scale of few to hundreds of nanometers. The particles of the probe which are illuminated by the X-ray under the SAXS setup are the scatterers which give rise to the scattering pattern on the detectors. These particles are not necessarily identical. They might differ in size and shape. The SAXS intensity presents the average structure of the illuminated volume. Therefore, local details are not visible unless they are highly pronounced in the whole sample and are therefore detectable in the measurement. The illuminated volume of the probe contains different scaled substructures. As will be discussed in section 4.3.4, substructures with larger scales dominate the intensity because their contributions in the intensity are modulated by the squared of their volume.

When X-ray illuminates a sample in the SAXS mode, every atom in the radiated volume emits a spherical wave from its position. Since this is a Thomson scattering, and the waves here are synchronized plane waves, an interference pattern is obtained and can be detected by the detector. The final diffraction pattern is the interference of the radiation from many atoms of the probe. The observed scattering pattern on the detector is the square of the sum of the amplitudes of all the waves radiated by all the atoms. This pattern oscillates in such a way that it reveals characteristics of the shape and the size of the probe, which is referred to as the ***form factor*** of the probe. However, in most experiments, many particles are illuminated, and therefore the scattering pattern is related to the form factor of one particle only if:

1- All the illuminated particles in the probe are identical (monodisperse sample) and
2- The distances between the particles are large compared to the wavelength (dilute system)

If particles are not identical the sample possesses ***polydispersity***.

In samples with a specific arrangement of the position of the particles, even in the short-range, another factor should be considered which is related to particle-particle interaction. This factor is also contributing when the particle density is high such that their distances are in the order of the size of the particles and the interference pattern contains contributions from the neighboring particles. This additional part is known as the ***structure factor***, which contains information on the position of the particles with respect to each other.

4.3.1 Form Factor

As mentioned in section 4.2.1, the scattering amplitude $A(\vec{q})$ arises from the in-phase summation of the spherical waves. This can be described in the continuous approximation with a Fourier transformation of the contrast of the electron density distribution function.

$$A(\vec{q}) = \int_{-\infty}^{\infty} \Delta\rho_e(\vec{r}) e^{-i\vec{q}\cdot\vec{r}} dV \qquad 4.21$$

Equation 4.21 shows that if the contrast $\Delta\rho_e$ is not position dependent and is consequently a constant value, the amplitude can be considered as the phase difference in volume V multiplied by the $\Delta\rho_e$. This happens for instance when a particle with ρ_{e1} is located in an environment with ρ_{e2} such that $\Delta\rho_e = \rho_{e1} - \rho_{e1}$ and the boundaries between the two materials are sharp. The form factor of the isolated particle with volume V_p is defined as:

$$F(\vec{q}) = \frac{1}{V_p} \int_{V_p} e^{-i\vec{q}\cdot\vec{r}} dV_p \qquad 4.22$$

This factor depends on the morphology of the particle. The form factor of an arbitrary particle is the sum of the phase shifts of different fragments of the particle, which contribute in the scattering amplitude weighted by the electron density difference.

The analytical solution for the equation 4.22 is feasible for only in a few cases. In other cases, the integral should be solved using numerical methods. The analytical solution of three cases is given below.

The form factor of a sphere with radius R is given by:

$$F_s(\vec{q}) = \frac{1}{V_s} \int_0^{\pi} \int_0^{2\pi} \int_0^{R} e^{-i\vec{q}\cdot\vec{r}} r^2 \sin\theta \, dr d\varphi d\theta \longrightarrow |F_s(\vec{q})|^2 = \left(\frac{3J_1(qR)}{qR}\right)^2$$

The form factor of a disc with radius R:

$$F_d(\vec{q}) = \frac{1}{V_d}\int_0^{2\pi}\int_0^{R} e^{-i\vec{q}\cdot\vec{r}} r\,dr\,d\varphi \longrightarrow |F_d(\vec{q})|^2 = \frac{2}{(qR)^2} - \frac{2J_1(2qR)}{(qR)^3}$$

And the form factor of a rod with length L.

$$F_r(\vec{q}) = \frac{1}{V_r}\int_0^{L} e^{-i\vec{q}\cdot\vec{r}}\,dr \longrightarrow |F_r(\vec{q})|^2 = \frac{2\int_0^{qL}\frac{\sin t}{t}dt}{qL} - \frac{4\sin^2(qL/2)}{(qL)^2}$$

In section 4.3.4 we will see that in a dilute system dilute where the structure factor is equal to unity, the intensity for a monodisperse system is given by:

$$I(\vec{q}) = \left(\Delta\rho_e V_p\right)^2 |F(\vec{q})|^2 \qquad 4.23$$

4.3.2 Polydispersity

So far, we have assumed a monodisperse dilute, that is all particles in the dilute are identical with the same shape and size. An example of such a system is the protein dilute. However, in most cases this assumption is not valid, and the system is therefore polydisperse. If there are differences in the size or in the shape of the particles, the form factor is related to the aggregation of the form factors of all the particles, and therefore the scattering pattern is the average pattern of the particles.

There should be a function $D(\vec{r})$ with which the distribution of the size of the particles can be described. In this case the intensity in equation 4.23 is modified to:

$$I(\vec{q}) = (\Delta\rho_e)^2 \int_0^{\infty} D(\vec{r})\, V_p(\vec{r})\, |F(\vec{q},\vec{r})|^2\, dr \qquad 4.24$$

4.3.3 Structure Factor

In a concentrated system of particles, the ***structure factor*** $S(\vec{q})$ describes the contribution of particle interaction in the diffraction pattern.

Particle-particle interaction in a short-range order means an increment in the probability of finding a next neighboring particle at a specific distance. At short distances the positions of the particles with respect to the origin are relatively well-defined as if they are placed on lattice points. However, at larger distances the positions of the particles are not predictable anymore and are therefore more random with respect to the origin. In such a random system, the concentration effect is visible at the small angles of the SAXS pattern through the structure factor as a drop in the intensity at the beginning of the curve.

On the other hand, when particles of a system are aligned in a highly ordered periodic arrangement, there is a long-range order of particles in real space. This appears in the SAXS diffraction pattern as a set of pronounced peaks which are the Bragg peaks at

well-defined values of the scattering vector. The Bragg peaks in this case are more visible and non-vanishing at the high values of q.

The structure factor $S(\vec{q})$ for two-dimensional hexagonal arrangement and a for a random system will be discussed in chapter 5.

4.3.4 SAXS Intensity

The scattering intensity is the observable that is measured on the detector. the electron density contrast ($\Delta\rho_e(\vec{r}) = \rho_e(\vec{r}) - \rho_{min}$, with $\rho_{min} = min\big(\rho_e(\vec{r})\big)$ being the lowest electron density of the scattering volume) of the sample gives rise to such measurable scattering on the detector. The entire electron density distribution function can be split into two parts:

$$\rho(\vec{r}) = \rho_F(\vec{r}) \otimes \rho_s(\vec{r}) \qquad 4.25$$

where $\rho_F(\vec{r})$ is the electron density distribution with respect to the form of particles, such as a sphere, disk, rod, etc. If the positions of these particles are correlated then $\rho_S(\vec{r})$ is defined as the particle-particle interaction to indicate any correlation between the position of the particles. In the language of crystallography, when the electron density distribution describes a crystal, $\rho_S(\vec{r})$ stands for the lattice, and $\rho_F(\vec{r})$ stands for the basis. Recalling that the scattering amplitude is the Fourier transform of the electron density, according to the convolution theorem, the final scattering amplitude can be expressed as the product of both contributions.

$$A(\vec{q}) = A_F(\vec{q}) \cdot A_S(\vec{q}) \qquad 4.26$$

with $A_F(\vec{q})$ being the scattering amplitude contribution of the form, and $A_S(\vec{q})$ being the contribution of the correlation or the structure. This results in the scattered intensity as to the square of sums

$$I(\vec{q}) = |A(\vec{q})|^2 = S(\vec{q}) \cdot |F_F(\vec{q})|^2 \qquad 4.27$$

where $S(\vec{q})$ is the structure factor which shows the contribution of the particle-particle interaction in the intensity. Equation 4.27 expresses that the intensity maxima are given by the structure factor and their relative heights are resulted by the modulation of the contribution of the form acting as an envelope.

The scattering usually takes place on a total volume V_P of the sample, which is determined by the collimation and consequently by the cross-sectional profile of the primary beam and the sample thickness. In addition, a typical measurement time for laboratory equipment ranges from several minutes to hours, depending on the scattering power of the sample. Therefore, the scattered intensity represents an ensemble average as well as a time average of the sample. As a result, the reflected length scale in the scattering pattern is given by the average length scales of the contributing particles to the scattering with respect to their distribution, e.g. the average radius of the spheres illuminated by the X-ray. This results in the general scattering intensity of the sample [21]:

$$\langle I(\vec{q})\rangle = (b_e \cdot \Delta\rho_e \cdot V_P)^2 \cdot N \cdot (\langle F(\vec{q})\rangle^2 S(\vec{q}) + \langle F(\vec{q})^2\rangle - \langle F(\vec{q})\rangle^2) \qquad 4.28$$

with the dimensionless function $F(\vec{q}) = A_F(\vec{q})/b_e\Delta\rho_e V_F$ as the form factor. V_F is the mean volume of a scattering particle with the number of electrons in this volume $N_e = \rho_e V_F$.

As can be seen from equation 4.28, the sample ensemble scatters with the mean form factor and the structure factor. Due to the deviations from the mean of the form factor, a q-dependent background $\langle F(\vec{q})^2\rangle - \langle F(\vec{q})\rangle^2$ called Laue scattering, appears. Furthermore, the intensity is determined by the electron density contrast $\Delta\rho_e(\vec{r})$, the sample volume V_P, and the number of scattering particles N described by the form factor $F(\vec{q})$.

As equation 4.28 shows, the SAXS signal strength is proportional to the square volume of the scattering particles. Therefore, the small scatterers are nearly invisible in the presence of the larger scatterers. Consequently, when scattering occurs from a sample with multi size scattering objects, the scattering pattern is dominated by the larger scatterers.

The intensity function cannot be used to completely reconstruct the electron distribution of the sample. The reason is that the most phase shifts of the radiation are lost by the formation of the square of sums. However, due to its typical scattering angle range of a few degrees, the small angle scattering can be used to measure the length of the sample at molecular level and above, i.e., approximately between few to hundreds of nanometers.

4.3.5 Guinier Analysis and Radius of Gyration

Consider a system of randomly ordered spheres at positions far from each other forming a dilute system. Using the spherical form factor, the intensity is given by:

$$I_s(\vec{q}) = \left(\Delta\rho_e V_s \frac{3J_1(qR)}{qR}\right)^2 \qquad 4.29$$

It can be proven that at small values of q where $qR \to 0$, the intensity tends to the following value [24]:

$$I_s(\vec{q}) \approx (\Delta\rho_e V_s)^2 e^{-q^2R^2/5} \qquad 4.30$$

Therefore, at the very beginning of the intensity curve, $\ln I_s$ vs q is a straight line with slope $R^2/5$. This means that the SAXS intensity in the limits of small values of q gives the radius of sphere. This result, which was first derived by Guinier, is valid for every dilute system and can be expanded to other shapes of particles in the concept of ***radius of gyration***. It is when the radius of the sphere is replaced by a more general characteristic size of the particles in the dilute system. It is defined as the root-mean-squared distance from the center of gravity of the particle. When the scattering length distributed uniformly for the particle, the radius of gyration R_g is given by:

$$R_g^2 = \frac{1}{V_p}\int_{V_p} r^2 dV_p \qquad 4.31$$

In a more general case where the electron density is position dependent, the above formula extends to:

$$R_g^2 = \frac{\int_{V_p} \rho_{sl}(\vec{r})\, r^2\, dV_p}{\int_{V_p} \rho_{sl}(\vec{r})\, dV_p} \qquad 4.32$$

This equation is mostly calculated by numerical methods, but it is straightforward to show that for a sphere we have $R_g^2 = \frac{3}{5}R^2$. We can therefore rewrite the equation 4.30 in a more general form:

$$I_p(\vec{q}) \approx \left(\Delta\rho_e V_p\right)^2 e^{-q^2 R_g^2/3} \qquad 4.33$$

This formula is valid for all types of particles, and R_g^2 has been proven to be $\frac{1}{2}R^2$ and $\frac{1}{12}L^2$ for disks and rods respectively.

4.3.6 Porod Analysis

Here we consider another limit of the scattering vector in a dilute system of spheres. When the relevant wavelength is small compared to the particle size we can consider that $qR \gg 1$. Then the spherical form factor limits to:

$$I_s(\vec{q}) = \frac{(3\Delta\rho_e V_s)^2}{2q^4R^4} = \frac{2\pi(\Delta\rho_e)^2}{q^4} S_s \qquad 4.34$$

where S_s is the surface area of the sphere. In Porod regime, the double logarithmic plot of $\frac{I_s}{S_s}$ and q falls off with an average slope of -4 for a spherical shape. In this limit, the intensity is sensitive to the surface and therefore to the shape of the particle. Same as the Guinier analysis, this result can be generalized to other cases. The slope is -2 and -1 for disks and rods respectively.

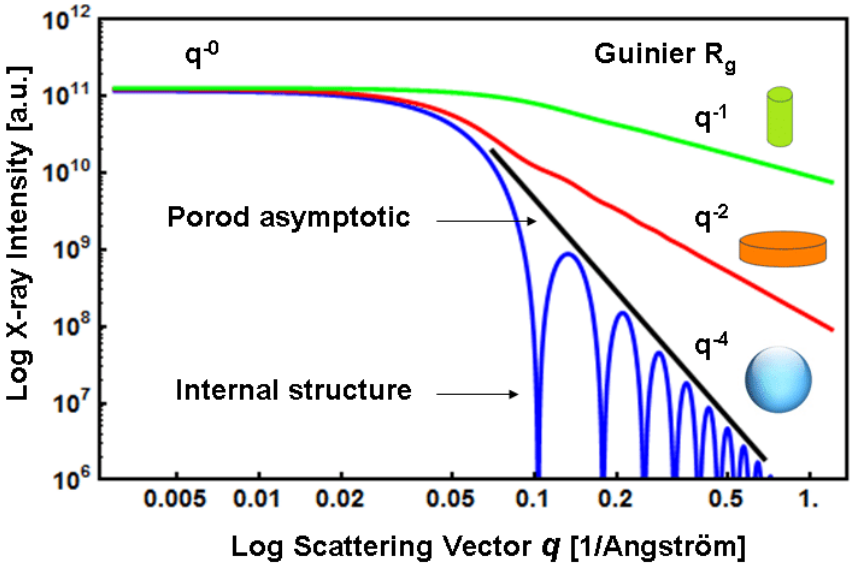

Figure 4.14 In Porod limit the slope of the intensity curve is related to the shape of the particle [105].

4.4 Optical Transmission, the Classical Approach

Here, we represent the optical twin of the SAXS experiment in the field of optics, where the classical approach of waves and sinusoidal displacements are considered. The optical transmission phenomenon is studied based on classical point of view which considers the interference of wave-like light. On the other hand, the SAXS phenomenon is studied on the base of particle interactions. Despite different points of views, the two events appear to have similar conceptual properties. In both cases, the intensity is the product of the factor resulted from the particle shape and a factor resulted from the arrangement of the particles. As we see in the following sections, similar to the case of SAXS, the size of the scattering slits as well as their distances can be derived from the intensity of the interference pattern.

4.4.1 Young's Experiment and Grating

When multiple waves pass through a given space at the same time, the resulting wave at any position is given by the summation of the individual waves at that position. This phenomenon is called the superposition of the waves. In 1801 Thomas Young performed an experiment known as the double slit experiment. In his experiment a point-like monochromatic light source illuminates a plane containing two parallel slits. The two slits act as point-like sources of light and form an interference pattern on the detection screen in front of them.

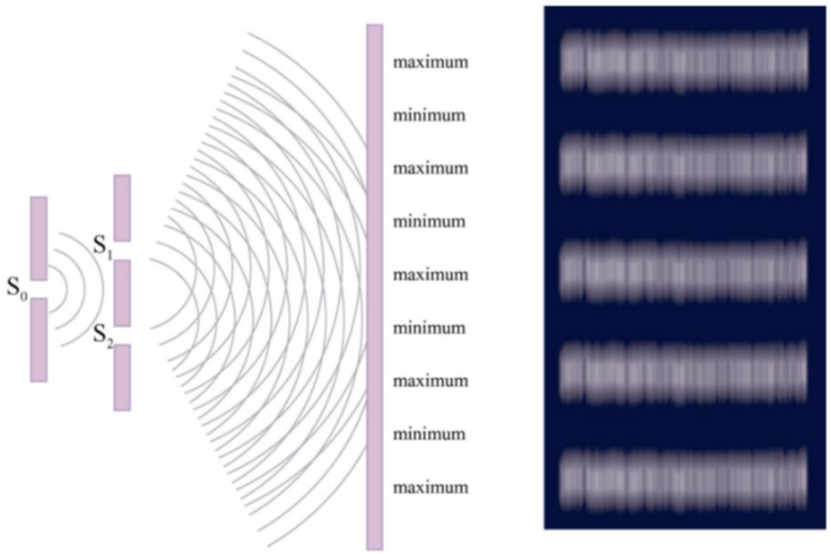

Figure 4.15 Young's double slit experiment [106].

The interference pattern occurs on the detection screen because the following conditions are satisfied for the two sources:

1- The two sources are coherent sources, which means the phase shift between the waves stay constant.
2- The two sources emit monochromatic waves, which means each wave consists of only one wavelength

In this experiment a sequence maxima and minima are formed, from which the distance between the slits can be extracted. It can be proven that the path difference

between the two waves is related to the wavelength and to the distance between the sources. For maxima we have:

$$d\ sin\ \theta_{max} = n\lambda \qquad n = \cdots, -1, 0, 1, \ldots \qquad 4.35$$

As the detectable feature, the intensity is given by the time average on the summation of the electrical fields squared:

$$E_1 = E_0 \sin(\omega t), \qquad E_2 = E_0 \sin(\omega t + \varphi), \qquad \varphi = \frac{2\pi d}{\lambda}\sin\theta$$

$$I = \langle\left(\vec{E}_1 + \vec{E}_2\right)^2\rangle = \langle E_1^2\rangle + \langle E_2^2\rangle + 2\langle\vec{E}_1.\vec{E}_2\rangle \qquad 4.36$$

The term $\langle\vec{E}_1.\vec{E}_2\rangle$ is vanishing for incoherent waves when averaging over time. While it is a position dependent function for coherent waves, and they can therefore produce the interference pattern. Since $\langle E_1^2\rangle = \langle E_2^2\rangle = E_0^2/2 = I_0$, it can be proven that for coherent waves:

$$I = 4I_0\ cos^2\left(\frac{\varphi}{2}\right) = I_{max}\ cos^2\left(\frac{\pi d}{\lambda} sin\ \theta\right) \qquad 4.37$$

where $I_{max} = 4I_0$ is only valid for a two-slit system.

Expanding this experiment and calculations to N-slits grating, it can be shown that the following relationship for a grating is given as follow [107]:

$$I = N^2 I_0 \frac{sin^2\left(N\frac{\pi d}{\lambda} sin\ \theta\right)}{sin^2\left(\frac{\pi d}{\lambda} sin\ \theta\right)} = I_{max}\frac{sin^2\left(N\frac{\pi d}{\lambda} sin\ \theta\right)}{sin^2\left(\frac{\pi d}{\lambda} sin\ \theta\right)} \qquad 4.38$$

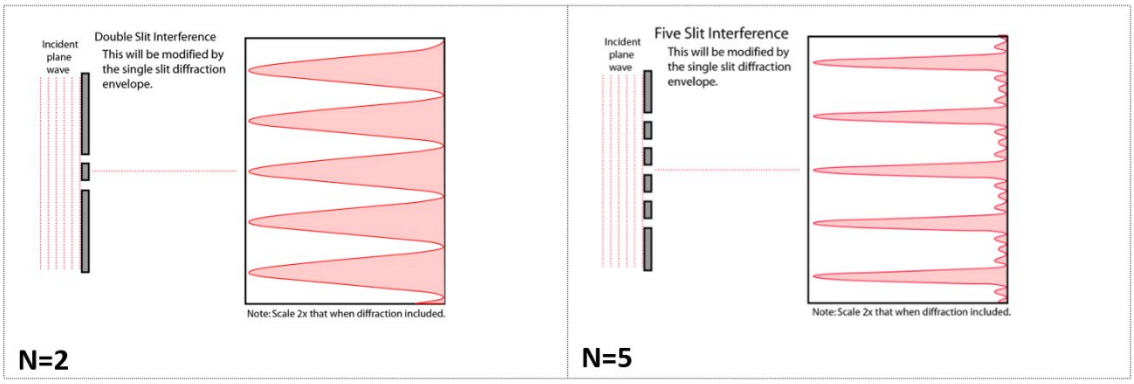

Figure 4.16 schematic view of interference pattern for 2-slit and 5-slit gratings [108].

Figure 4.16 shows the schematic view of the interference pattern for 2-slit and 5-slit gratings.

4.4.2 Grating with Diffracting Slits

So far, we have treated the slits as point-like sources by assuming their width to be exceedingly small. In fact, each slit affects the interference pattern by a phenomenon known as ***diffraction***. As Huygens-Fresnel principal says: "*Every unobstructed point on a wavefront will act as a source of secondary spherical waves. The new wavefront is the surface tangent to all the secondary spherical waves.*" Therefore, every part of the slit serves as a point-source, and the whole slit will produce the interference pattern

by itself, which is known as the ***diffraction pattern***. If the width of a single alit is given by w, then the intensity of the slit diffraction pattern is given by:

$$I = I_0 \left(\frac{sin\left(\frac{\pi w}{\lambda} sin\,\theta\right)}{\frac{\pi w}{\lambda} sin\,\theta} \right)^2 \qquad 4.39$$

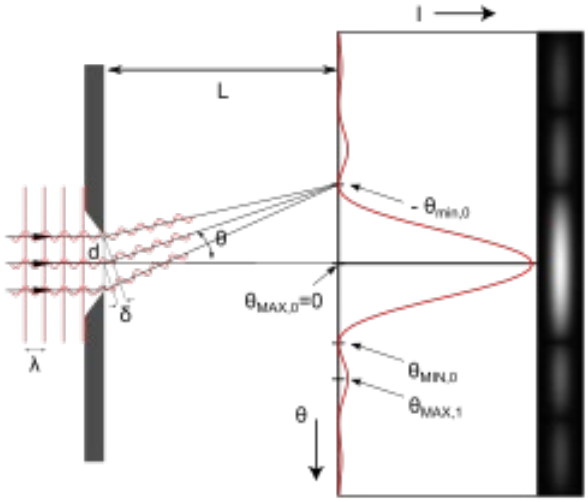

Figure 4.17 when the light source is large, then every part of it acts as point-like source and an interference is caused by the shape of the slit. This kind of interference is known as diffraction.

Let us consider a grating which contains many slits, each having width w apart from each other by distance d. The final pattern of interference for this system includes the ***diffraction factor*** produced by the slits and the ***interference factor***. The intensity of the total pattern is the product of the two functions:

$$I = I_{max} \left(\frac{sin\left(N\frac{\pi d}{\lambda} sin\,\theta\right)}{sin\left(\frac{\pi d}{\lambda} sin\,\theta\right)} \right)^2 \left(\frac{sin\left(\frac{\pi w}{\lambda} sin\,\theta\right)}{\frac{\pi w}{\lambda} sin\,\theta} \right)^2 \qquad 4.40$$

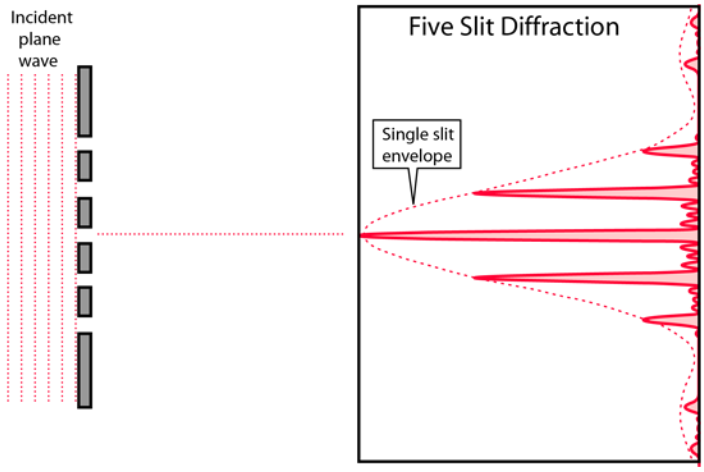

Figure 4.18 the interference pattern of a diffracting grating is made of the interference of the grating enveloped in the diffraction pattern of the slits.

As can be seen in the figure 4.18, the interference factor determines local minima while the diffraction factor is an envelope for the whole pattern.

The equation 4.40 reminds the SAXS intensity equation 4.27. The SAXS intensity is the product of the form factor and the structure factor whereas they are exchanged by the diffraction factor and the interference factor respectively in an optical transmission.

5 MATHEMATICAL MODEL

In this chapter a mathematical model is established to describe the SAXS scattering pattern by the nanoporous aluminum oxide. The aim is to investigate the parameters of the model and their relation to characteristics of the samples.

In the following the form factor of a cylinder is considered to represent a pore of the nanoporous sample. The cylinder is considered in two cases of single and core-shell cylinders. The polydispersity of the cylindrical pores and roughness of the pore walls are considered in the model. To explain the dispersion of cylindrical pores in the sample, two structure factors are discussed. the first one describes a well-ordered hexagonal arrangement and the second one is related to the same system with a level of disorder. After that the effect of the beam shape on the scattering pattern is considered.

In the next chapter the fitting of the model to experimental results is performed to deduce the properties of the samples. In the present chapter, calculations and simulations are done in terms of MATLAB platform using the numerical integration methods.

5.1 Elements of Modeling AAO

As described in chapter 2, the nanoporous alumina samples are made of aluminum oxide matrix containing cylindrical pores. Pores are basically arranged in a hexagonal order due to close packing principle. According to the discussion in chapter 4 when the sample is subjected to the X-ray transmission under SAXS setup, the cylindrical pores and their hexagonal arrangement are responsible for the form factor and the structure factor of the scattering pattern, respectively. However, there are sources of deviations from the explained ideal system. In the real samples the pores are not perfect cylinders. The most effective deviations from the perfection raise from the deformation of the pore surface shape from a circular shape. Another source of the deviation comes from the differences in the diameters of the pores. These two deviations are applied to the system as polydispersity. On the other hand, the

arrangement of the pores might deviate from the ideal hexagonal arrangement. This effect can be explained as thermal disturbance and in more disturbed cases a more random structure factor is considered. Therefore, statistical approaches are employed to explain the named disorders in the modeling.

5.2 Small Angle X-ray Scattering on a Cylindrical Object

In this section, we introduce the scattering from cylindrical object. As mentioned above, the dimensions of the pores in the nanoporous aluminum oxide samples are not identical and their shapes are disturbed from the ideal cylinder. The internal surfaces of the pore walls are rough. In the following sections, these deviations of ideal cylinder are considered by the development of the model.

5.2.1 The Form Factor of a Cylindrical Object

Illuminating a material with continuous and constant electron density doesn't give rise to any diffraction pattern. It only reduces the intensity of the beam compared to the direct beam due to the absorption. What gives rise to the scattering pattern is the differences in electron density at different positions of the real space. It can also be seen from equation 4.23 that if $\Delta\rho_e = 0$ then $I = 0$. The parameter $\Delta\rho_e$ is called the ***contrast***. According to the Babinet principle [31], since the squared contrast is contributing the scattering intensity, there is no difference between the diffraction pattern of an empty pore in a matrix with electron density ρ_0 and a cylinder with electron density ρ_0 in an environment with electron density 0. Therefore, for simplicity we choose to solve the second case.

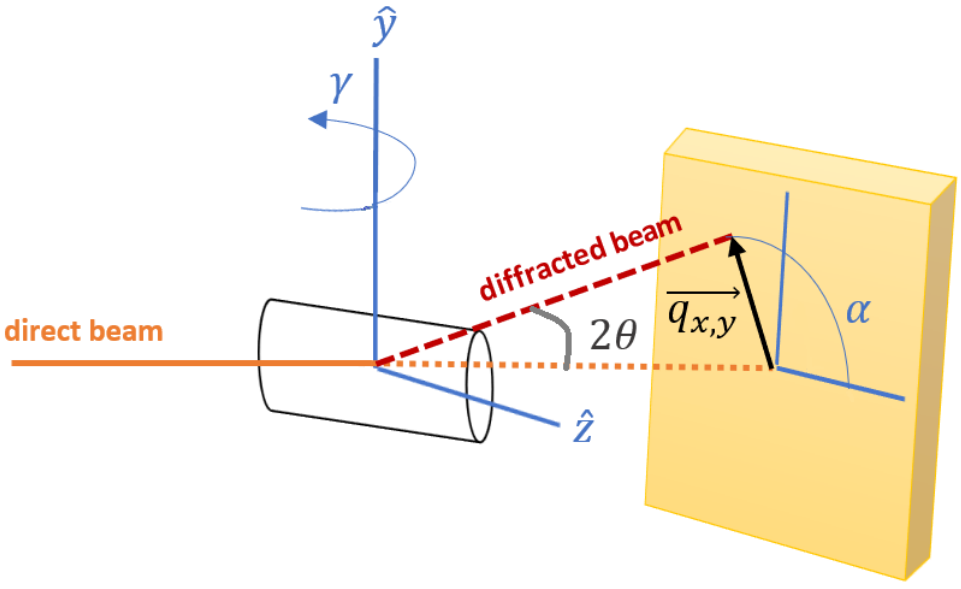

Figure 5.1 Schematic view of the SAXS scattering from a cylinder.

The geometry of the SAXS setup experiment measuring a cylindrical sample is shown in figure 5.1. The incident beam with wavevector $\vec{k}_0$ is scattered at position $\vec{r}$ and hits the detector as a scattered wave in the far field limit with wavevector $\vec{k}$. Due to the symmetry of the problem, the coordinate system is fixed with respect to the cylinder

and rotates with the cylinder through the angle γ. Angle α is the azimuth angle in the detector plane.

Following the discussion in chapter 4 section 4.3.1 the form factor of an ideal cylinder is derived (see also [30]). According to equation 4.22, the form factor of a cylindrical object with length L,radius R and electron density ρ_0 which is placed in a matrix with electron density 0 is given by the following expression:

$$F(\vec{q}) = \frac{1}{V_c}\int_{V_c} e^{-i\vec{q}\cdot\vec{r}}dV_c = \frac{1}{\pi R^2 L}\int_{-\frac{L}{2}}^{\frac{L}{2}}\int_0^R\int_0^{2\pi} e^{-i\vec{q}\cdot\vec{r}}\acute{\rho}d\phi d\acute{\rho}dz \qquad 5.1$$

Any deviation of the cylinder axis from the primary beam direction is shown by the tilting angle γ. This angle is considered to be in horizontal plane. The horizontal plane crosses the detector at azimuth angles $\alpha = 0°$ and $\alpha = 180°$. As described in [31] the scattering vector is parameterized as:

$$q_x = q(cos\,\alpha\,cos\,\gamma\,cos\,\theta + sin\,\gamma\,sin\,\theta) \qquad 5.2$$

$$q_y = -q\,sin\,\alpha\,cos\,\theta \qquad 5.3$$

$$q_z = q(cos\,\alpha\,sin\,\gamma\,cos\,\theta - cos\,\gamma\,sin\,\theta) \qquad 5.4$$

Since the SAXS is dealing with the small scattering angels of θ, it is usually considered that $\cos\theta \approx 1$ and $\sin\theta \approx \theta$. On the detector plane, the azimuth angle α is 0 where the projection of γ is maximum. Therefore equation 5.1 extends to the following:

$$F(\vec{q}) = \frac{1}{\pi R^2 L}\int_{-\frac{L}{2}}^{\frac{L}{2}} e^{-iq_z\cdot z}dz\int_0^R\int_0^{2\pi} e^{-i\left(q_x\cdot\acute{\rho}\,cos\,\phi + q_y\cdot\acute{\rho}\,sin\,\phi\right)}\acute{\rho}d\phi d\acute{\rho} \qquad 5.5$$

The z integration along the cylinder axis can be carried out and solved independently from the rest of the integrals.

$$\int_{-\frac{L}{2}}^{\frac{L}{2}} e^{-iq_z z}dz = \frac{2}{q_z}\cdot sin\left(q_z\cdot\frac{L}{2}\right)$$

$$= \frac{2}{q\,sin\,\gamma\,cos\,\alpha}\cdot sin\left(q\,sin\,\gamma\,cos\,\alpha\cdot\frac{L}{2}\right) \qquad 5.6$$

Beside some special cases, the rest of the equation 5.5 doesn't have an analytical solution and should be solved using numerical methods.

The first possible analytical solution is when the cylinder is not tilted at all. In this case $\gamma = 0°$ and the second part of equation 5.5 is given by:

$$\int_0^R \int_0^{2\pi} e^{-i(q_x \cdot \acute{\rho} \cos\phi + q_y \cdot \acute{\rho} \sin\phi)} \acute{\rho} d\phi d\acute{\rho}$$
$$= \int_0^R \acute{\rho} d\acute{\rho} \int_0^{2\pi} e^{-iq\acute{\rho}\cos\theta(\cos\alpha\cos\phi - \sin\alpha\sin\phi)} d\phi = \int_0^R \acute{\rho} d\acute{\rho}\left(2\pi J_0(q\acute{\rho})\right)$$
$$= 2\pi R \frac{J_1(qR)}{q} \qquad 5.7$$

J_0 and J_1 are the zeroth and first order Bessel functions of first kind. Since $\gamma = 0°$ the z-part of the integral tends to the constant value of the length of the cylinder, L, and the form factor turns out to be:

$$F_{\gamma=0}(\vec{q}) = \frac{1}{\pi R^2 L} 2\pi R L \frac{J_1(qR)}{q} = 2\frac{J_1(qR)}{qR} \qquad 5.8$$

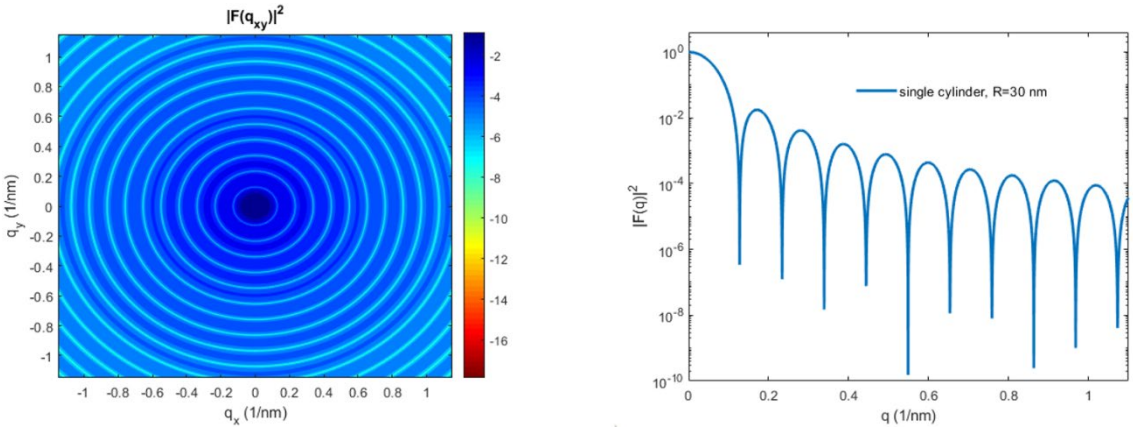

Figure 5.2 Left: two-dimensional, right: the line profile of the form factor of a single cylinder. The primary beam id parallel to the cylinder axis.

In this case the form factor is symmetric and forms concentric circular pattern.

Since there is no projection of the tilting angle γ on the vertical direction of the detector i.e. $\alpha = 90°$ or $\alpha = 270°$, equation 5.8 is always valid ion that direction at any tilting angle γ. In this direction of the detector equation 5.6 and equation 5.8 describe the total form factor of the cylinder.

The other case of an analytical solution is on the horizontal direction of the detector i.e., $\alpha = 0°$ and $\alpha = 180°$. It is possible to show [31] that in this case the form factor is given by:

$$F_{\alpha=0°/180°}(q) = \frac{2\sqrt{2}}{q \sin\gamma L} \frac{J_1(qR\cos\gamma)}{qR\cos\gamma} \qquad 5.9$$

Since we consider $\gamma = 0$ in our study, a detailed calculation of this case is beyond this scope. More details can be found in [109, 22, 28, 110].

5.2.2 Polydispersity

As mentioned in chapter 4 section 4.3.2, in a dilute system with same particles usually there is a distribution of the length scales which are contributing to the scattering prosses. This distribution is used to calculate the final form factor that appears in the scattering pattern. In the case of parallel cylinders with no specific order of arrangement, the scattering length scales with the radii of the cylinders. For averaging of the separated form factors the Schulz-Zimm distribution $g(R, \sigma_r, \langle R \rangle)$ is used for the radii of the cylinders

$$g(R, \sigma_r, \langle R \rangle) =$$

$$exp\left\{z_1\, log(z_1 \langle R \rangle) + z\, log(R) - log\big(\Gamma(z_1)\big) - \frac{z_1 R}{\langle R \rangle}\right\} \qquad 5.10$$

where $z = (\langle R \rangle / \sigma_r)^2 - 1$, $z_1 = z + 1$, Γ is the gamma function, and σ_r is a measure of the width of the distribution. This function corresponds to the Gaussian function with the advantage that it does not take negative values into account. This eliminates problems of negative values of radius in the fitting procedure especially for distribution with larger widths. The average form factor of a set of polydisperse cylinders is given by the following equation:

$$F(\vec{q}) = \int_0^\infty F(\vec{q}, r) g(r, \sigma_r, \langle R \rangle) dr \qquad 5.11$$

The effect of the polydispersity on the pattern is the smearing of the peaks. This effect is more enhanced for larger values of the scattering vector $\vec{q}$.

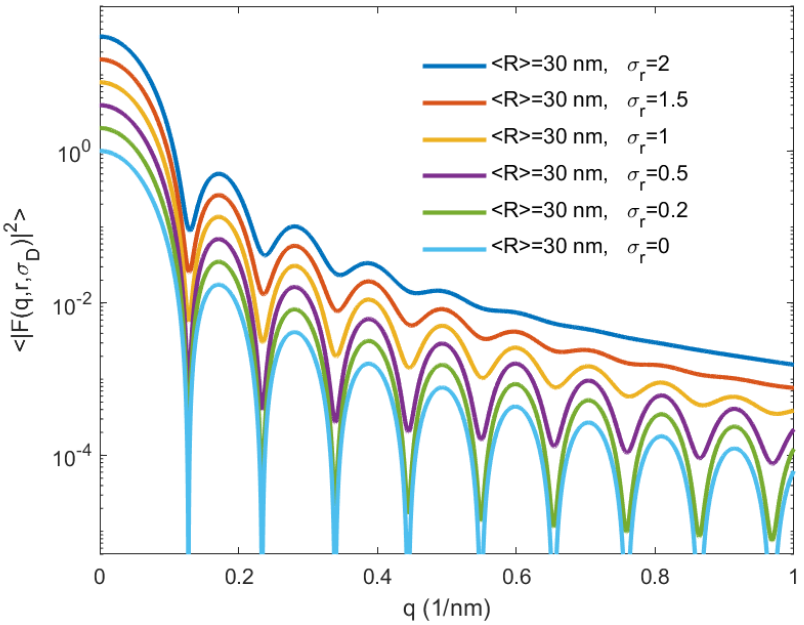

Figure 5.3 The polydispersity in the sample leads to smeared smeared peaks of the form factor.

5.2.3 Form Factor of a Core-Shell Cylinder

Here the form factor of a system is investigated which contains two coaxial cylinders, one placed into the other. This object consists of a cylindrical shell with constant electron density ρ_s around the core with constant electron density ρ_c, inner radius is noted by R_i and outer radius by R_o. The core-shell cylinder is located in an environment with constant electron density ρ_m. The corresponding form factor of the system can be derived as below:

$$\begin{aligned} F(q) &= -F_{R_o,\rho_m}(q) + F_{R_o,\rho_s}(q) - F_{R_i,\rho_s}(q) + F_{R_i,\rho_c}(q) \\ &= 2\left[-\rho_m \frac{J_1(R_o q)}{R_o q} + \rho_s \frac{J_1(R_o q)}{R_o q} - \rho_s \frac{J_1(R_i q)}{R_i q} + \rho_c \frac{J_1(R_i q)}{R_i q}\right] \\ &= 2\left[(\rho_s - \rho_m) \cdot \frac{J_1(R_o q)}{R_o q} + (\rho_c - \rho_s) \cdot \frac{J_1(R_i q)}{R_i q}\right] \end{aligned} \qquad 5.12$$

As it can be seen from the equation 5.12, the ordering of the electron densities is playing a role in the integrations of the calculation of the core-shell form factor. Therefore, in this case the Babinet principle is no longer valid. In this approach a continues matrix with electron density ρ_m is considered. A cylinder with radius R_o and length L is removed and replaced by a cylinder of the same shape and size but with different electron density ρ_s. The same procedure is done for the inner cylinder. With the explained assumptions, the form factor is calculated as equation 5.12. Another approach to calculate the core-shell cylindrical form factor can be found in [31] which gives the same result.

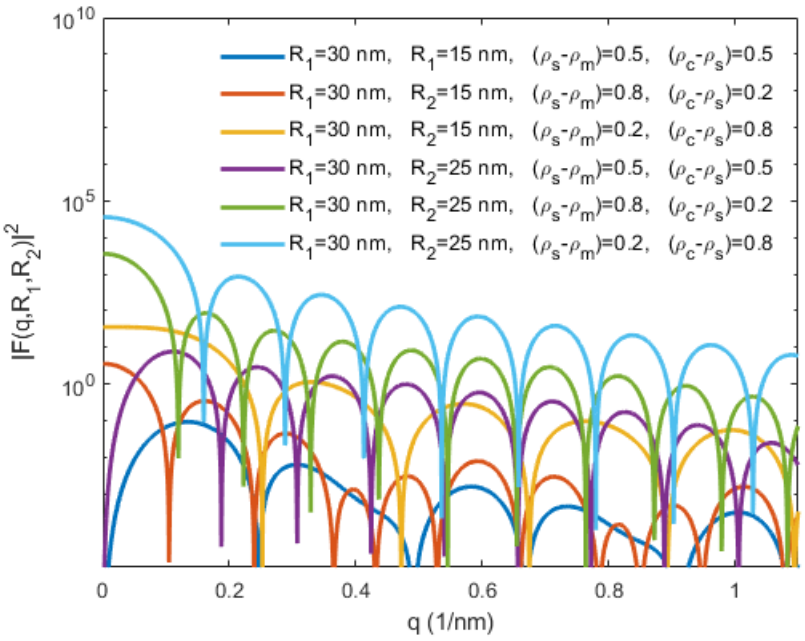

Figure 5.4 The form factor of a core-shell cylindrical object for different cases of contrast and radius difference.

5.2.4 Roughness of the Walls

So far, we have assumed that the transition from one material to the other ones is a sudden change of electron density on the edge of the cylinder walls. However, this is

not the case in reality. A more realistic assumption is that this transition takes place in a continuous manner. This fact is considered by considering a roughness on the walls. This factor comes to the equations by the convolution of the true electron density distribution with a Gaussian function which leads to an exponential decrease of the intensity. This effect is found in [31]. Using an attenuation factor with width σ_D of the Gaussian function, the intensity turns out to be as follow:

$$I(q) = I(q).e^{-(q\sigma)^2} \qquad 5.13$$

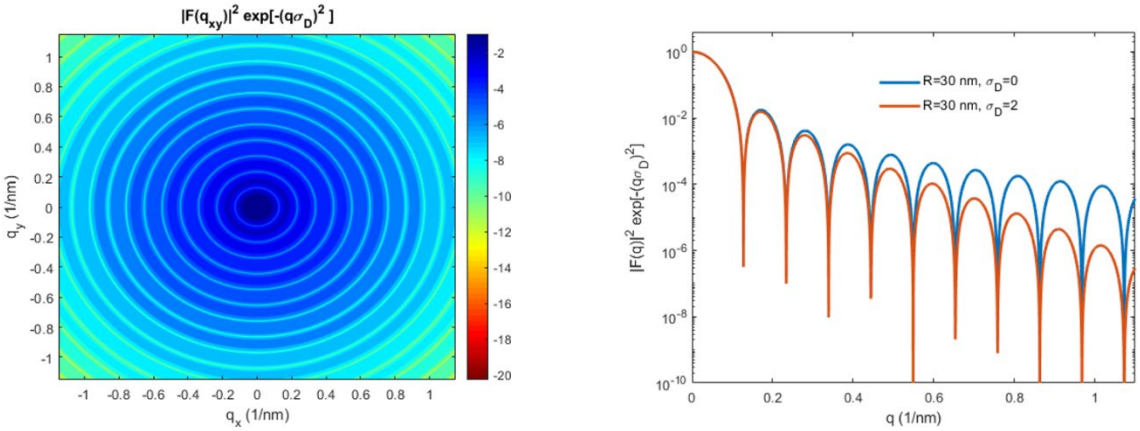

Figure 5.5 Left: two-dimensional, right: the line profile of the form factor of a single cylinder. The roughness of the walls causes to steeper drop of the intensity.

5.3 Structure Factor

In the following section, two models for the two-dimensional arrangement of the cylindrical pores are presented. One is a perfect nanocrystalline lattice and the other is a less well-ordered structure.

The first model explains the scattering intensity resulting from the arrangement of a two-dimensional hexagonal grid while the latter is developed to explain a less ordered arrangement. The goal is to obtain an expression for the structur factor $S(\vec{q})$ of the arrangement of cylindrical pores in nanoporous aluminum oxide which is describes in section 5.1 [111].

5.3.1 Structure Factor of a Two-Dimensional Hexagonal Grid

The two-dimensional lattice is already well-known in crystallography. Using equations 4.4 – 4.6 it is straight forward to realize that the reciprocal space of such a lattice is also a 2D hexagonal lattice with $30°$ rotation. In a hexagonal lattice the length of the two lattice vectors are the same. The value of the vectors are $|\vec{a}_1| = |\vec{a}_2| = a$ in real space and $|\vec{a}_1^*| = |\vec{a}_2^*| = \frac{4\pi}{\sqrt{3}a}$ in reciprocal space.

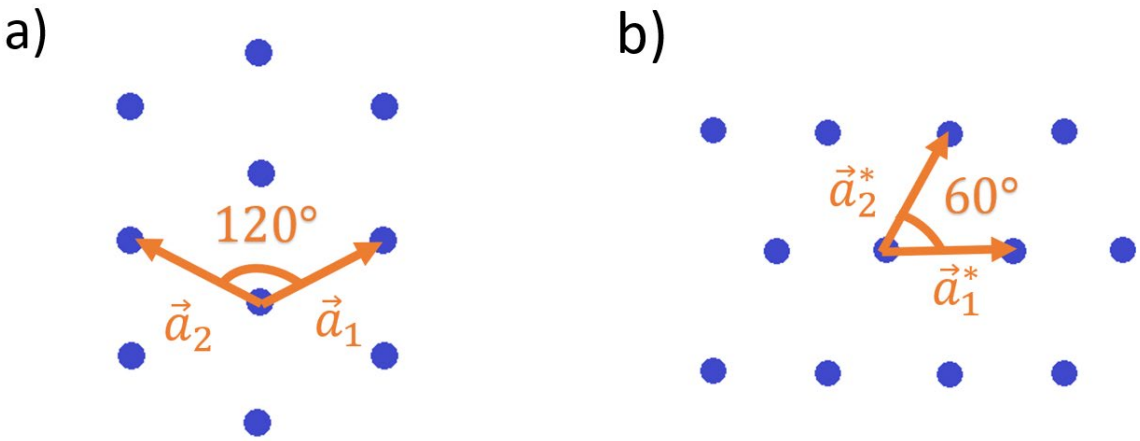

Figure 5.6 The view of a hexagonal lattice in a) real space and b) reciprocal space.

The characteristic length a is the interpore distance between 2 pores. It is the first neighbor distance in real lattice. The positions of the Bragg reflexes $\vec{q}_i$, which result from the lattice distances are modeled with Gaussian functions of constant width σ_B . In crystallography the Debye-Waller factor $\sigma_{DW}/2$ shows the thermal vibration of the lattice points around their rest position. In our case we use it as a measure of the disorder in the sense of a small deviation of the position of the pores around the lattice position well known as static Debye Waller factor. The nanoporous AAO samples consist of several domain regions of hexagonal lattices which are randomly arranged. Because of this two-dimensional powder averaging of the pore arrangement, there is an additional inverse q dependency $1/q$. This results in the structural factor in the form of following equation:

$$S(\vec{q}) = \frac{1}{A} e^{-q^2 \cdot \sigma_{DW}^2/2} \sum_{hk0} \frac{const}{\sqrt{2\pi}\sigma_B} \frac{1}{q} exp\left(-\frac{(\vec{q}_{hk0}^* - q)^2}{2\sigma_B^2}\right) \qquad 5.14$$

with the surface of the unit cell $A = \frac{\tilde{a}^2\sqrt{3}}{2}$ and the average lattice constant $\tilde{a}$ [28].

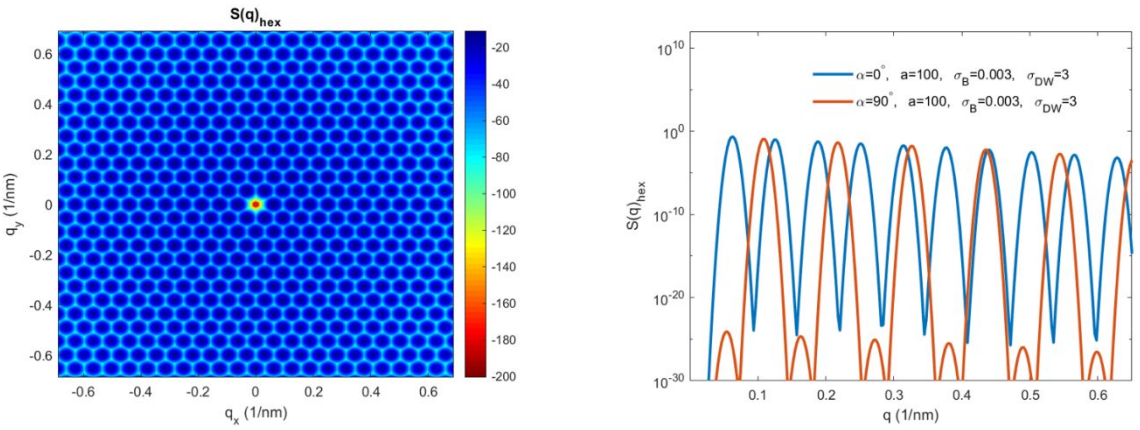

Figure 5.7 Left: two-dimensional, right: the line profile of the hexagonal structure factor. The position of the peaks is dependent to the line profile direction.

5.3.2 Scattering From a Mixture of Two-Dimensional Hard Disks

The structure factor for a two-dimensional hexagonal lattice can only be used within a limited range of the Debye-Waller factor [30]. When the correlation of the pores to one another is rather random, the perfect lattice is no longer the right model. In this case the structure can be modeled with a two-dimensional model of a fluid-like correlation of hard disks. The structure factor for a mixture of two-dimensional hard disks is presented in [112]. In [31] this model has been proposed as a possible description for the arrangement of less well-ordered cylindrical pores [113]:

$$1/S(q) - 1 = 4\kappa\left\{A\left[\frac{J_1(qR_{hc})}{qR_{hc}}\right]^2 + B\cdot J_0(qR_{hc})\cdot\frac{J_1(qR_{hc})}{qR_{hc}} + G\cdot\frac{J_1(2qR_{hc})}{qR_{hc}}\right\} \qquad 5.15$$

with

$$A = \frac{[1 + (2\kappa - 1)\chi + 2\kappa G]}{\kappa} \qquad 5.16$$

$$B = \frac{[(1-\kappa)\chi - 1 - 3\kappa G]}{\kappa} \qquad 5.17$$

$$Z = \frac{1}{(1-\kappa)^2} \qquad 5.18$$

$$\chi = \frac{(1+\kappa)}{(1-\kappa)^3} \qquad 5.19$$

$$G = \frac{1}{(1-\kappa)} \qquad 5.20$$

κ is a measure of the order of the system. For high values of κ the peaks are very sharp that they tend to infinity. Since a certain disorder in the system is assumed, structure factors for values $\kappa \gtrsim 0.76$ are unrealistic. For large values of κ the function diverges in the area of the first maximum. The second parameter R_{hc} corresponds to half average distance between adjacent pores. Which is correlated to the average half-distance of the pores.

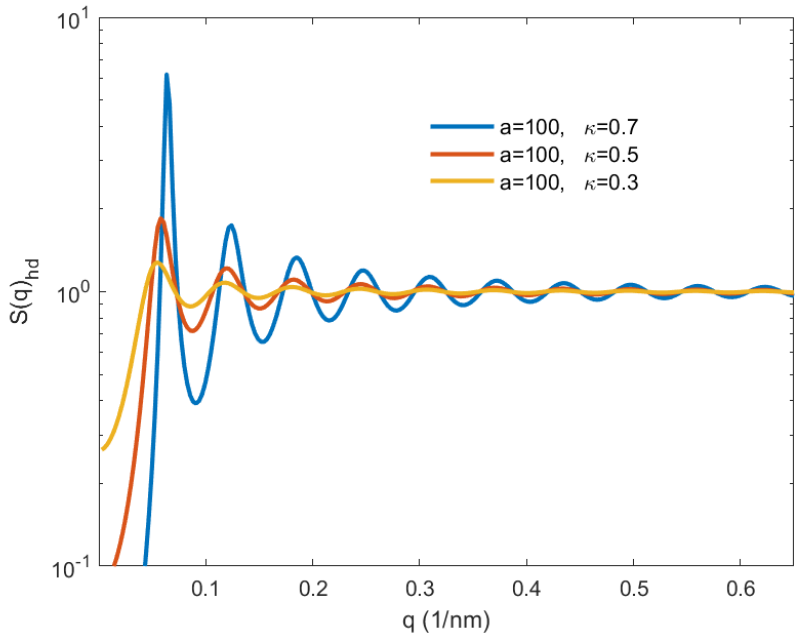

Figure 5.8 Structure factor of random arrangements of the objects. Lower value of κ indicates a more random arrangement.

5.4 Beam Shape Effects on the Scattering Pattern

The shape of the beam is another parameter to be considered for the simulation of the scattering pattern in an accurate way. Most X-rays beams have Gaussian shape. The shape of the incident beam is convoluted with a Gaussian function to the presented model for the intensity. The Gaussian width σ_q is a measure of the q-resolution of the equipment in $[1/\mathrm{nm}]$. For the scattering Intensity with a constant Background intensity I_{BG} we can write the final expression for the intensity as follow:

$$I(q) \propto I(q) \otimes \frac{1}{\sqrt{2\pi}\sigma_q} exp\left\{-\frac{(\tilde{q}-q)^2}{2\sigma_q^2}\right\} + I_{BG} \qquad 5.21$$

6 EXPERIMENTAL RESULTS

In this chapter the results of measurements on nanoporous aluminum are presented in cases of empty pores and pores filled by polymer. To check the wetting procedure and electron density of the polymer, the X-ray reflectivity experiments have been done for one type of polymer. Then the results of typical SAXS experiments are presented with focus on structural resolution in relation to the experimental setup. A model is introduced which was established in order to predict the presence of polymer inside the pores. Finally, the agreement of a more detailed model explained in chapter 4 to the data is discussed.

6.1 X-ray Reflectivity (XRR) on the Polymer

The X-ray reflectivity (XRR) is a measurement technique which is sensitive to the properties of sample surface [114]. It is also used to investigate thin films on substrate with smooth surface. This technique is based on the interference of X-rays from the surface and inner interfaces causing formation of Bragg peaks on particular angles of reflection. We have used this method to test the wetting of flat, plane and smooth silicon substrate by thermoresponsive polymer. In this way, we also can measure the layer thickness and the electron density of the polymer layer.

6.1.1 Theoretical Basis of XRR

When an X-ray beam illuminates a surface of a material, it can exhibit two major processes, namely reflection and refraction. In the first process a part of the beam reflects from the surface. In the second one the rest of the beam penetrates into the medium and if not absorbed, it propagates in the medium with a change in its direction of propagation.

Considering the medium of interest to be homogeneous and the boundaries to be sharp, the two phenomena are related to a parameter called the refractive index n described as follow [115]:

$$n = 1 - \delta + i\beta \qquad (6.1)$$

As it is well-known, δ and β are functions of the beam energy and the properties of the medium as follow [116, 117]:

$$\delta = \frac{\lambda^2}{2\pi} r_e \rho_e = \frac{\lambda^2}{2\pi} r_e \left(Z \frac{N_A \rho_m}{A} \right) \qquad (6.2.a)$$

$$\beta = \frac{\lambda}{4\pi} \mu \qquad (6.2.b)$$

With λ the wavelength of the X-ray, r_e the classical electron radius, ρ_e the electron density, ρ_m the mass density, Z atomic electron number, A the atomic weight, N_A Avogadro's number and μ the absorption coefficient of the medium. δ is usually of the order of 10^{-5} in solids and around 10^{-8} in air. This parameter is related to the scattering properties of the medium. While the imaginary part β is related to the absorption properties of the medium and is much smaller than δ [24].

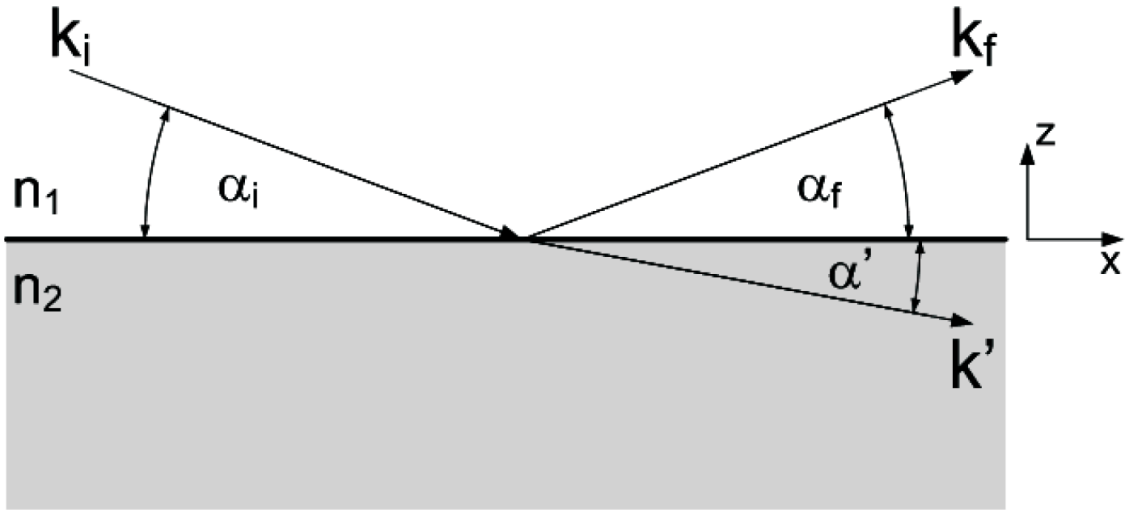

Figure 6.1 Schematic view of reflection and refraction of the X-ray by α_f and α' respectively where $\alpha_i = \alpha_f$ and $\alpha_i > \alpha'$ for X-rays. k_f and k' are the wavevectors of the reflected and refracted beam [118].

As mentioned before the value of δ depends on the energy of the X-rays and it falls to smaller values for higher energy. It is obvious that for X-rays, the real part of the n is less than unity. However, this difference is very small. This is due to the fact that the X-ray frequency is generally higher than the resonance energies related to the binding of the electrons in atoms [24].

The angle of refraction is derived from the Snell's law as follow:

$$n_1 \cos \alpha_1 = n_2 \cos \alpha_2 \qquad (6.3)$$

Where n_1 and n_2 are the refractive indices of first and second media respectively, α_1 is the incident angle and α_2 is the refracted angle. When X-rays enter from a less dense medium to a denser one $n_1 > n_2$ they refract towards the surface boundary. As a consequence, below a certain angle of incidence angle called ***critical angle*** α_c total external reflection of the X-rays occurs where $\alpha_2 = 0$. If the X-rays are initiated from the vacuum or air, then $n_1 = 1$ and α_c can be found using eq. 6.7:

$$\cos \alpha_c = n_2$$

If the absorption index β is ignored in comparison with δ and is considered as:

$$n_2 = 1 - \delta$$

with the Taylor expansion of the cosine function we have:

$$\cos \alpha_c = 1 - \frac{{\alpha_c}^2}{2} + \cdots$$

And therefore, the critical angle is related to δ as follow:

$$\alpha_c = \sqrt{2\delta} = \lambda \sqrt{\frac{r_e \rho_e}{\pi}} \qquad (6.4)$$

Equation 6.4 shows that the critical angle is a characteristic parameter of the material which is connected to its electron density. Therefore finding α_c leads to get the important parameter of the material ρ_e.

6.1.2 XRR Experiment on a Thin Film Layer

The XRR experiment is the proper technique to find the critical angle and thus the electron density of a thin film layer. For this purpose, a thin film layer of a polymer is placed on a proper substrate such as silicon and is examined under following procedure.

Consider a thin layer of material (region 1) lying on a flat and smooth substrate (region 2) with larger electron density (fig 6.2). The X-rays illuminate the sample from the air (region 0). The surface of 0 and 1 is illuminated first at $\alpha = 0$. Since the incident angle α_i is smaller than the critical angle α_{c1} the total reflection occurs, and no part of the beam enters the thin film layer.

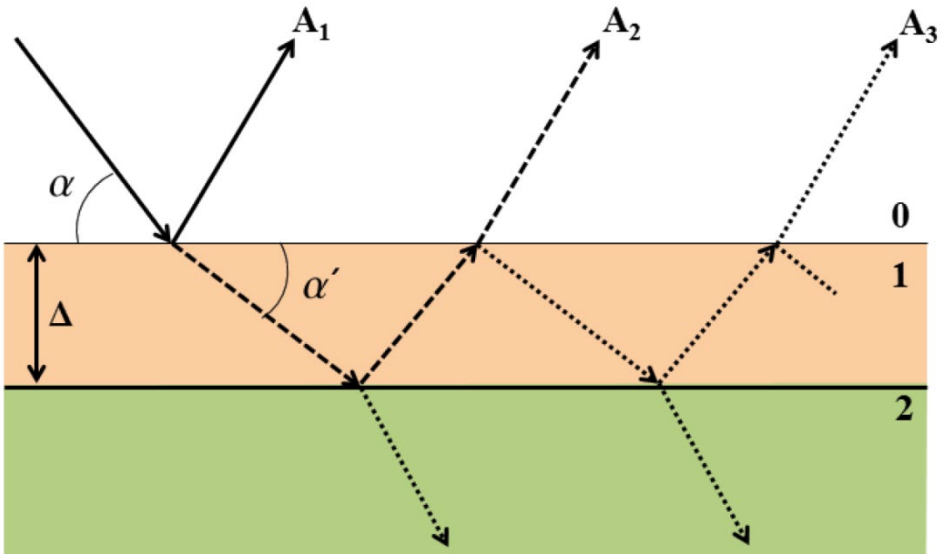

Figure 6.2 reflection and refraction of the X-ray from the two surfaces. The beam reflects and refracts several times within the thin film layer [118].

Then the incident angle increases and exceeds the critical angle of the thin film. At this point a part of the beam enters the thin film and is refracted by entering the new medium. Then it reflects at the interface of thin film and the substrate. Since the

electron density of the substrate is larger than the film, the total reflection of the beam happens at surface 1 and 2 at first. This is the case up to the point that the refracted beam within the thin film hits the surface at an angle larger than the critical angle of the substrate α_{c2}. Between the 2 surfaces, the beam reflects several times. A detector is placed on an angle equal to the incident angle and records the summation of the rays on that angle.

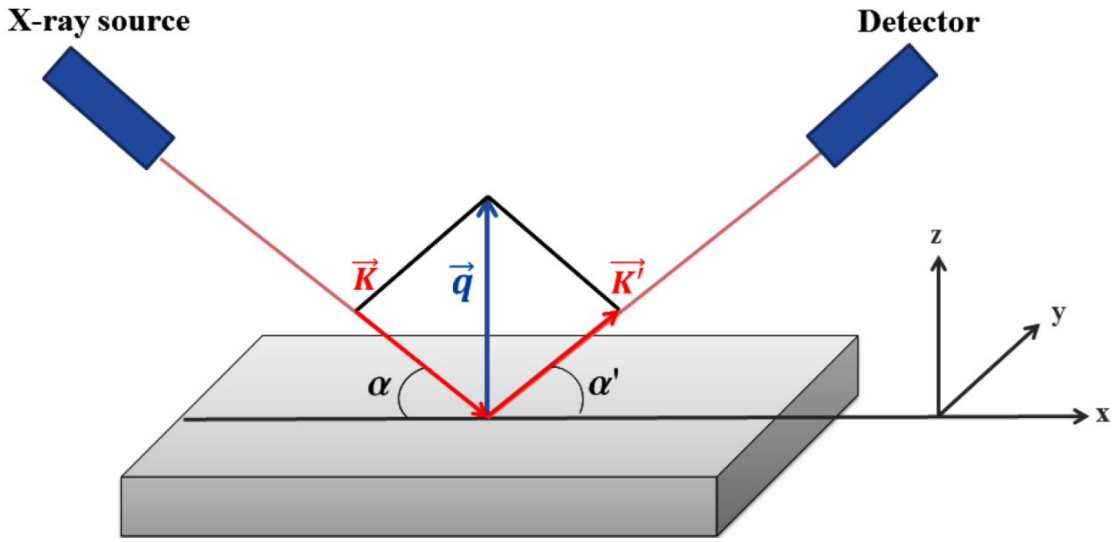

Figure 6.3 Schematic view of XRR experiment. The detector is recording the scattering on an angle equal to the incident angle. The scattering is a function of $2\alpha_i$ denoted by 2θ [118].

The scattering angle is the angle between the projection of direction of the incident beam and the reflected beam which is $\alpha_i + \alpha_f = 2\alpha_i$ and is noted by 2θ. The resulted pattern contains Bragg peaks which are called ***Kiessig fringes***. The period of Kiessig fringes is $2\pi/\lambda$ in 2α in q-space. According to Bragg peaks' law, the fringes are related to the layer thickness of the thin film layer as follow [119]:

$$\Delta = \frac{\lambda}{2(\alpha_{m+1} - \alpha_m)} \qquad m \in \mathbb{N} \qquad (6.5)$$

Where α_ms are the angular position of the fringes.

The angular position for which the maximum intensity falls to its half, $\alpha_{\frac{I_{max}}{2}}$ indicates the critical angle of the substrate α_{c2}:

$$\alpha_{\frac{I_{max}}{2}} = 2\alpha_{c2} \qquad (6.6)$$

And the critical angle of the thin film α_{c1} can be found as [120]:

$$\alpha_m^2 = m^2 \frac{\lambda^2}{4\Delta^2} + \alpha_{c1}^2 \qquad m \in \mathbb{N} \qquad (6.7)$$

6.1.3 Experiment

The experiments were performed at the in-house X-ray laboratory at Emmy Noether Campus (ENC), University of Siegen. The wavelength was $\lambda = 1.54$ Å and the result

was recorded by a scintillation counter/photomultiplier with a monochromator-crystal on a STOE theta/theta diffractometer. In order to have reliable results, an accurate alignment of the setup is necessary.

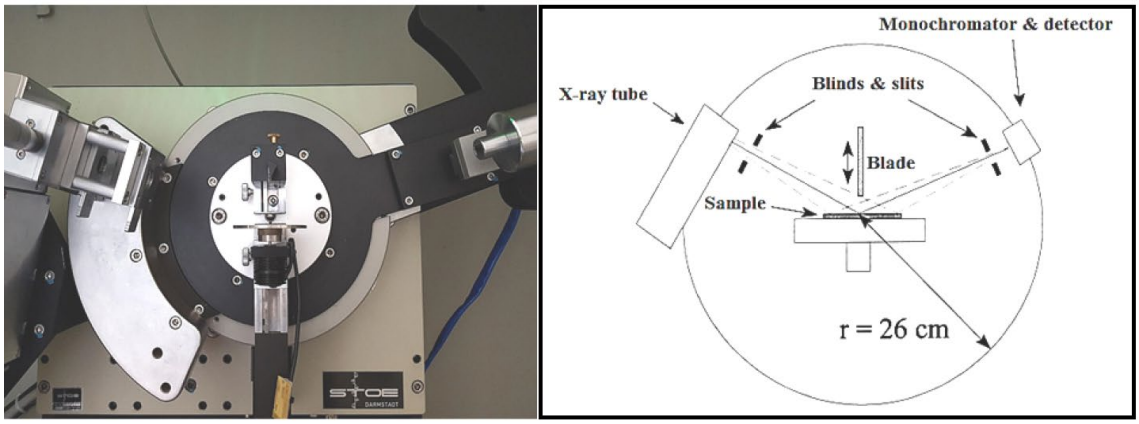

Figure 6.4 STOE theta/theta diffractometer at University of Siegen [118].

The sample should be placed on a horizontal plane. Another important point is that detector records the reflection meaning that the incident angle of the tube with respect to the horizontal plane should be the same as the angle of the detector with the same plane. As it is shown in fig 6.4., the sample is located in the center in horizontal position. The detector and the X-ray tube rotate simultaneously on a circle centered by the sample holder.

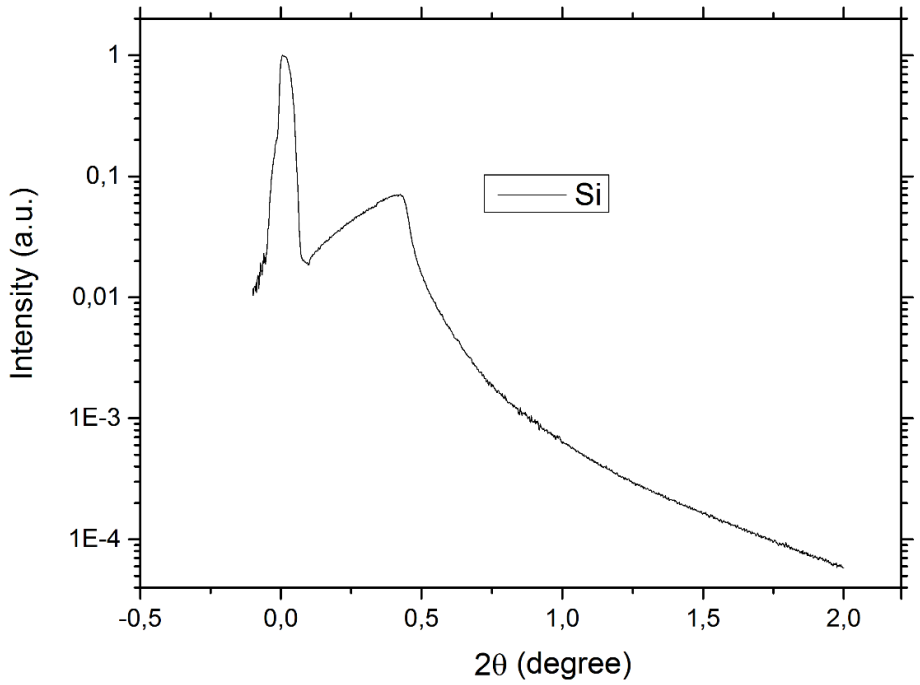

Figure 6.5 XRR experiment result on bare silicon

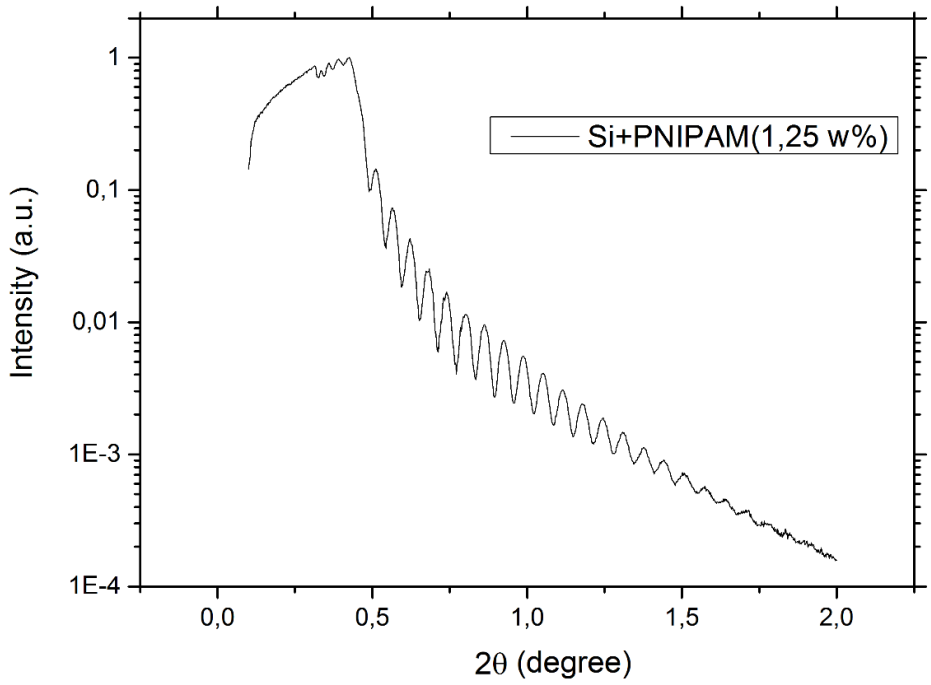

Figure 6.6 XRR experiment result on 1.25 w% of MU-F007 polymer thin film on silicon substrate

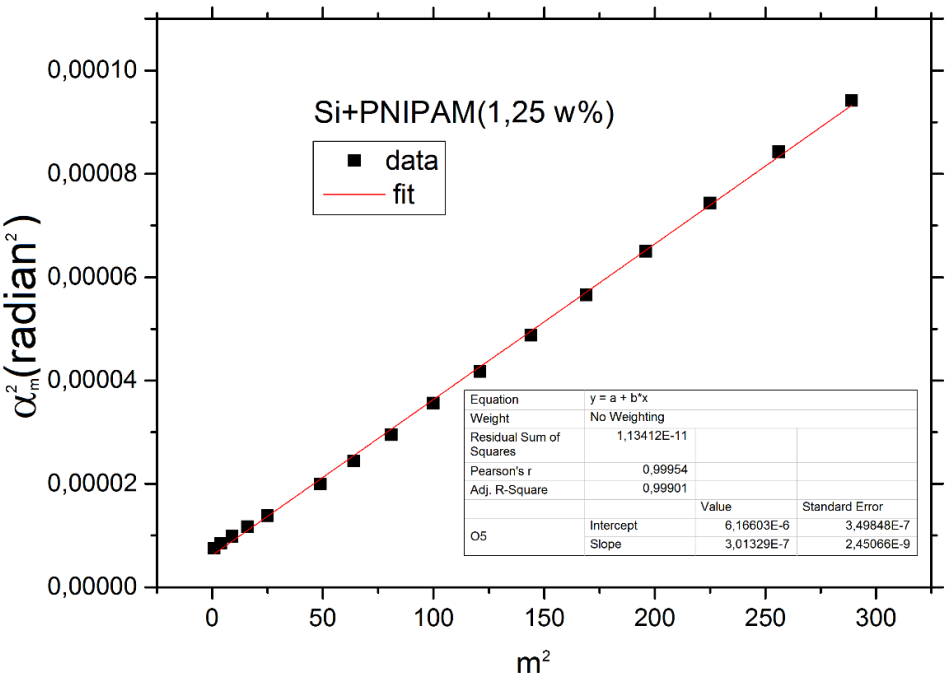

Figure 6.7 Linear fit of Kiessig fringes for 1.25 w% of MU-F007 polymer

At any given time, the X-ray tube and the detector make the same angle with respect to the horizontal plane. Therefore, the detector records the reflection of the beam from the sample. The scattering angle is noted by 2θ. At small angles of incident, such as $\alpha_i < \alpha_c$ the intensity is so high that it can saturate the detector and discredit the measurement at that range of angles. To avoid this problem the measurement begins with an absorber made of a metallic foil of proper thickness. At larger angles the absorber is removed. Instead the exposure time is increased in order to reach better statistics. It can be proven that for $\alpha > 3\alpha_c$ ($q > 3q_c$) the reflection goes down as α^{-4} (q^{-4}) [118, 121, 122].

To check the wetting properties and the electron density, the polymer was examined under XRR experiment. A thin film layer of the MU-F007 polymer was deposited on silicon substrate via spin coating method [93]. A bare silicon wafer as well as two samples with thin film polymers of solutions with different concentrations of 1.25 w% and 2.5 w% were examined.

Figure 6.5 shows the XRR result on bare silicon. The absence of Kiessig fringes confirms that there is no thin film on the silicon surface. The position of the half maximum intensity corresponds to $\alpha_{c2} = 0.23^\circ$ which is in good agreement with literature [118].

Figure 6.6 shows the XRR result for thin film of MU-F007 polymer prepared with a solution of 1.25 w% polymer in ethanol on silicon substrate. Using the equation 6.5, the thickness of the polymer layer can be found. The periodicity of Kiessig fringes lead to 144 nm for the layer thickness. According to equation 6.7, a linear fit is applied to the value of α_m^2s with relation to their orders m^2s which is shown in figure 6.7 The slope of the fit is related to the thickness of layer which confirms the obtained value 144 nm. The intercept relates to the critical angle of the polymer and therefore its electron density. The value of the intercept for the obtained fit gives the critical angle of the polymer as $\alpha_{c1} = 0.142^\circ$.

Another experimental result is shown in figure 6.8 with its fit in figure 6.9 the polymer has a concentration of 2.5 w%. the layer thickness was found as 140 nm and the critical angle of the polymer agrees well with the previous experimental result $\alpha_{c1} = 0.142^\circ$.

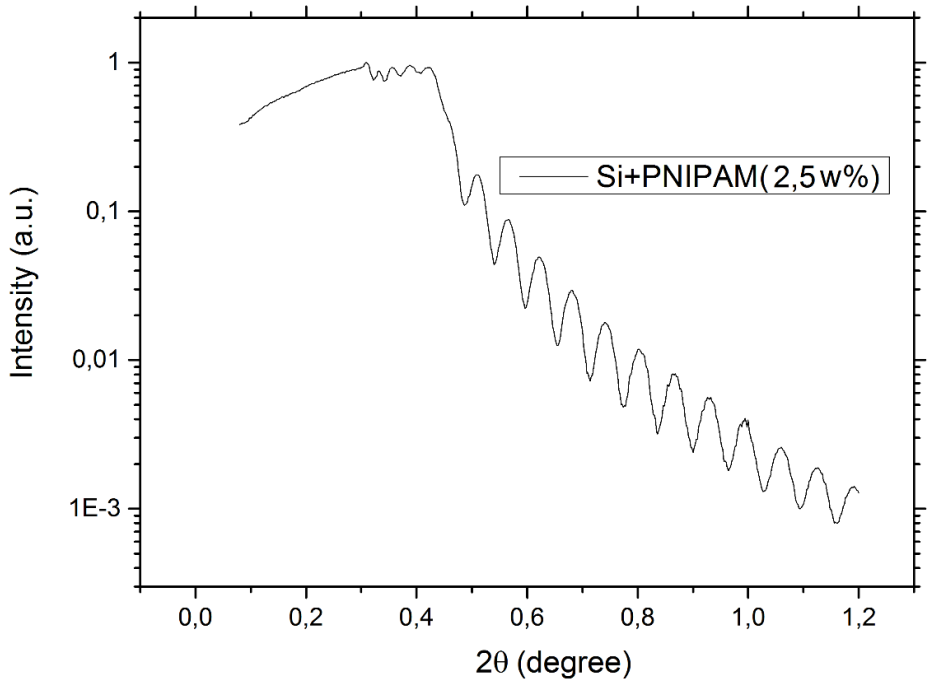

Figure 6.8 XRR experiment result on 2.5 w% of MU-F007 polymer thin film on silicon substrate

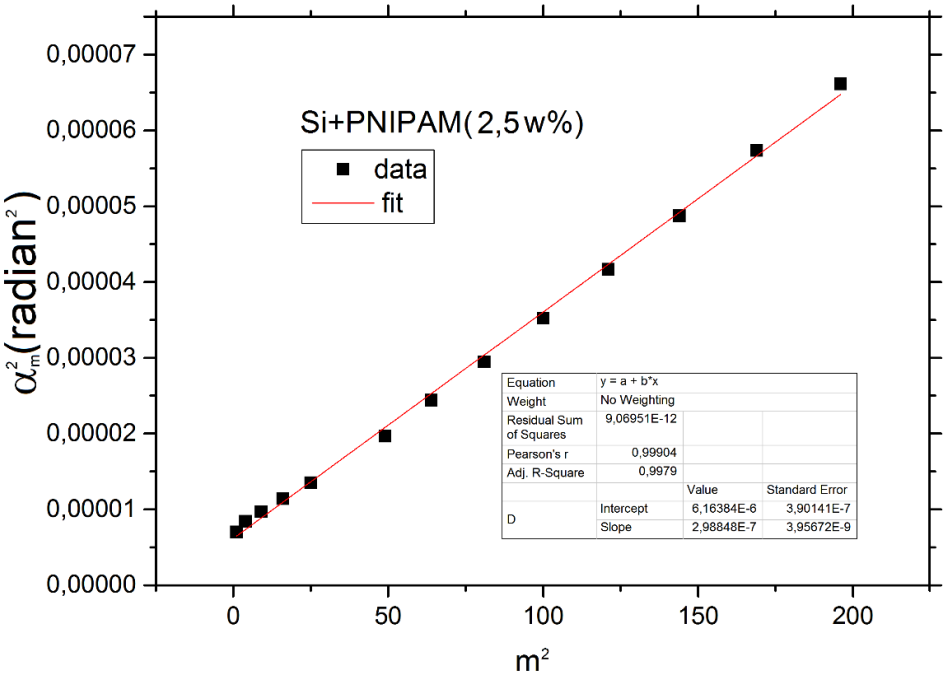

Figure 6.9 Linear fit of Kiessig fringes for 2.5 w% of MU-F007 polymer

6.2 Results of the SAXS Measurement

AAO samples have been examined with SAXS measurement under the setup explained in chapter 5. A typical result of the experiment is shown in figure 6.10. For the analysis usually, the horizontal line profile of the image is considered.

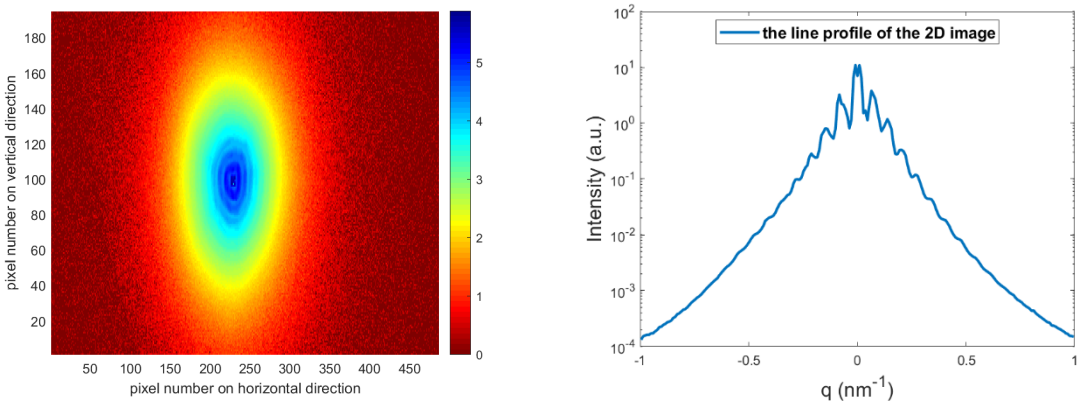

Figure 6.10 On the left is an example of 2D image of SAXS experiment on 40 V AAO empty samples and its line profile is shown on the right.

When X-ray beam is scattered from the sample, the scattering pattern on the detector is recorded on the pixels of the 2D Pilatus detector. The number of events on each pixel represents the intensity at that position. However, this value should be normalized to the direct beam intensity which falls by time.

6.2.1 Experimental Resolution

After the determination of the position of the direct beam on the detector, the positions of other pixels relate to the scattering angle by 2θ. Considering the size of each pixel to be 172 microns and the distance of the sample to the detector L, the transferred momentum q can be derived as follow:

$$2\theta = \tan^{-1}\frac{n \cdot 172}{L} \qquad (6.8.a)$$

$$q = \frac{4\pi \sin\theta}{\lambda} \qquad (6.8.b)$$

Where λ is wavelength of the incoming beam and n is the number of the pixel with regards to the pixel at the elastic interaction where the transferred energy is zero. As it can be seen from 6.11, for higher values of L a specific pixel falls on a smaller value of θ which in turn leads to higher resolution of the results. To quantify the resolution of data more specifically we introduce the parameter Res as the number of data points i.e. number of pixels which in a unit of scattering vector q.

$$Res = \frac{total\ number\ of\ data\ points}{q_{max} - q_{min}} \qquad (6.9)$$

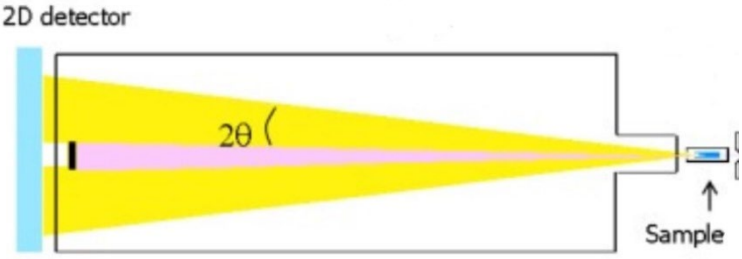

Figure 6.11 As the detector to sample distance gets larger, there are a greater number of pixels recording the pattern in 2θ range. Therefore, the measurement is recorded at a better resolution [123].

Since in small angles $\sin\theta \approx \theta$ and $\tan\theta \approx \theta$, Res can be estimated as follow:

$$q = \frac{4\pi \sin\theta}{\lambda} = \frac{4\pi}{\lambda}\frac{n \cdot 172 \cdot 10^{-6}}{2L}$$

$$Res = \frac{n_{max} - n_{min}}{q_{max} - q_{min}} = \frac{2L\lambda}{4\pi \cdot 172 \cdot 10^{-6}} \qquad (6.10)$$

Equation 6.10 shows that the data resolution depends on the experimental setup namely: the energy of the beam, the sample to detector distance and the pixel size of the detector which in our case is 172 microns.

As explained before in chapters 2 and 5 the scattered intensity of SAXS measurement is related to the Fourier Transform of the electron density distribution. In other words, it reveals the spatial correlation of scatterers in the sample. An increase in the value of distance L leads to the increase of the range of observation on q which in turn decreases the size range in real space by $2\pi/q$.

Another benefit of collecting the scattering intensity at small values of scattering vector q is that it enables us to study systems with characteristic sizes up to few microns. However, there are some important parameters such as data resolution which might block the details of the scattering from larger substructures in the experiment. For example, if we are interested to observe scattering form structures of size of a micron, each pixel of detector should cover scattering vector smaller than $q = 2\pi/1\ micron^{-1}$.

$$Res = \frac{1}{2\pi/1\ micron} = \frac{2L\lambda}{4\pi \cdot 172\ micron} \Rightarrow \frac{4\pi \cdot 172\ micron}{4\pi/1\ micron} = L\lambda \qquad (6.11)$$

For a beam with energy 13 keV the corresponding wavelength is $\lambda = 0.95 \cdot 10^{-10}\ m$, the sample to detector distance should be at least $1.81\ m$. If the value of Res is smaller than $1\ micron/2\pi$ then the details of scattering pattern are accumulated in one pixel and the structural information of the scattering pattern are merged and therefore concealed by ***binning effect*** of the detector.

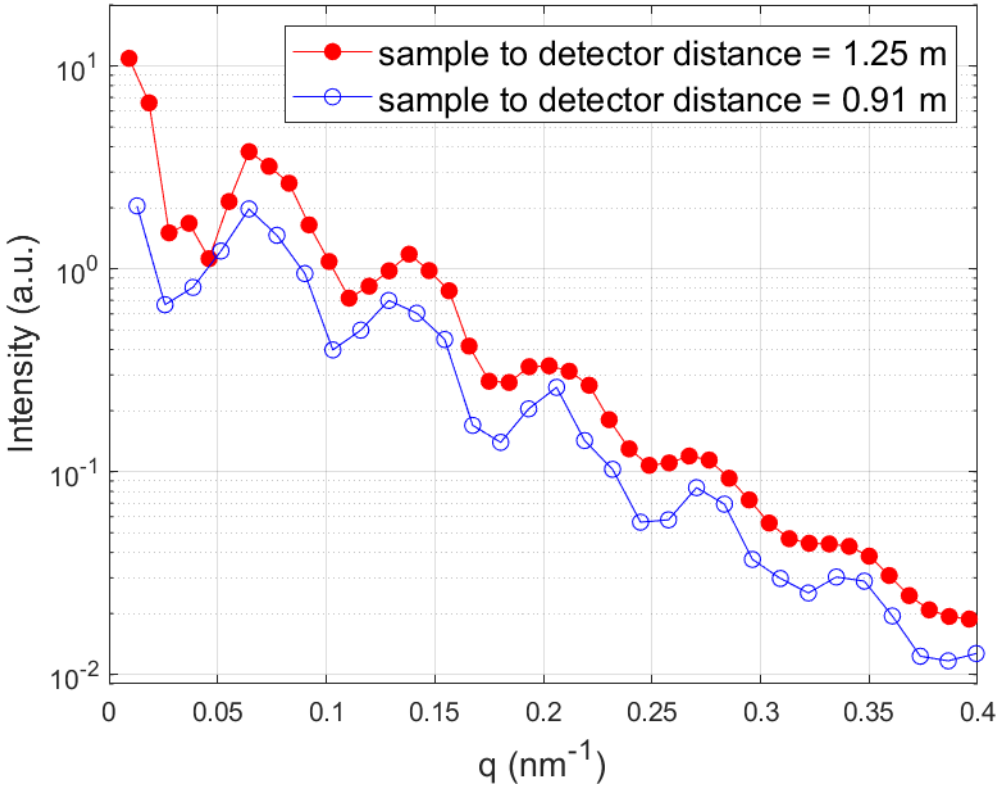

Figure 6.12 Comparison of the measurements for a 40 V empty sample at 2 different distances of sample to detector.

Figure 6.12 shows two measurements of the same sample. The sample is a bare 40 V anodized sample. As explained in chapter 3 it has an interpore distance around 100 nm and pore diameter around 60 nm. The sample was examined at 13 keV energy of the X-ray. The sample was placed once at 0.95 m and the other time at 1.25 m away from the detector. The red curvature with filled markers shows the measurement at larger distance. There are 11 data points for qs smaller and equal to 0.1 nm^{-1} for the red curve whereas this value is 8 for the blue curve. From equation 6.10 we can find the resolution:

$$Res_{1.25} = \frac{2L\lambda}{4\pi \cdot pixel\ size} = \frac{2 \cdot 1.25 \cdot 0.95 \cdot 10^{-10}}{4\pi \cdot 172 \cdot 10^{-6}} = 110 \cdot 10^{-9}$$

$$Res_{0.91} = \frac{2L\lambda}{4\pi \cdot pixel\ size} = \frac{2 \cdot 0.91 \cdot 0.95 \cdot 10^{-10}}{4\pi \cdot 172 \cdot 10^{-6}} = 80 \cdot 10^{-9}$$

Which means there are 110 and 80 data points for a unit of q nm^{-1} for larger and smaller distance, respectively.

As it can be seen from the figure, there is a peak at q=0.036 nm^{-1} in the red curve which is not visible in the blue curve. This is an example of missing data due to low resolution and binning effect of the detector.

6.2.2 Error Bar of the Data

One problem which usually occurs at larger values of q in the scattered intensity is the descended ratio of signal to background which dominates the pattern. To overcome this problem the so-called ***dummy scan*** is used. In this method one measurement is done many times e.g., 100 times and the result of all these measurements are added to form one final pattern. This way we increase the statistics of photons and reduce the ratio of noise to signal. The uncertainties of data points are measured by error propagation regarding the errors of the pixels in each image.

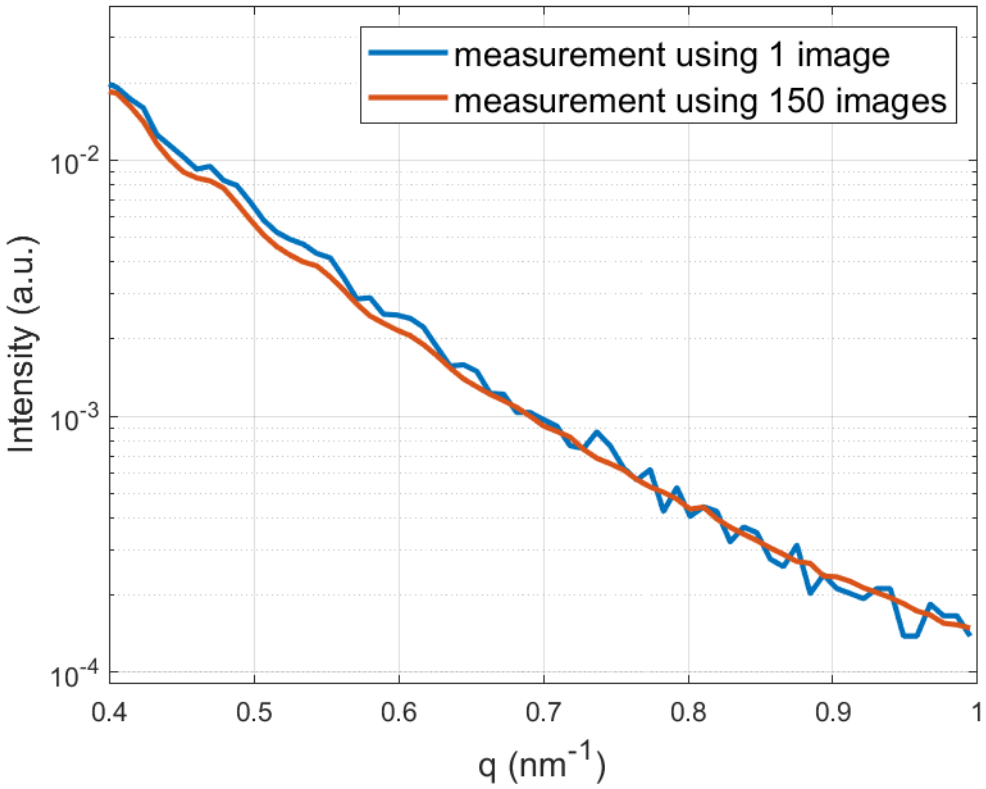

Figure 6.13 Blue curve is the line profile using one detector image. Red curve is the summation of same measurement using 150 images

As it can be seen in figure 6.13, using only one image can be misleading to some artificial oscillation which are only caused by the high level of the noise. For further analysis specially in the fitting process, it is very important to find the right error bars of the data points.

The uncertainties of the counts on each pixel of the single image is given by $1/\sqrt{N_j}$ where N_j is the number of the counts on j^{th} pixel. When the image is normalized to the intensity of the direct beam I_{norm} this value turns out to $1/\left(I_{norm} \cdot \sqrt{N_j}\right)$. The error bar of j^{th} pixel of the final image is calculated by the error propagation formula for j^{th} pixel of the total number of images t. It is given by the following:

$$f_j(x_{1j}, \dots, x_{ij}, \dots, x_{tj}) = \frac{1}{t}\sum_{i=1}^{t} x_{ij} = \frac{1}{t}\sum_{i=1}^{t} \frac{N_{ij}}{I_{norm,i}}$$

$$\delta f_j(x_{1j}, \dots, x_{ij}, \dots, x_{tj}) = \frac{1}{t}\sqrt{\sum_{i=1}^{t}\left(\frac{\partial f}{\partial x_{ij}}\delta x_{ij}\right)^2}$$

$$= \frac{1}{t}\sqrt{\sum_{i=1}^{t}\left(\frac{1}{I_{norm,i}\cdot\sqrt{N_{ij}}}\right)^2} \qquad (6.12)$$

Where i is summing up on the images.

6.3 Primary Model

As a first step through the investigation of pore filling in AAO samples, a model has been established to predict the SAXS intensity based on a study done by Eidmann et al [25] and later by Ruggles et al [26]. In this model the basic idea is that the SAXS intensity is enveloped by a function related to the form factor. It is proved that the intensities at central maximum I_0 and m[th] maxima I_m are related to the pore radius r and interpore distance d as follow:

$$I_0 = \left(\frac{r}{d}\right)^2 + \left(1-\frac{r}{d}\right)^2 c_1^2 + 2\frac{r}{d}\left(1-\frac{r}{d}\right)c_1c_2 \qquad (6.13.a)$$

$$I_m = \left(\frac{\sin\left(m\pi\frac{r}{d}\right)}{m\pi}\right)^2 (1 + c_1^2 - 2c_1c_2) \qquad (6.13.b)$$

Where $c_1$and c_2 are constants of material which in our case is aluminum oxide.

Based on that we can consider the empty AAO sample as a grating with pinholes with pore diameter r_0. Then the filled AAO samples are estimated as grating similar to the case of empty samples but with an effective pore diameter r_{eff} smaller than r_0. Therefore, the model helps to evaluate the effective pore diameter of filled sample compared to the empty one.

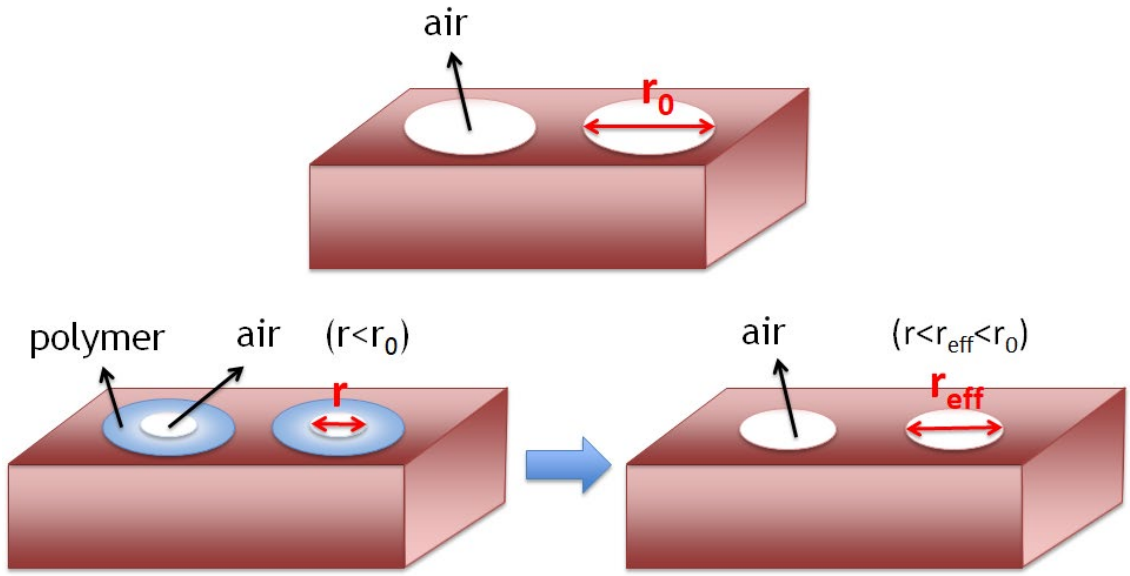

Figure 6.14 Illustration of primary model. On top is the empty sample with its original diameter r_0. Bottom shows the filled sample considered as an empty one with effective pore diameter r_{eff}.

Figure 6.15. left shows the recorded two-dimensional pattern of the scattering recorded by the Pilatus detector. As mentioned before, the central line profile containing the central maximum intensity is driven as in figure 6.15. right. This way the experimental values of the $I_0$and I_m are available from the measurements.

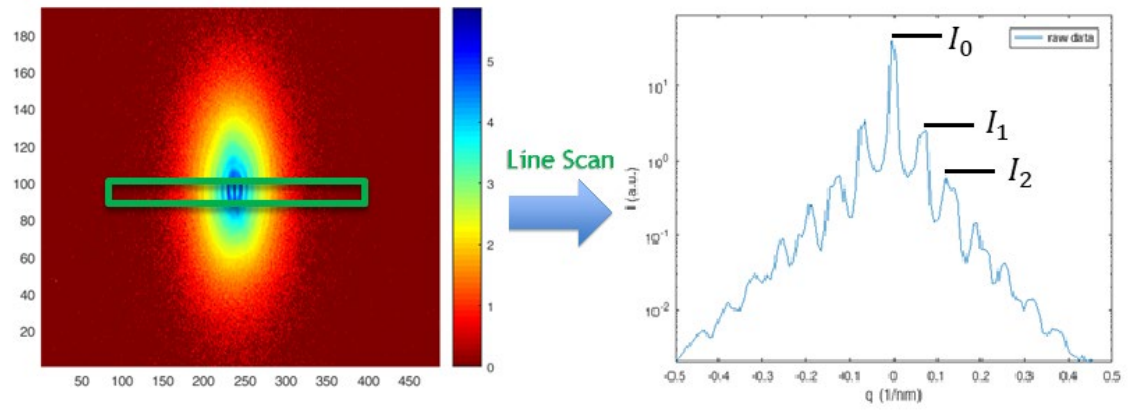

Figure 6.15 Left: the 2D recorded scattering pattern of the SAXS experiment. Right: obtained line profile taken from the horizontal line in the middle.

Using the values of I_1 and I_2 taken from the line profile, the ratio of $\frac{r}{d}$ can be found regardless of the values of c_1 and c_2. The corresponding value for empty sample is calculated as follow:

$$\left(\frac{I_1}{I_2}\right)_{empty} = \frac{4\sin^2\left(\pi\frac{r_0}{d}\right)}{\sin^2\left(2\pi\frac{r_0}{d}\right)} = A_0 \qquad (6.14)$$

And for the filled sample it turns out to:

$$\left(\frac{I_1}{I_2}\right)_{filled} = \frac{4\sin^2\left(\pi\frac{r_{eff}}{d}\right)}{\sin^2\left(2\pi\frac{r_{eff}}{d}\right)} = A_f \qquad (6.15)$$

The value of A for empty sample at room temperature $A_{0,rt}$ differs from that of the same sample filled by water and measured at higher temperature $A_{0,T}$. The same logic which is used to evaluate equation 6.15 is applicable to calculate the effective pore diameter for the measurements at higher temperatures for empty and filled samples namely $A_{0,T}$ and $A_{f,T}$ respectively. Substantially the values of effective pore diameters are different at different temperatures. They are noted as $r_{0,T}$ for empty and $r_{eff,T}$ for filled samples.

The ratio of $\frac{r_{eff,T}}{d}$ for different samples is extracted from the experiments. 40 V samples were examined as bare, 0.1 w% of MU-F007, 1 w% of MEM-063 and 3 w% of MU-F007 and 25 V samples as bare and 3 w% of MU-F007 at 13 keV energy of X-rays. Also, both sample sizes were examined bare, 0.1 w% of MU-F007 and 1 w% of MU-F007 at 10 keV energy of the X-ray. The results are summarized in figures 6.16 – 6.19.

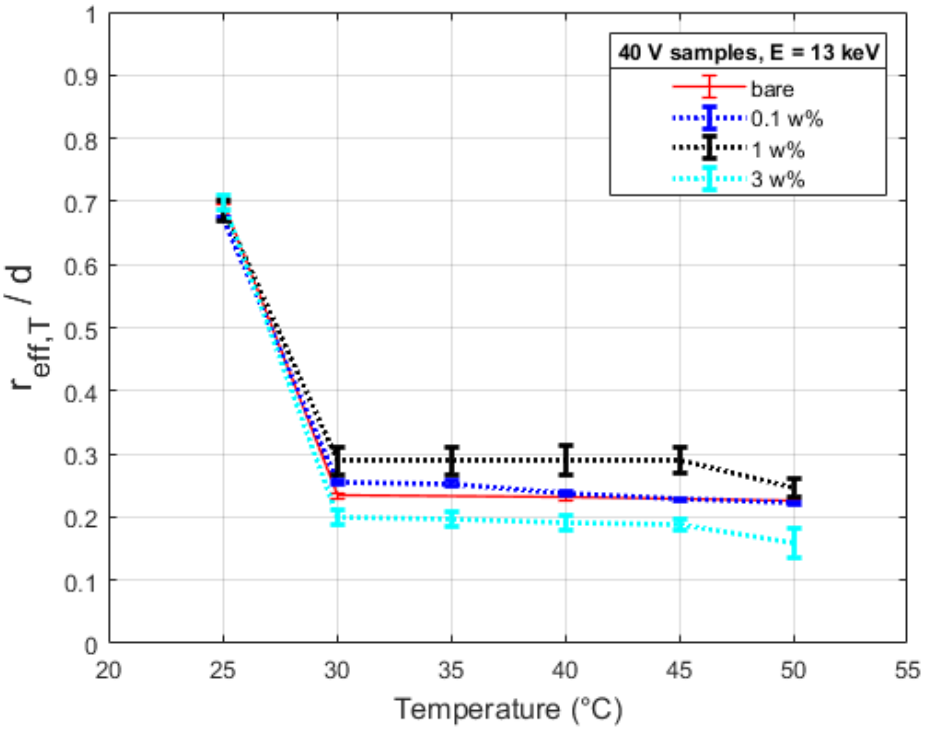

Figure 6.16 Ratio of $\frac{r_{eff,T}}{d}$ for 40 V samples at 13 keV of X-ray energy. The experiments were done at 4 different temperatures.

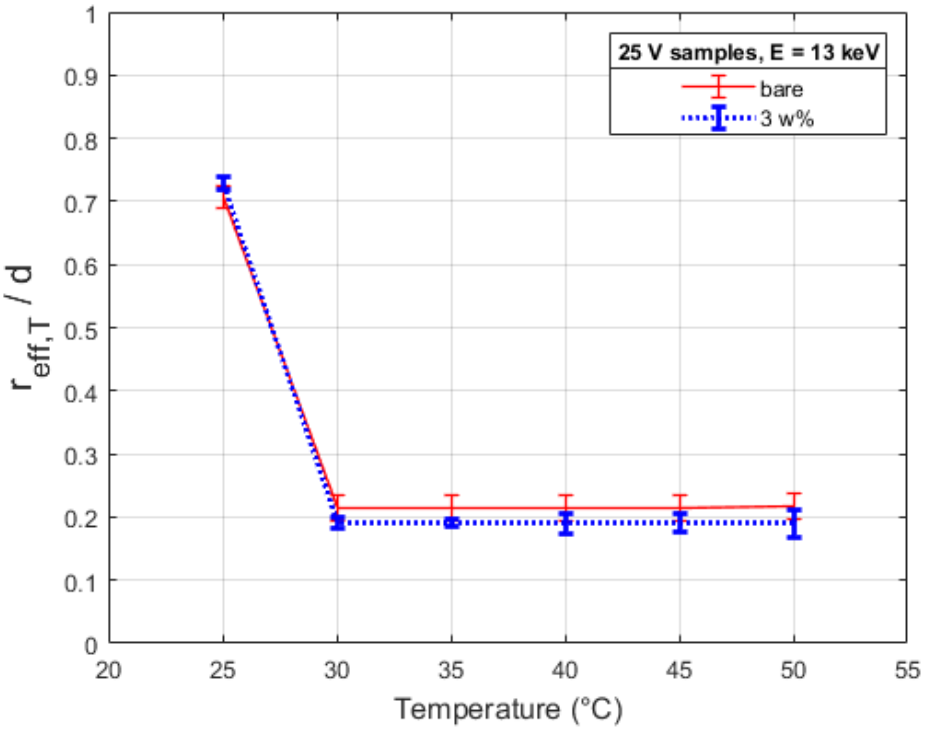

Figure 6.17 Ratio of $\frac{r_{eff,T}}{d}$ for 25 V samples at 13 keV of X-ray energy. The experiments were done at 6 different temperatures.

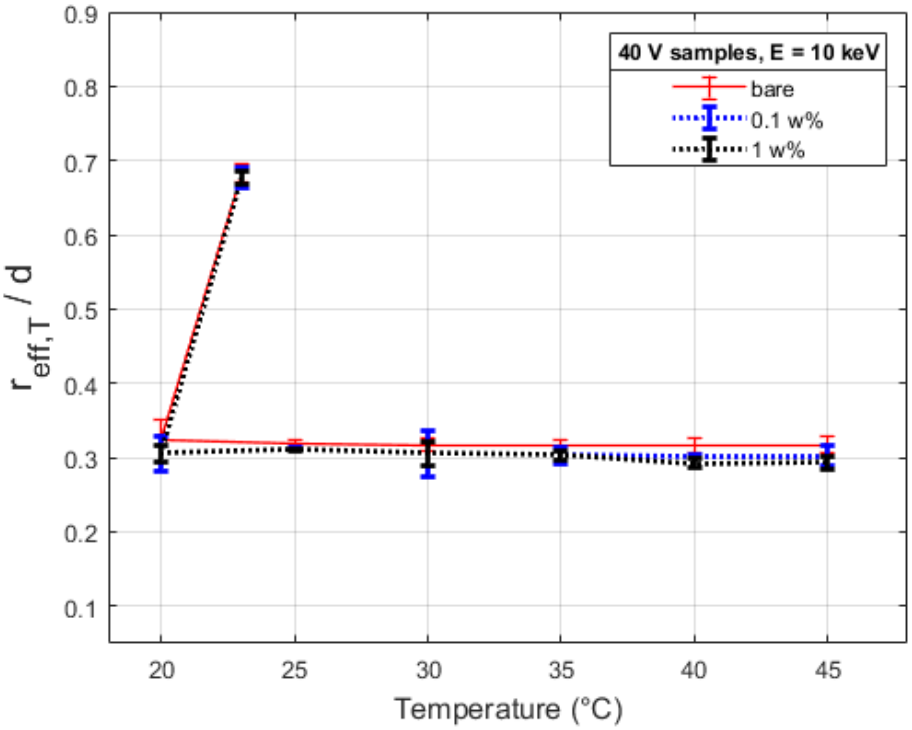

Figure 6.18 Ratio of $\frac{r_{eff,T}}{d}$ for 40 V samples at 10 keV of X-ray energy. The experiments were done at 7 different temperatures.

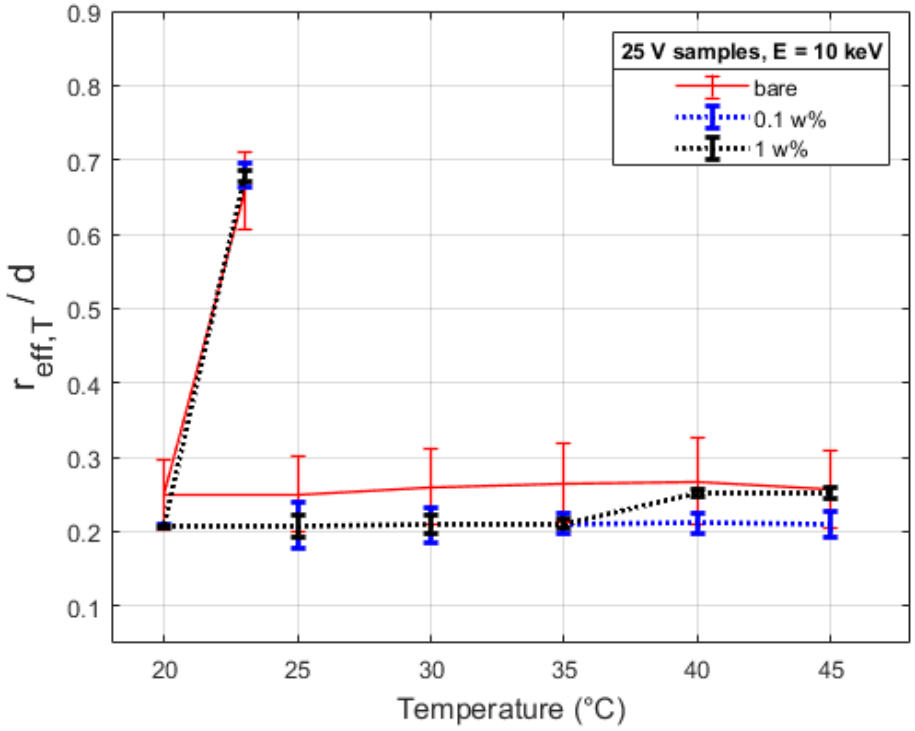

Figure 6.19 Ratio of $\frac{r_{eff,T}}{d}$ for 25 V samples at 10 keV of X-ray energy. The experiments were done at 7 different temperatures.

40 V samples at 13 keV show changes for different temperatures. The drop of the value for higher temperatures shows the decrease of the ratio for them. The value remains the same for the bare sample at different temperatures. While this value shows a slight decrease at higher temperatures for 0.1 w%, 1 w% and 3 w% samples. This could be a sign of swelling of the polymer inside the pores. Regarding the error bars for other experiments, significant changes in the values are not visible for 40 V samples at 10 keV and for 25 V samples at 13 and 10 keV energy of the X-ray.

6.4 Characterization of Nanoporous AAO

In order to tease out the properties of the constructed nanopores, we use a retrieval procedure by employing Markov Chain Monte Carlo (MCMC). We used a Python implementation of *emcee* [124, 125], called MCKM [126], to effectively sample the parameter-space.

MCKM handles any arbitrary number of model parameters over regular (Cartesian) or irregularly spaced steps and any arbitrary number of data points and their respective covariance matrices. The observational uncertainties can be estimated through a Gaussian process using a variety of kernels.

The MCMC methods are a class of algorithms for sampling from probability distributions. These methods generate samples from a random variable, with probability density proportional to a known function. In practice, an ensemble of chains is generated based on an arbitrary set of points that are called stochastic walker processes. The walkers move around randomly and explore the parameter-space to find chains with higher probabilities. Such processes would allow maximizing

likelihood and estimate the posterior distributions of free parameters. To set up the algorithm, we need to specify the number of parameters, the number of walkers and initialize the walkers with the starting values of the parameters.

The probability distribution of model parameters, i.e. the posteriors, is traditionally visualized through “corner plots”, where the probability distribution function of each parameter and their correlations with other parameters can be shown.

To setup the retrieval, we assume uninformative priors to initialize 2000 walkers in the MCMC process and iterated until the solution converged. The mathematical models explained in Chapter 4 are employed as our forward models. The free parameters are chosen in accordance with the aim of retrieval at each characterization step and will be discussed later.

The reported uncertainties are the marginalized uncertainties of each free parameter at the 16%, 50%, and 84% quantiles, as is common for the representation of marginalized posteriors in MCMC results. The best fitted models are also shown along with the data in the corresponding figures. In order to visualize the uncertainties, we randomly draw 300 model-parameters from the converged posteriors and calculate the 16%, 50%, and 84% quantiles at any given q. The 50% quantile is shown by a dark green line and the shaded light green area represents the area between 16% and 84% quantiles. The goodness of the fit is assessed based on the Bayesian information criterion.

6.4.1 Fitting to a Single Sample

As the first step, we aim fitting the model to the empty samples. To this end, we select only one measurement to assess if sufficient information is contained in the data in order to constrain the model-parameters meaningfully.

Given the high number of received photons to the detector, the formal measured uncertainties are photon-noise limited and follow a Poisson distribution. This estimation of uncertainties, however, results in extremely low relative uncertainties at low q values, which makes the fitted parameters highly sensitive to, for example, sample heterogeneities and possible experiment’s setup errors. The data of a single sample and associated uncertainties are shown in Figure 6.20.

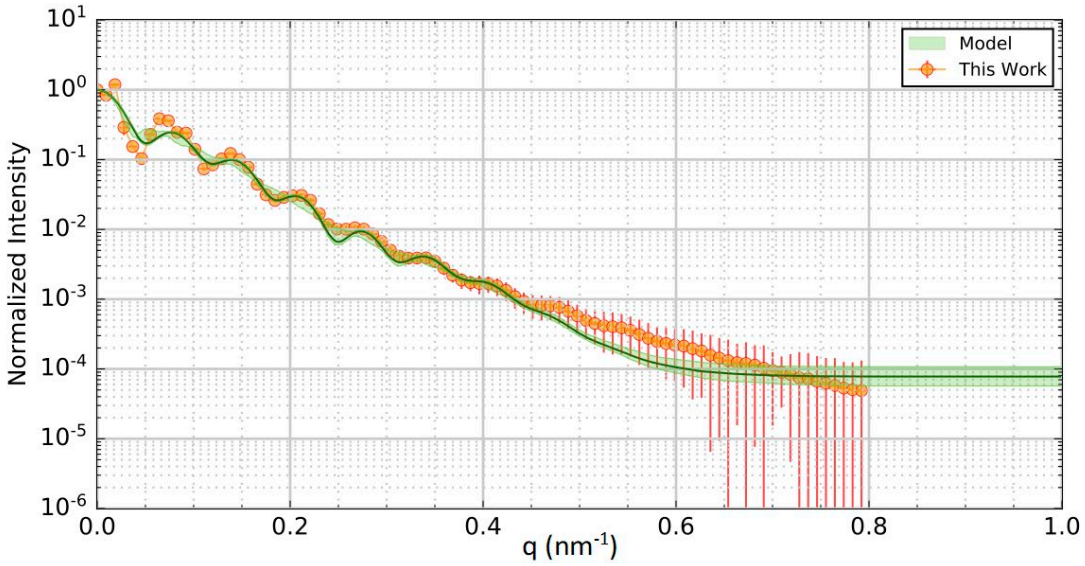

Figure 6.20 Fitting of the complete model to a bare AAO sample. The data (orange symbols) and their associated photon-noise limited uncertainties along with the calculated best fitted model at 50% quantile, and the corresponding 16%-84% quantiles. The 50% quantiles are shown with red lines and 16% and 84% quantiles with dashed

We begin with the core-shell cylindrical form factor with polydispersity (equation 5.12 as it is suggested in the literature [31, 32]. For the structure factor of two-step anodized samples, scattering from a mixture of two-dimensional hard sphere is used (equation 5.15). Therefore, free parameters were chosen to be the average radius of the inner cylinder, $\langle R_i \rangle$, the width of the $\langle R_i \rangle$ distribution noted by $g(R, \sigma_r, \langle R \rangle)$, σ_r, the average radius of the outer cylinder, $\langle R_o \rangle$, the electron density difference between the shell and the core of cylinders, $\rho_c - \rho_s$, the $\frac{\rho_s - \rho_m}{\rho_s - \rho_m}$ ratio, where is electron density difference between the matrix and the shell cylinders, intensity scaling factor, A, measure of the perturbation, κ, separation of two adjacent peaks in the structure factor, R_{hc}, structure factor's scaling factor, C_S, background intensity, I_{bc}, and roughness of the cylinders walls, σ_D.

Here we ignore qs with values larger than 0.8 nm^{-1} due to their large uncertainties and also, we limit our investigation to the positive qs, i.e. 0<q<0.8 nm^{-1}. Figure 6.20 shows the result of our fit to a single measurement.

Comparing the fitted model with the data, both through posteriors and visual inspection, suggest a statistically reasonable fit. However, the obtained parameters in Figure 6.20 appear to be unphysical. The result is consistent with a high-density core with a radius of around 7nm and a low-density shell with a radius of 48nm. This is not consistent with the bare sample which is expected to have much smaller core density with larger radius [8, 34].

Having a closer look at line profile, we realize that it begins with sharp narrow peaks. In larger values of q these peaks are replaced by more widened peaks. As it was discussed in section 4.3.3, the effect of particles interaction in the system is visible in smaller values of q. This effect smears out at larger values. Accordingly, the line profile can be

sorted in two regions. The first region where particles interaction affects the intensity and the structure factor is visible. The second region where the structure factor tends to one and the pattern is dominated by the form factor. In above case, the fit result show poor match at small values of qs and therefore week consistency with the suggested structure factor.

The unphysical results might have been caused by the low resolution at small *q*s and their very small uncertainties. Such combination enforces a biased fit toward the limited sampled *q*s and hence causes the domination of fitted model by poorly constrained form factor parameters. Consequently, some measures must be taken to resolve the issue.

The following three measures were taken for the next step: 1) limiting the retrieval to 0.25<q<0.9 nm^{-1}, 2) assigning arbitrary uncertainties to avoid underestimation of uncertainties at low *q*s, and 3) limiting the free parameters to $\langle R_i \rangle$, σ_r, the difference between the average radius of the outer and inner cylinders, R_{diff}, electron density of the shell (ρ_s) and the core cylinder (ρ_c), intensity scaling factor, A, background intensity, I_{bc}, and roughness of the cylinders walls, σ_D. These aim us to only focus on the form factor fitting and exclude the unwanted structure factor affects.

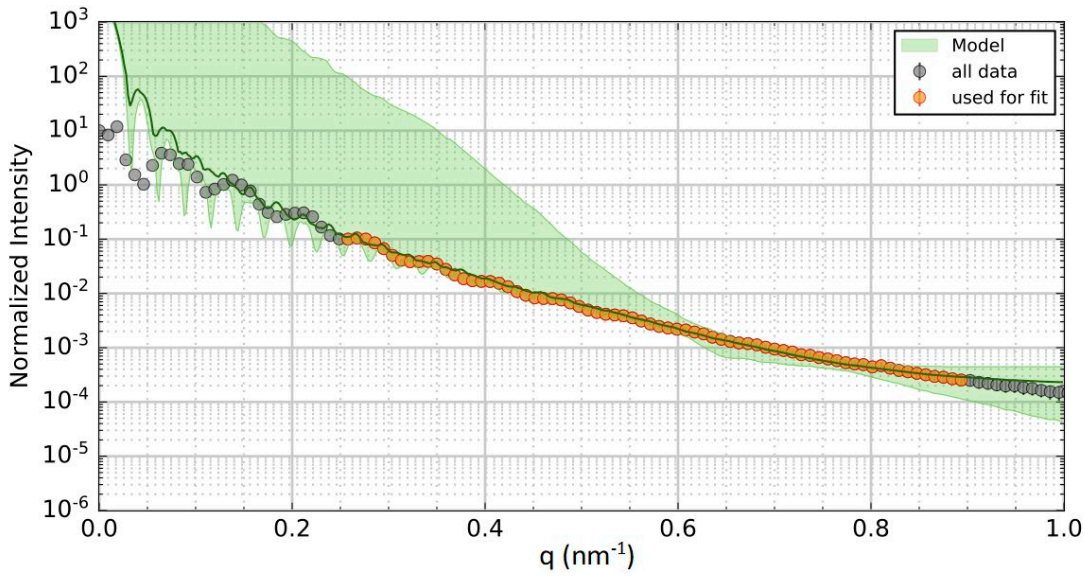

Figure 6.21 Similar to Figure 6.20 expect the range of q is limited to 0.25 and 0.9 nm^{-1}, the uncertainties are relaxed and arbitrary, and the number of fitting parameters is reduced.

Figure 6.21 shows the fit on the range of q between 0.25 nm^{-1} and 0.9 nm^{-1}. The data sued for the fit are shown in orange and the rest are shown in gray for the reference. Neither posteriors nor visual inspection suggest a reasonable fit. This is also evident in the fitting and inability of the retrieval to constrain the values of free parameters. This result may suggest that the uncertainties in the measurement system or heterogeneity of physical parameters are underestimated. However, further investigation is needed to support this claim. Nevertheless, a further immediate step is to narrow the q range even further.

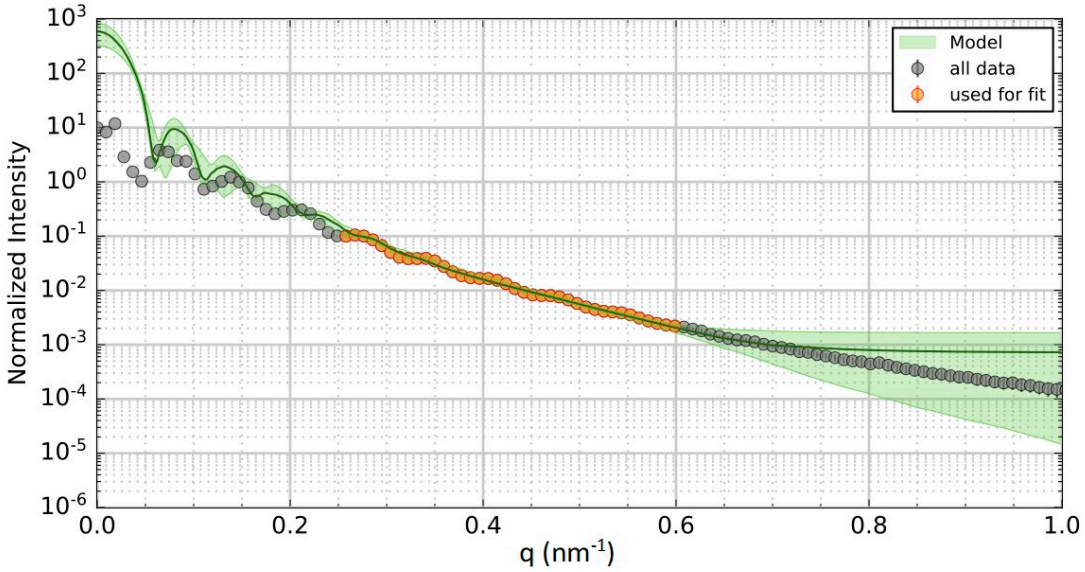

Figure 6.22 Similar to Figure 6.21 expect the range of q is limited to 0.25 and 0.6 nm^{-1}.

Decreasing the q-range to 0.25-0.6 nm^{-1} might help the fitting procedure to emphasize on the form factor pattern and improve the solution for the values of parameters. Figure 6.22 shows the results of such configuration. No improvement is observed in the result. Instead, the fitting algorithm tends to smear the model oscillations in order to force “an averaged” solution, and hence not a reasonable fit.

A compromise, however, might be to limit the q values but move toward smaller *q*s. The amplitude of signals is expected to be larger at smaller *q*s and hence a better fit might be obtained.

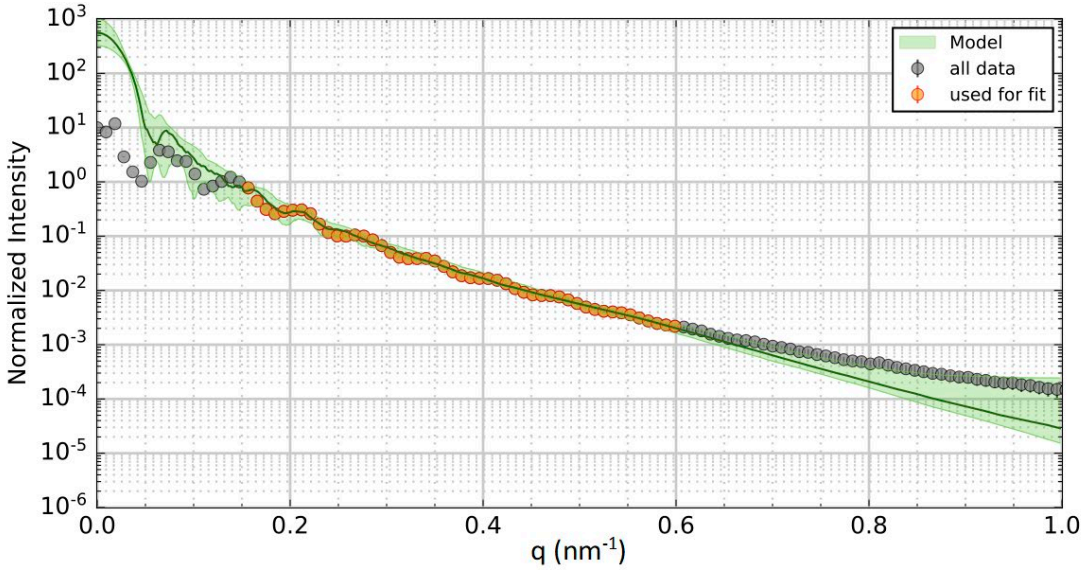

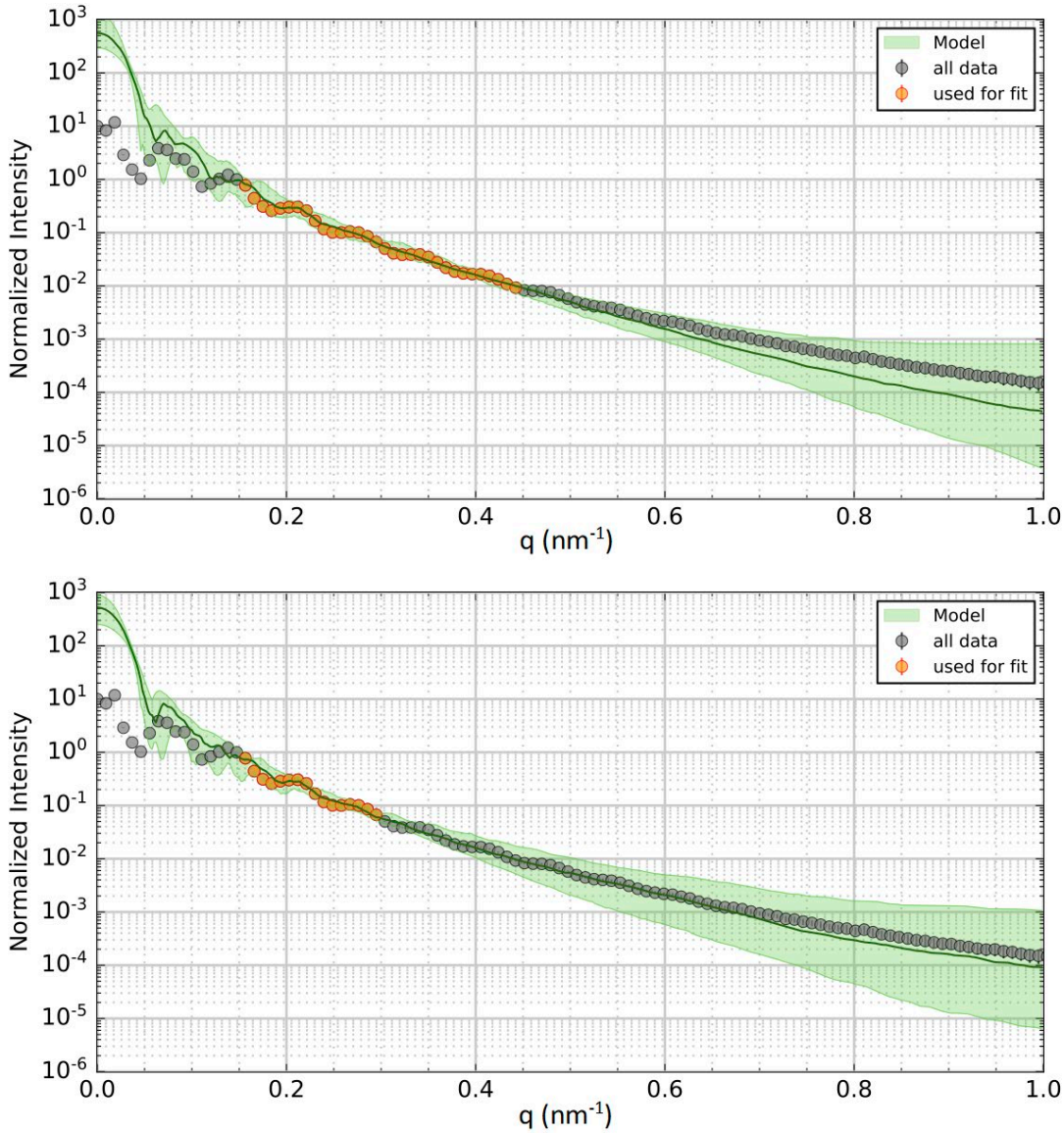

Figure 6.23 Similar to Figure 6.22 expect the range of q is limited to 0.15-0.6 nm^{-1}, 0.15-0.45 nm^{-1} and 0.15-0.30 nm^{-1}.

We examine this by limiting the q-range to 0.15-0.6 nm^{-1}, 0.15-0.45 nm^{-1} and 0.15-0.30 nm^{-1}. However, none applying these limitations do not lead to more physical values of fitted parameters. The results are shown in Figure 6.23.

In another attempt, we change the assumption of the used model in the fitting and consider the form factor as a single cylinder and apply the fitting on q>0.25 nm^{-1}. As shown in figure 6.24 this assumption improves the result. The parameters are physically sensible and in a good agreement with literature. However, given the fact that this fit is systematically underestimating q<0.25 suggests that the model likely to has a missing component. In addition, the microscopic imaging does not support single cylindrical nature of nanopores.

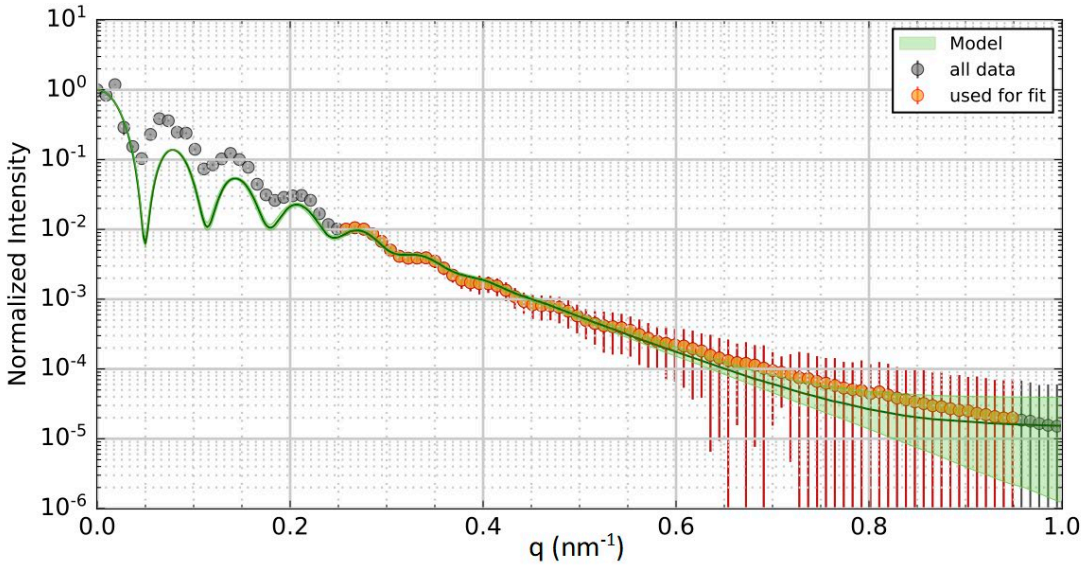

Figure 6.24 Similar to Figure 6.22 expect a single cylindrical form factor is assumed and the range of q is limited to 0.25-0.95 nm^{-1}.

All together, we conclude that the inconsistencies in the retrieved parameters and their expected values might have caused by the data quality and the choice of measured sample. A logical next step is, therefore, stacking several measurements to improve the signal quality.

6.4.2 Fitting to the Median of Samples

Following the conclusion in the previous section, we co-add negative *q*s on positive *q*s and then took the median of the samples of each experiment. We then assigned a relative uncertainty of 20% is assigned to all datapoints.

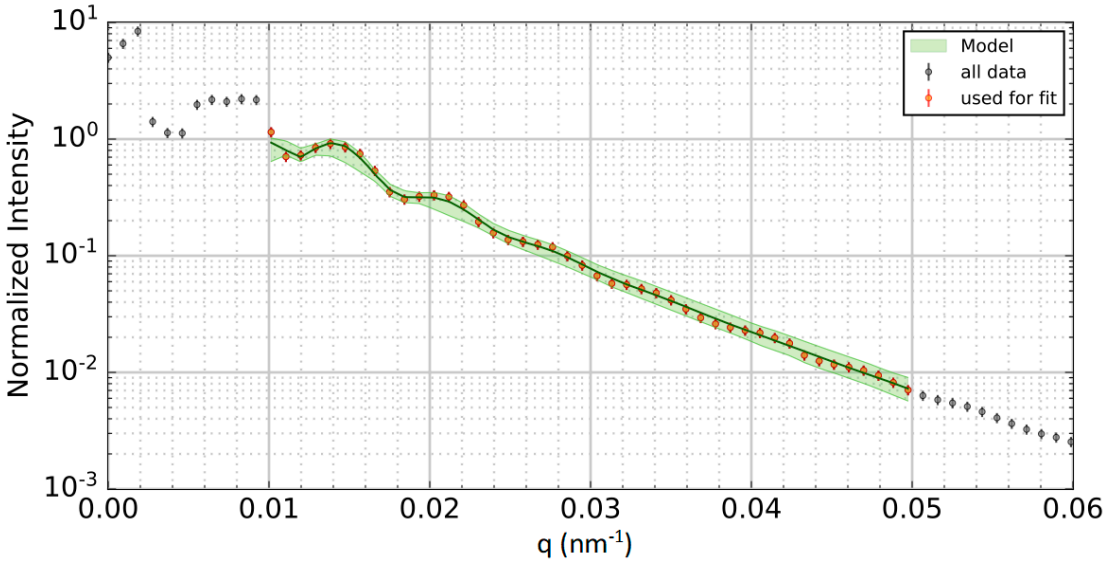

Figure 6.25 Fitting the full model (form factor and structure factor) to the median of seven measurements of a bare sample.

The q<0.1 is ignored to highlight the role of the form factor and the q>0.5 is ignored to prevent the flattened result caused by very high value of σ_r. The structure factor

parameters (κ and R_{hc}) cannot be constrained since we exclude small qs. However, the constrained parameters are summarized in Table-6.1.

Fitting parameters of form factor	
$\langle R_i \rangle$	$47.5^{+4.3}_{-0.9}$
$R_{diff} = \langle R_o \rangle - \langle R_i \rangle$	$8.8^{+10.4}_{-4.7}$
σ_r	$6.6^{+1.0}_{-0.9}$
σ_D	$2.4^{+0.2}_{-0.4}$
ρ_{shell}	819^{+147}_{-92}

Table 6.1 Summary of the constrained parameters of the fit in figure 6.25.

All fitted values are consistent with the expected values and seem to explain a core-shell form factor. The values of inner diameter 47.5 nm and outer diameter 55 nm are in agreement with other studies. The σ_r is relatively higher than what is expected, which flattens the fit results at higher qs faster than the data. The value of the ρ_{shell} seems to be underestimated and cannot be fitted around the expected value of 1025-1075 cm^{-3}. Nevertheless, co-adding the data and taking the median is found to be a reasonable strategy in order to find a reasonable fit to the data.

Although the above result does not contain a complete and accurate characterization of the bare sample, we may consider it as a solution for bare sample and continue with filled samples to see if any discriminative parameter can be found to separate the two types.

According to previous studies [31, 32] scattering by the polymer has a less noticeable contribution in the line profile. This effect can only be detected in data taken at higher resolution of measurement. This is consistent with our experience of fitting the complete model to the data taken from AOO with filled polymers where there was no convergence of the parameters. For this reason, in the second approach the same model (as for the bare samples) is applied to the filled samples. This way we expect to find the electron density difference and/or the values of diameters.

Therefore, we employed the same model fitting procedure on the median of the datasets of three other samples filled with 0.1% of MEM-063, 1% of MEM-063, and 2% of MEM-063 polymer, respectively. We note that in the following models, the structure factor is excluded from our fitting, as it tends to be sensitive to lower qs, which are not included in the analysis. We, therefore, also exclude q values less than 0.1 to highlight the role of the form factor. The result of the fitting to the 0.1% polymer sample is shown in Figure 6.26 and the retrieved values are summarized in Table-6.2.

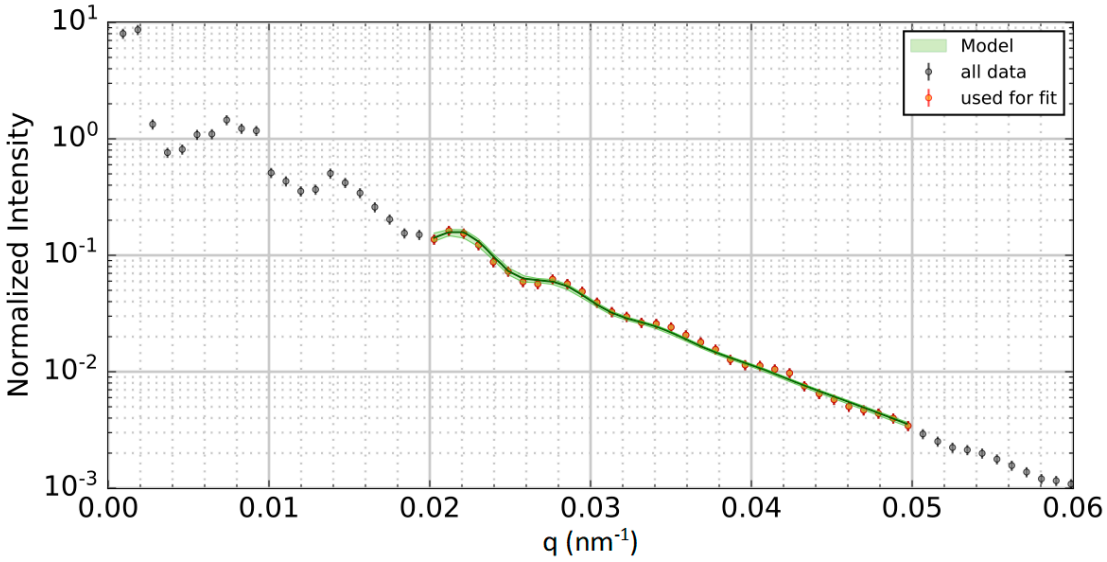

Figure 6.26 Fitting the form factor to the median of seven measurements of a 0.1% polymer sample.

Fitting parameters of form factor	
$\langle R_i \rangle$	$52.4^{+0.6}_{-0.5}$
$R_{diff} = \langle R_o \rangle - \langle R_i \rangle$	--
σ_r	$3.8^{+0.4}_{-0.3}$
σ_D	$2.4^{+0.1}_{-0.1}$
ρ_{shell}	--

Table 6.2 Summary of the parameters of the fit in figure 6.26.

The inner diameter and roughness of the cylinder walls, σ_D, are consistent within one-sigma with our finding on the bare samples. The polydispersity factor, σ_r, found to be smaller than that of the bare samples. Although this might suggest a higher monodispersity in the polymer-filled samples, the ratio of polydispersity factor to the mean inner radius ($\frac{\sigma_r}{\langle R_i \rangle} \sim 0.14$) in our bare sample also suggest a moderately monodispersed sample as well. As shown in the corner plot and summarized in the Table-6.2, the fitting algorithm were unable to constrain the electron density and thickness of the shell.

The result of the fitting to the 1% polymer sample is shown in Figure 6.27 and the retrieved values are summarized in Table-6.3. Similar to the case of 0.1% polymer, the inner diameter and roughness of the cylinder walls, σ_D, are consistent within one-sigma with our finding on the bare samples. However, despite an order of magnitude higher concentration of polymer in the nanopores, the fitting algorithm were unable to constrain the electron density and shell's thickness.

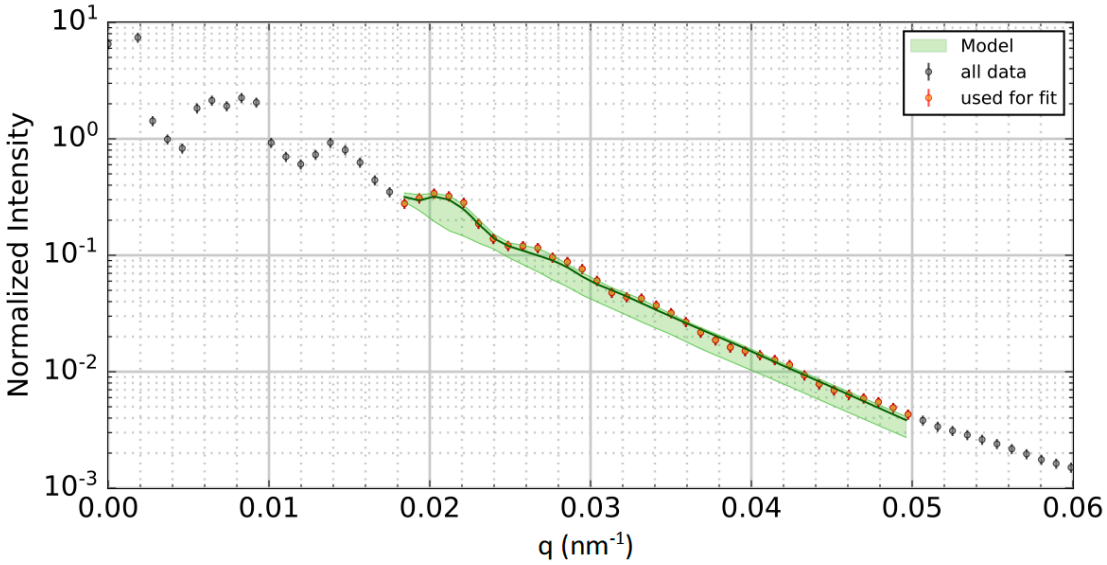

Figure 6.27 Fitting the form factor to the median of seven measurements of a 1% polymer sample.

Fitting parameters of form factor	
$\langle R_i \rangle$	$52.0^{+1.0}_{-1.0}$
$R_{diff} = \langle R_o \rangle - \langle R_i \rangle$	--
σ_r	$4.0^{+0.3}_{-0.2}$
σ_D	$2.8^{+0.1}_{-0.1}$
ρ_{shell}	--

Table 6.3 Summary of the parameters of the fit in figure 6.27.

The result of the fitting to the 2% polymer sample is also shown in Figure 6.28 and the retrieved values are summarized in Table-6.4. Again, the inner diameter and roughness of the cylinder walls, σ_D, are consistent within one-sigma with our finding on the bare samples and the other polymer filled samples. The fitting algorithm were still unable to deduce the electron density and shell thickness, likely due to the data quality and resolution.

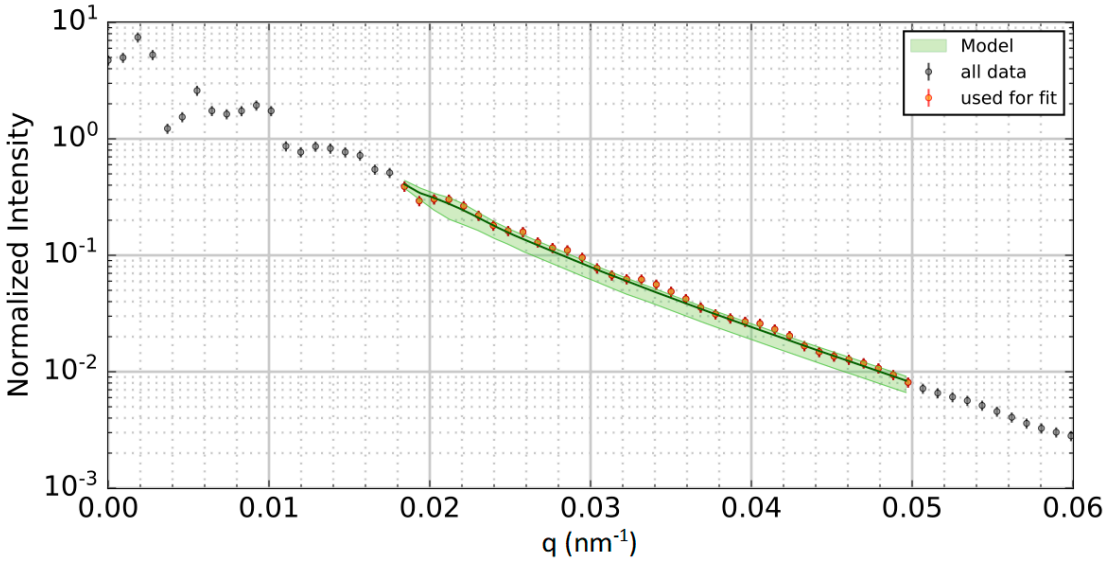

Figure 6.28 Fitting the form factor to the median of seven measurements of a 2% polymer sample.

Fitting parameters of form factor	
$\langle R_i \rangle$	$52.0^{+1.0}_{-1.0}$
$R_{diff} = \langle R_o \rangle - \langle R_i \rangle$	--
σ_r	$5.0^{+1.1}_{-0.5}$
σ_D	$2.1^{+0.1}_{-0.1}$
ρ_{shell}	--

Table 6.4 Summary of the parameters of the fit in figure 6.28.

The low resolution of the taken data causes merging of the adjacent oscillations into one data point and consequently losing informative details of the line profile. This issue is more remarkable at lower q values. In this region the structure factor is dominant. Therefore, the peaks are closer together. They are also rather sharp and narrow peaks. This property makes the merging problem more remarkable. Accordingly finding the right values are even less efficient for the structure factor.

At higher values of q, the form factor plays the main role. The peaks in this region are wider. This leads the fitting approximation to be more consistent. As explained above with the right choice of the q range, the obtained values of the inner radii R_i and σ_D are compatible with the expected values given by other studies [8, 31, 34]. However, the large values of the σ_r obtained by the fitting smear out the oscillations faster than the data. From this point it is inferred that although the fitting procedure might seem to return rigid values with low uncertainties, it ignores the information presented by the data. In most cases, the values of outer radii R_o, the core electron density ρ_{core} and the shell electron density ρ_{shell} are not the convergence results of the fitting. Instead, they are the mean values of wide distributions which obviously are not reliable representatives of the desired values. This effect is apparent in cornel plots.

According to the explained results and given our assessment of the data quality and the fitting algorithm, we conclude that further investigations are needed to proceed with more detail analysis of the data.

7 CONCLUDING REMARKS

In this thesis nanoporous alumina was investigated both for the cases of empty pores and once filled by the thermoresponsive poly(*N*-isopropyl acrylamide) (PNIPAM). The initial intention was to investigate the filling status of the pores by PNIPAM and the thermoresponsive behavior of the PNIPAM in the confinement of the pores. The synthesis of AAO and the trace of effective parameters in the anodization process have been discussed. The initial conditions for the two sizes of AAO sample have been explained. Then the thermoresponsive (PNIPAM and the wetting process of the nanopores filled by the PNIPAM have been described. The XRR experiments have been done on PNIPAM. The polymer was placed on smooth flat silicon substrate. Polymer solutions with three different solution concentrations have been used for the XRR experiment. The critical angle for the silicon was obtained as $\alpha_{cs} = 0.23^{\circ}$ which is in good agreement with literature. This value for the PNIPAM was obtained as $\alpha_{cp} = 0.142^{\circ}$ for all solution concentrations.

The prepared AAO samples were measured, as empty and filled by the polymer by the SAXS experiment which is the tool to study the shape, dimensions, and the electron density of the samples. The experimental setup has been illustrated with the focus on the effect of setup parameters that improve the resolution of the measured data. The measurements were recorded as images by 2D Pilatus detector. The result images have been analyzed carefully to understand the knowledge given by the SAXS experiment.

In the first approach a primary model has been built on the base of mathematical functions of the SAXS intensity given by a grating with shaped holes. The model was developed with the idea of recognition the distinction of scattering pattern measured from the samples with different filling conditions and at different temperatures. For this purpose, a parameter has been appointed which was related to the empty part of the nanopores namely “effective pore diameter”. For samples anodized at 40V and measured at 13 keV of X-ray energy, the corresponding ratio value, $\frac{r_{eff,T}}{d}$ remained unchanged for empty samples and showed a reduction for filled samples at temperatures above LCST. This change can be explained by the swelling of the

polymer. For other cases the differences between the values are in the order of error bars. Therefore, a strong judgment is not possible for the 40V samples at 10 keV and for the 25 keV at 13 and 10 keV energy of the X-ray.

In the second approach an analytical solution has been applied. Mathematical functions of the SAXS intensity through a 2D grating processing cylindrical pores with hexagonal arrangement have been fitted to the data. However, for the real samples there are deviations from the ideal model of regularly arranged circular pores. The sources of the deviations include the disorder in the arrangement of the pores and also the deformation of the surfaces of the pores from the circular shape. The first source has been considered as thermal disorder to a perfect crystal and explained by Debye-Waller factor and the second source has been considered as statistical perturbations to the initial functions. The effect of the roughness of the pores walls and the instrumental effect have been also considered as smearing effects to the functions. The obtained model has been visualized and the effect of parameters have been investigated. This model has been employed to the measured data by fitting process using Monte-Carlo algorithm. At the first attempt the model was not successful to evaluate the parameters.

It was found out that the problem to overcome in the analysis is the insufficient resolution of the measured data which causes merging of the informative data points. This matter is also responsible for the large value of the error bars in the first approach. The resolution parameter, RES, has been introduced to represent the data resolution. The experimental setup has been modified to maximize the RES value by increasing the sample to detector distance up to the point that was limited by the dimensions of the chamber at the beamline. The outcome of the modified setup improved the results of the fitting for some parameters. With this modification, the characteristic parameters of the pores such as pore diameter and wall roughness could be obtained for the empty samples. However, the fitting procedure returned a wider distribution than what the data represents for the pore diameter. The values of the electron densities and the shell diameter did not yet converge in the fitting process. The characteristic parameter of the grating namely the interpore distance could not be obtained by the fitting. Therefore, we conclude that given our experimental setup and data resolution further investigations are needed to proceed with more detail analysis of the data.

Outlook

As explained above, the insufficient data resolution was found to be the main problem of the efficiency in both analysis approaches. It is recommended to work on the relation between RES parameter and efficiency of the fitting approach. It would be worthy to find a lower limit value for the RES parameter which leads to obtain convergence parameters with high accuracies in the fitting procedure. This can be reached by changing the sample to detector distance for constant X-ray energy and same detector. Then the simulations should be applied to data sets with different resolutions. There is a starting point where the simulations can identify the parameters related to the structure factor. At this point the RES parameter can be considered as the lower limit value. Having the lower limit of the RES value, one can confidently design the experimental setup forehand the analysis with low cost and time efficient.

Another suggestion to study on this topic is the method to discriminate and classify the samples based on artificial intelligence and more specifically machine learning algorithms. In the classification algorithms through supervised learning, the discriminating features of the labelled samples are extracted and after pre-processing will be utilized for training the algorithm. The algorithm is basically a classifier which statistically learns from the distribution of training labelled samples. The choice of the classifier is not known in advance while they might be subjected to the feature set. A feedback loop based on the achieved results is necessary. In general, the classifiers based in Bayesian decision rule, Support Vector Machine (SVM), and decision trees could be some well-known candidates. However, if there is some uncertainty about the feature importance and type of the features selected and feature space, the methods based on Deep Learning would be recommended as well wherein the feature engineering task will be elaborated.

BIBLIOGRAPHY

[1] K. Nielsch, J. Choi, K. Schwirn, R. B. Wehrspohn, U. Gösele, "Self-ordering Regimes of Porous Alumina: The 10 Porosity Rule," *Nano Lett.,* vol. 2, no. 7, pp. 677-680, 2002.

[2] M. Moradi, M. Noormohammadi, F. Behzadi, "Three-dimensional structural engineering of nanoporous alumina by controlled sprinkling of an electrolyte on a porous anodic alumina (PAA) template," *J. Phys. D: Appl.Phys,* vol. 44, no. 4, p. 045301, 2011.

[3] M. Noormohammadi, M. Moradi, "Structural engineering of nanoporous alumina by direct cooling the barrier layer during the aluminum hard anodization," *Mater. Chem. Phys.,* vol. 135, no. 2-3, pp. 1089-1095, 2012.

[4] R. Krishnan, C. V. Thompson, "Monodomain High-Aspect-Ratio 2D and 3D Ordered Porous Alumina Structures with Independently Controlled Pore Spacing and Diameter," *Adv. Mater.,* vol. 19, no. 7, pp. 988-992, 2007.

[5] I. V. Roslyakov, E. O. Gordeeva, K. S. Napolskii, "Role of Electrode Reaction Kinetics in Self-Ordering of Porous Anodic Alumina," *Electrochim. Acta,* vol. 241, pp. 362-369, 2017.

[6] D. Losic, M. Lillo, "Porous Alumina with Shaped Pore Geometries and Complex Pore Architectures Fabricated by Cyclic Anodization," *Small,* vol. 5, no. 12, pp. 1392-1397, 2009.

[7] F. Keller, M. S. Hunter, D. L. Robinson, "Structural Features of Oxide Coatings on Aluminum," *J. Electrochem. Soc,* vol. 100, no. 9, pp. 411-419, 1953.

[8] S. Müller, Responsive Nanoporous Anodic Aluminum Oxide/Silicon – Polymer Hybrid Systems for Biological Applications, Siegen: Universität Siegen, 2017.

[9] D. M. Dotzauer, J. Dai, L. Sun, M. L. Bruening, "Catalytic Membranes Prepared Using Layer-by-Layer Adsorption of Polyelectrolyte/Metal Nanoparticle Films in

Porous Supports," *Nano Lett,* vol. 6, no. 10, p. 2268–2272, 2006.

[10] T. Kumeria, A. Santos, D. Losic, "Nanoporous Anodic Alumina Platforms: Engineered Surface Chemistry and Structure for Optical Sensing Applications," *Sensors,* vol. 14, no. 7, pp. 11878-11918, 2014.

[11] F. Casanova, C. E. Chiang, C.-P. Li, I. V. Roshchin, A. M. Ruminski, M. J. Sailor, I. K. Schuller, "Gas adsorption and capillary condensation in nanoporous alumina films," *Nanotechnology,* vol. 19, no. 31, p. 315709, 2008.

[12] T. Kumeria, D. Losic, "Controlling interferometric properties of nanoporous anodic aluminium oxide," *Nanoscale Res. Lett.,* vol. 7, p. 88, 2012.

[13] M. M. Rahman, L. F. Marsal, J. Pallarès, J. Ferré-Borrull, "Tuning the Photonic Stop Bands of Nanoporous Anodic Alumina-Based Distributed Bragg Reflectors by Pore Widening," *ACS Appl. Mater. Interfaces,* vol. 5, no. 24, p. 13375–13381, 2013.

[14] A. R. Walpole, E. P. Briggs, M. Karlsson, E. Pålsgård, P. R. Wilshaw, "Nano-porous Alumina Coatings for Improved Bone Implant Interfaces," *Mat.-wiss. u. Werkstofftech,* vol. 34, no. 12, pp. 1064-1068, 2003.

[15] M. S. Aw, S. Simovic, J. Addai-Mensah, D. Losic, "Polymeric micelles in porous and nanotubular implants as a new system for extended delivery of poorly soluble drugs," *J. Mater. Chem.,* vol. 21, no. 20, pp. 7082-7089, 2011.

[16] B. Malfait, A. Jani, J. B. Mietner, R. Lefort, P. Huber, M. Fröba, D. Morineau, "Influence of Pore Surface Chemistry on the Rotational Dynamics of Nanoconfined Water," *J. Phys. Chem. C,* vol. 125, no. 30, p. 16864–16874, 2021.

[17] D.-K. Kim, K. Kerman, M. Saito, R. R. Sathuluri, T. Endo, S. Yamamura, Y.-S. Kwon, E. Tamiya, "Label-Free DNA Biosensor Based on Localized Surface Plasmon Resonance Coupled with Interferometry," *Anal. Chem.,* vol. 79, no. 5, pp. 1855-1864, 2007.

[18] T. Kumeria, L. Parkinson, D. Losic, "A nanoporous interferometric micro-sensor for biomedical detection of volatile sulphur compoundscite," *Nanoscale Res. Lett.,* vol. 6, p. 634, 2011.

[19] S.-J. Li, N. Xia, B.-Q. Yuan, W.-M. Du, Z.-F. Sun, B.-B. Zhou, "A novel DNA sensor using a sandwich format by electrochemical measurement of marker ion fluxes across nanoporous alumina membrane," *Electrochim. Acta,* vol. 159, pp. 234-241, 2015.

[20] N. Haberkorn, J. S. Gutmann, P. Theato, "Template-Assisted Fabrication of Free-Standing Nanorod Arrays of a Hole-Conducting Cross-Linked Triphenylamine Derivative: Toward Ordered Bulk-Heterojunction Solar Cells," *ACS Nano,* vol. 3, no. 6, pp. 1415-1422, 2009.

[21] A. GUINIER, X-ray difraction in crystals, imperfect crystals, and amorphous bodies, New York: Dover Publications, INC., 1994.

[22] R.-J. Roe, Methods of X-ray and neutron scattering in polymer science, Oxford University Press on Demand, 2000.

[23] D. Sivia, Elemental Scatteing Theory for X-ray and Neutron Users, Oxford: Oxford university press, 2011.

[24] Als-Nielsen, J., McMorrow, D., Elements of Modern X-ray Physics, London: Wiley & Sons, 2011.

[25] K. Eidmann, M. Kühne, P. Müller, G.D. Tsakiris,, "Characterization of Pinhole Transmission Gratings," *J. X-Ray Sci. and Tech.,* vol. 2, no. 4, pp. 259-273, 1990.

[26] L. E. Ruggles, M. E. Cuneo, J. L. Porter, D. F. Wenger, and W. W. Simpson, "Measurement of the efficiency of gold transmission gratings in the 100 to 5000 eV photon energy range," *Rev. Sci. Ins.,* vol. 72, no. 1, pp. 1218-1222, 2001.

[27] W. Ruland, B. Smarsly, "X-ray scattering of non-graphitic carbon: an improved method of evaluation," *J. Appl. Cryst.,* vol. 35, no. 5, pp. 624-633, 2002.

[28] W. Ruland and B. Smarsly, "SAXS of self-assembled nanocomposite films with oriented two-dimensional cylinder arrays: an advanced method of evaluation," *J. Appl. Cryst.,* vol. 38, no. 1, pp. 78-86, 2005.

[29] B. Smarsly, H. Kaper, W. Ruland, "On the analysis of SAXS data from oriented 2D cylindrical mesostructures measured in symmetric reflection," *Nuclear Inst. and Meth. Phys. Res. Sect. B,* vol. 246, no. 1, pp. 249-253, 2006.

[30] M. Engel, B. Stühn,J. J. Schneider, T. Cornelius, M. Naumann, "Small-angle X-ray scattering (SAXS) off parallel, cylindrical, well-defined nanopores: from random pore distribution to highly ordered samples," *Appl. Phys. A.,* vol. 97, no. 1, pp. 99-108, 2009.

[31] M. Engel, Untersuchung von Füllprozessen und Strukturen von Polymeren in zylindrischen Nanoporen, Darmstadt: Technische Universität Darmstadt, 2009.

[32] M. Khaneft, Polymers in aligned carbon nanotube arrays, Darmstadt: Technische Universität Darmstadt, 2013.

[33] A. Hadley, C. Notthoff, P. Mota-Santiago, S. Dutt, S. Mudie, M. A. Carrillo-Solano, M. E. Toimil-Molares, C. Trautmann, and P. Kluth, "Analysis of nanometer-sized aligned conical pores using small-angle x-ray scattering," *Phys. Rev. Materials,* vol. 4, no. 5, p. 056003, 2020.

[34] M. Raoufi, Modification and Functionalization of Porous Alumina Templates with Polymers, Siegen: Universität Siegen, 2013.

[35] X. Wang, Y. Li, M. Zhou, J. Duan, H. Luo, L. Ye, X. Liu, X. Lin, "Theoretical Simulation of X-Ray Transmission Through a Polycapillary X-Ray Lens With a Variable Capillary Radius," *IEEE Transactions on Nuclear Science,* vol. 67, no. 5, pp. 791-796, 2020.

[36] I.V. Roslyakov, D.S. Koshkodaev, A.A. Eliseev, D. Hermida-Merino, A.V.

Petukhov, K.S. Napolskii, "Crystallography-Induced Correlations in Pore Ordering of Anodic Alumina Films," *J. Phys. Chem. C,* vol. 120, no. 35, p. 19698–19704, 2016.

[37] W. Lee, J.-Ch. Kim, "Highly ordered porous alumina with tailor-made pore structures fabricated by pulse anodization," *Nanotechnology,* vol. 21, no. 48, p. 485304, 2010 .

[38] J. P. O'Sullivan, G. C. Wood, "The morphology and mechanism of formation of porous anodic films on aluminium," *Proc. R. Soc. Lond. A,* vol. 317, no. 1531, pp. 511-543, 1970.

[39] W. Lee, R. Ji, U. Gösele, K. Nielsch , "Fast fabrication of long-range ordered porous alumina membranes by hard anodization," *Nature Matr.,* vol. 5, pp. 741-747, 2006.

[40] H. Masuda, K. Fukuda, "Ordered Metal Nanohole Arrays Made by a Two-Step Replication of Honeycomb Structures of Anodic Alumina," *Science,* vol. 268, no. 5216, pp. 1466-1468, 1995.

[41] H. Masuda, H. Yamada, M. Satoh, H. Asoh, , M. Nakao , T. Tamamura, "Highly ordered nanochannel-array architecture in anodic alumina," *Appl. Phys. Lett.,* vol. 71, no. 19, pp. 2770-2772, 1997.

[42] O. Jessensky, F. Müller, U. Gösele, "Self-organized formation of hexagonal pore arrays in anodic alumina," *Appl. Phys. Lett.,* vol. 72, no. 10, pp. 1173-1175, 1998.

[43] H. Masuda, F. Hasegawa, S. Ono, "Self-Ordering of Cell Arrangement of Anodic Porous Alumina Formed in Sulfuric Acid Solution," *J. Electrochem. Soc,* vol. 144, no. 5, p. L127–L130, 1997.

[44] A. P. Li, F. Müller, A. Birner, K. Nielsch, and U. Gösele, "Hexagonal pore arrays with a 50–420 nm interpore distance formed by self-organization in anodic alumina," *J. Appl. Phys.,* vol. 84, no. 11, pp. 6023-6026, 1998.

[45] H. Asoh, K. Nishio, M. Nakao, A. Yokoo, T. Tamamura, H. Masuda, "Fabrication of ideally ordered anodic porous alumina with 63 nm hole periodicity using sulfuric acid," *J. Vac. Sci. Technol. B,* vol. 19, no. 2, pp. 569-572, 2001.

[46] K. R. Hebert, S. P. Albu, I. Paramasivam, P. Schmuki, "Morphological instability leading to formation of porous anodic oxide films," *Nat. Mater.,* vol. 11, no. 2, pp. 162-166, 2011.

[47] H. Masuda, K. Yada, A. Osaka, "Self-Ordering of Cell Configuration of Anodic Porous Alumina with Large-Size Pores in Phosphoric Acid Solution," *Jpn. J. Appl. Phys.,* vol. 37, no. 11A, p. L1340–L1342, 1998.

[48] M. T. Wu, I. C. Leu, M. H. Hon, "Effect of polishing pretreatment on the fabrication of ordered nanopore arrays on aluminum foils by anodization," *J. Vac. Sci. Technol. B.,* vol. 20, no. 3, pp. 776-782, 2002.

[49] S. Shingubara, K. Morimoto, H. Sakaue, T. Takahagi, "Self-Organization of a Porous Alumina Nanohole Array Using a Sulfuric/Oxalic Acid Mixture as Electrolyte," *Elec. Solid-State Lett.,* vol. 7, no. 3, pp. E15-E17, 2004.

[50] P. C. Painter, M. M. Coleman, Fundamentals of Polymer Science, CRC Press, 1997.

[51] J. M. G. Cowie, V. Arrighi, Polymers: Chemistry and physics of modern materials, Boca Raton: CRC Press, 2007.

[52] A. D. Jenkins, P. Kratochvil, R. F. T. Stepto, U. W. Suter, "Glossary of basic terms in polymer science," *Pure and Appl. Chem.,* vol. 68, no. 12, pp. 2287-2311, 1996.

[53] J. R. Wünsch, Polystyrene: Synthesis, production and applications, shropshire: iSmithers Rapra Press, 2000.

[54] M. Heskins, J. E. Guillet, "Solution Properties of Poly(N-isopropylacrylamide)," *J. Mac.molecular Scie.: Part A - Chem.,* vol. 2, no. 8, pp. 1441-1455, 1968.

[55] Y. Akiyama, T. Okano, 9 - Temperature-responsive polymers for cell culture and tissue engineering applications, Z. Zhang, Ed., Woodhead Publishing, 2015, pp. 203-233.

[56] J. Niskanen, H. Tenhu, "How to manipulate the upper critical solution temperature (UCST)?," *Polym. Chem.,* vol. 8, no. 1, pp. 220-232, 2017.

[57] M. Toma, U. Jonas, A. Mateescu, W. Knoll, J. Dostalek, "Active Control of SPR by Thermoresponsive Hydrogels for Biosensor Applications," *J. Phys. Chem. C,* vol. 117, no. 22, p. 11705–11712, 2013.

[58] E. M. Ahmed, "Hydrogel: Preparation, characterization, and applications: A review," *J. Adv. Research,* vol. 6, no. 2, pp. 105-121, 2015.

[59] S. Lee, B. Lee, J. Choi, C.-S. Chi, "Effects of Various Solution Wetting Conditions on the Morphology and the Crystallization of Poly (Vinylidene Fluoride) Nanotubes," *J. Korean Phys. Soc.,* vol. 54, no. 3, pp. 1198-1202, 2009.

[60] H.-W. Shin, E.-J. Shin, S.Y. Cho, S.-L. Oh, Y.-R. Kim, "Enhanced Energy Transfer within PVK/Alq3 Polymer Nanowires Induced by the Interface Effect of Nanochannels in Porous Alumina Membrane," *J. Phys. Chem. C,* vol. 111, no. 42, p. 15391–15396, 2007,.

[61] H. W. Fox, E. F. Hare, W. A. Zisman, "Wetting properties of organic liquids on high-energy surfaces," *J. Phys. Chem.,* vol. 59, pp. 1097-1106, 1955.

[62] P. G. de Gennes, "Wetting: statics and dynamics," *Rev. Mod. Phys,* vol. 57, no. 3, pp. 827-863, 1985.

[63] S. Wu, Polymer Interface and Adhesion, New York: Dekker, 1982.

[64] M. Steinhart, J. H. Wendorff, R. B. Wehrspohn,, "Nanotubes a la Carte: Wetting of Porous," *ChemPhysChem,* vol. 4, pp. 1171-1176, 2003.

[65] S. Jin, Y. Lee, S.-M. Jeon, B.-H. Sohn, W.-S. Chae, J.-K. Lee, "Simple fabrication of single- and multi-layer polymer nanotubes by spin-casting method within anodized aluminum oxide (AAO) templates," *J. Mater. Chem.,* vol. 22, pp. 23368-23373, 2012.

[66] J. Martín, C. Mijangos, "Tailored Polymer-Based Nanofibers and Nanotubes by Means of Different Infiltration Methods into Alumina Nanopores," *Langmuir,* vol. 25, no. 2, pp. 1181-1187, 2009.

[67] J. Byun, N.-H. Kim, D. H. Lee, K.-H. Lee, J. K. Kim, "Core-shell polymeric nanorods prepared from reactive polymer bilayer via sequential complete wetting," *Soft Matter,* vol. 5, pp. 3835-3838, 2009.

[68] J.-T. Chen, C.-W. Lee, M.-H. Chi, I.-C. Yao, "Solvent-Annealing-Induced Nanowetting in Templates: Towards Tailored Polymer Nanostructures," *Macromol. Rapid Commun.,* vol. 34, no. 4, pp. 348-354, 2013.

[69] M. Zhang, P. Dobriyal, J.-T. Chen, T. P. Russell, J. Olmo, A. Merry, "Wetting Transition in Cylindrical Alumina Nanopores with Polymer Melts," *Nano Lett.,* vol. 6, no. 5, pp. 1075-1079, 2006.

[70] J. Martín, A. Nogales, M. Martín-González, "The Smectic–Isotropic Transition of P3HT Determines the Formation of Nanowires or Nanotubes into Porous Templates," *Macromolecules,* vol. 46, no. 4, pp. 1477-1483, 2013.

[71] M. Heskins, J. E. Guillet, "Solution Properties of Poly(N-isopropylacrylamide)," *J. Macromol Sci. A Chem.,* vol. 2, no. 8, pp. 1441-1455, 1968.

[72] S. Furyk, Y. Zhang, D. Ortiz-Acosta, P. S. Cremer, D. E. Bergbreiter, "Effects of end group polarity and molecular weight on the lower critical solution temperature of poly(N-isopropylacrylamide)," *J. Polym. Sci. A Polym. Chem.,* vol. 44, no. 4, pp. 1492-1501, 2006.

[73] F. Afroze, E. Nies, H. Berghmans, "Phase transitions in the system poly(N-isopropylacrylamide)/water and swelling behaviour of the corresponding networks," *J. Mol. Struct.,* vol. 544, no. 1, pp. 55-68, 2000.

[74] M. A. Cooperstein, B. M. Bluestein, H. E. Canavan, "Synthesis and optimization of fluorescent poly(N-isopropyl acrylamide)-coated surfaces by atom transfer radical polymerization for cell culture and detachment," *Biointerphases,* vol. 10, no. 1, p. 019001 , 2015.

[75] M. Tolan, T. Weis, C. Westphal, K. Wille, "DELTA: Synchrotron light in nordrhein-westfalen," *Synchrotron Radiation News,* vol. 16, no. 2, pp. 9-11, 2003.

[76] D. Lützenkirchen-Hecht, R. Wagner, S. Szillat, A. K. Hüsecken, K. Istomin, U. Pietsch, Ronald Frahm, "The multi-purpose hard X-ray beamline BL10 at the DELTA," *J. Synchrotron Rad.,* vol. 21, p. 819–826, 2014.

[77] U. Berges, C. Sternemann, M. Tolan, C. Westphal, T. Weis, and K. Wille, "Status of the synchrotron light source DELTA," *AIP Conf. Proc.,* vol. 879, no. 1, pp. 30-

33, 2007.

[78] M. Paulus, D. Lietz, C. Sternemann, K. Shokuie, F. Evers, M. Tolan, C. Czeslik, R. Winter, "An access to buried interfaces: the X-ray reflectivity set-up of BL9 at DELTA," *J. Synchrotron Rad.,* vol. 15, no. 6, pp. 600-606, 2008.

[79] C. Krywka, C. Sternemann, M. Paulus, N. Javid, R. Winter, A. Al-Sawalmih, S. Yi, D. Raabe, M. Tolan, "The small-angle and wide-angle X-ray scattering set-up at beamline BL9 of DELTA," *J. Synchrotron Rad.,* vol. 14, pp. 244-251, 2007.

[80] C. Krywka, M. Paulus, C. Sternemann, M. Volmer, A. Remhof, G. Nowak, A. Nefedov, B. Pöter, M. Spiegel, M. Tolan, "The new diffractometer for surface X-ray diffraction at beamline BL9 of DELTA," *J. Synchrotron Rad.,* vol. 13, pp. 8-13, 2006.

[81] D. Lützenkirchen-Hecht, R. Wagner, U. Haake, A. Watenphul, R. Frahm, "The materials science X-ray beamline BL8 at the DELTA storage ring," *J. Synchrotron Rad.,* vol. 16, pp. 264-272, 2009.

[82] C. Krywka, C. Sternemann, M. Paulus, M. Volmer, U. Berges, M. Tolan, "Experimental Endstation of Beamline BL9 at DELTA," *AIP Conf. Proc.,* vol. 879, p. 875878, 2007.

[83] Inductiveload, "File:EM Spectrum Properties reflected.svg," Creative Commons Attribution, 14 2 2013. [Online]. Available: https://commons.wikimedia.org/wiki/File:EM_Spectrum_Properties_reflected.svg. [Accessed 26 9 2021].

[84] "File:Roentgen2.jpg," LIFE Photo Archive, 20 6 2012. [Online]. Available: https://commons.wikimedia.org/ wiki/File:Roentgen2.jpg. [Accessed 26 9 2021].

[85] W. Röntgen, "File:First medical X-ray by Wilhelm Röntgen of his wife Anna Bertha Ludwig's hand - 18951222.gif," {{PD-US-no notice}},, 24 10 2008. [Online]. Available: https://commons.wikimedia.org/wiki/File:First_medical_X-ray_by_Wilhelm_R%C3%B6ntgen_of_his_wife_Anna_Bertha_Ludwig%27s_hand_-_18951222.gif. [Accessed 26 9 2021].

[86] N. foundation, "File:Max von Laue sign.jpg," Les Prix Nobel 1914 p. 99, 15 6 2014. [Online]. Available: https://commons.wikimedia.org/wiki/File:Max_von_Laue_sign.jpg. [Accessed 26 9 2021].

[87] [Online]. Available: http://macxray.chem.upenn.edu/course/intro1.html.

[88] P. P. Ewald, Dispersion und Doppelbrechung von Elektronengittern, München: Ludwigs-Maximilians-Universität zu München, 1912.

[89] P. P. Ewald, "Contributions to the theory of the interferences of X-rays in crystals," *Phys. Z,* vol. 14, pp. 465-472, 1913.

[90] D.W.J. Cruickshank H.J.Juretschke, N.Kato, "P.P.Ewald and his dynamical theory of x-ray diffraction," *J-Stage,* vol. 20, p. 52, 1993.

[91] A. Authier, "Optical properties of X-rays - dynamical diffraction," *Acta Cryst. ,*

vol. A68, pp. 40-56, 2012.

[92] H. P. Myers, Introductory solid state physics, CRC press, 1997.

[93] Z. Molla, Structure analysis of organic molecule XNRD22L01 thin films, Siegen: Universit□at Siegen, 2018.

[94] Y. Waseda, E. Matsubara, K. Shinoda, "Reciprocal Lattice and Integrated Intensities of Crystals," in *X-Ray Diffraction Crystallography*, Heidelberg, Springer, Berlin, 2011, pp. 169-218.

[95] Y. Gu, X-ray investigation of organic molecule pdi8-cn2, Siegen: Universität Siegen, 2010.

[96] F. R. Elder, A. M. Gurewitsch, R. V. Langmuir, H. C. Pollock, "Radiation from Electrons in a Synchrotron," *Phys. Rev.,* vol. 71, no. 11, pp. 829-830, 1947.

[97] L. Grodd, Current induced structural changes in ofet devices, Siegen: Universität Siegen, 2011.

[98] P. Willmott., An introduction to synchrotron radiation: techniques and, John Wiley and Sons Press, 2011.

[99] R. S. Khandpur, Handbook of analytical instruments, McGraw-Hill Education, 1989.

[100] F. B. C. M. S. Mobilio, Synchrotron radiation: Basics, methods and applications, Springer Press, 2015.

[101] "SYNCHROTRON RADIATION," AARHUS University, 13 6 2009. [Online]. Available: https://www.isa.au.dk/facilities/astrid/ electrons/sr.asp. [Accessed 26 9 2021].

[102] A. Madsen, H. Sinn, "Europe enters the extreme X-ray era," CERNCOURIER, 10 7 2017. [Online]. Available: https://cerncourier.com/a/europe-enters-the-extreme-x-ray-era/. [Accessed 26 9 2021].

[103] W. D. Kimura, "What are electromagnetic waves?," in *Electromagnetic Waves and Lasers*, Morgan & Claypool Publishers, 2017, pp. 1-1 to 1-33.

[104] L. Barré, "Contribution of Small-Angle X-Ray and Neutron Scattering (SAXS and SANS) to the Characterization of Natural Nanomaterials," in *X-ray and Neutron Techniques for Nanomaterials Characterization*, Springer, Berlin, Heidelberg, 2016, pp. 665-716.

[105] A. Angelova, V. M. Garamus, B. Angelov, Z. Tian, Y. Li, A. Zou, "Advances in structural design of lipid-based nanoparticle carriers for delivery of macromolecular drugs, phytochemicals and anti-tumor agents," *Adv. Colloid and Interface Science,* vol. 249, pp. 331-345, 2017.

[106] "Interference and Diffraction," MIT, [Online]. Available: https://web.mit.edu/8.02t/www/802TEAL3D/visualizations/ coursenotes/modules/guide14.pdf. [Accessed 26 9 2021].

[107] E. Hecht, "Diffraction," in *Optics*, Eugene Hecht Reading, MA: Addison-Wesley Publishing Company, 1987, pp. 392-435.

[108] [Online]. Available: http://hyperphysics.phy-astr.gsu.edu/hbase/phyopt/slits.html#c1. [Accessed 26 9 2021].

[109] P. Mittelbach, G. Porod, "Zur Röntgenkleinwinkelstreuung verdünnter kolloider Systeme - Die Berechnung der Streukurven von Parallelepipeden," *Acta Physica Austriaca,* vol. 15, pp. 122-147, 1962..

[110] G. Pépy, P. Boesecke, A. Kuklin, E. Manceau, B .Schiedt, Z. Siwy, M. Toulemondeg, C. Trautmanne, "Cylindrical nanochannels in ion-track polycarbonate membranes studied by small-angle X-ray scattering," *Journal of Applied Crystallography,* vol. 40, no. 1, pp. s388-s392, 2007.

[111] H. Masuda, H. Asoh, M. Watanabe, K. Nishio, M. Nakao, T. Tamamura, "Square and Triangular Nanohole Array Architectures in Anodic Alumina," *Advanced Materials,* vol. 13, no. 3, pp. 189-192, 2001.

[112] Y. Rosenfeld, "Free-energy model for the inhomogeneous hard-sphere fluid in D dimensions: Structure factors for the hard-disk (D=2) mixtures in simple explicit form," *Phys. Rev. A,* vol. 42, no. 10, pp. 5978-5989, 1990.

[113] J. K. Percus, G. J. Yevick, "Analysis of Classical Statistical Mechanics by Means of Collective Coordinates," *Phys. Rev. ,* vol. 110, no. 1, pp. 1-13, 1958.

[114] P. Zaumseil, "X-ray Reflectivity Characterisation of Thin-Film and Multilayer Structures," in *Materials for Information Technology. Engineering Materials and Processes*, Springer, London, 2005, pp. 497-505.

[115] D. Attwood, Soft x-rays and extreme ultraviolet radiation: principles and applications, Cambridge university press, 2000.

[116] "X-ray reflectivity," [Online]. Available: https://people.eecs.berkeley.edu/ ~attwood/sxr2009/ lecnotes/ 04_Reflection_And_Refraction_2009.pdf. [Accessed 26 9 2021].

[117] J. A. Cronin, D. F. Greenberg, V. L. Telegdi, V. Telegdi, University of Chicago graduate problems in physics with solutions, University of Chicago Press, 1979.

[118] A. Biermanns, Manual for the experiment, X-Ray-Reflectometry, Siegen: Universität Siegen, 2007.

[119] U. Pietsch, V. Holy, T. Baumbach, High-resolution X-ray scattering: from thin films to lateral nanostructures, Springer Science & Business Media, 2004.

[120] T. C. Huang, R. Gilles, G. Will, "Thin-film thickness and density determination from x-ray reflectivity data using a conventional power diffractometer," *Thin Solid Films,* vol. 230, no. 2, pp. 99-101, 1993.

[121] J. Daillant, A. Gibaud, X-ray and neutron reflectivity: principles and applications, Vol. 770. Springer, 2008.

[122] A. I. Lvovsky, "Fresnel equations," *Encyclopedia of Optical Engineering,* vol. 27,

pp. 1-6, 2013.

[123] "Small Angle X-Ray Scattering and Diffraction," Safinya Group Research, [Online]. Available: http://www.mrl.ucsb.edu/ ~safinyaweb/ XRD.htm. [Accessed 26 9 2021].

[124] J. Goodman, J. Weare, "Ensemble samplers with affine invariance," *Commun. Appl. Math. Comput. Sci,* vol. 5, no. 1, pp. 65-80, 2010.

[125] D. Foreman-Mackey, D. W. Hogg, D. Lang, J. Goodman, "emcee: the MCMC hammer," *Publications of the Astronomical Society of the Pacific,* vol. 125, no. 925, pp. 306-312, 2013.

[126] K. Molaverdikhani, Characterization of Planetary Atmospheres, Heidelberg: PhD diss, Heidelberg University, 2020.

ACKNOWLEDGMENT

I would like to give my thanks to all of those people who helped me during my Ph.D. study and at this stage. First and foremost, I would like to express my sincere gratitude to my Ph.D. supervisor Prof. Dr. Ullrich Pietsch who gave me the opportunity to work and study at the Chair of Solid State Physics at University of Siegen. During the past five years, I have been given his intelligence supervisory, kind support and invaluable experience academically and socially.

I would like to give my sincere appreciation to the esteemed Ph.D. committee member and my second referee Prof. Dr. Patrick Huber for his valuable comments and feedback on this dissertation since past years.

I would like to express my gratitude to esteemed members of Ph.D. examination committee Prof. Dr. Holger Schönherr and Prof. Dr. Otfried Gühne due to their constructive and helpful feedback and comments.

I would like to thank all of my colleagues and friends with whom I had very nice experience and enjoyable time during the work. I had wonderful time through regular meetings, face-2-face seminars, social events and discussions. Lack of such an environment has been extremely highlighted during the pandemic situation since 2020.

I would like to thank Dr. Hyeokmin Choe for the nice scientific discussion.

I would like to appreciate Dr. Karan Moolaverdikhani from Max Planck Institute in Heidelberg due to his valuable support and comments where the scientific computations have been taking place.

I would like to thank the beamline scientists at DELTA Dr. Christian Sternemann, Dr. Michael Paulus, Dr. Ralph Wagner, and Dr. Özgül Öztürk for their scientific and technical help.

I would like to thank Deutsche Forschungsgemeinschaft (DFG) for the financial support.

I would like to thank House of Young Talents (HYT) office at University of Siegen who supported me by granting the scholarship to accomplish the final stage of my Ph.D. dissertation.

Finally, I would like to extend my appreciation to my beloved family. I am grateful of both my parents and parents-in-law due to their endless support and kind words during the Ph.D. study. With no doubt reaching to this stage without their heartfelt and inspiring encouragement was not possible. At last but not the least, I would like to thank my husband my son and my little daughter for their patience, trust and great support.